Toward optically defined mechanical geometry

Abeer Z. Barasheed

Department of Physics

McGill University, Canada

Supervisor: Jack C. Sankey

November, 2017

Thesis submitted to McGill University in partial fulllment of the requirements of the degree of Doctor of Philosophy

Abstract

In the field of optomechanics, radiation forces have provided a particularly high level of control over the frequency and dissipation of mechanical elements. In this dissertation, we first propose a class of optomechanical systems in which light exerts a similarly profound influence over two other fundamental parameters: geometry and mass. By applying an optical trap to one lattice site of an extended phononic crystal, we show it should be possible to create a tunable, localized mechanical mode. Owing to light's simultaneous and constructive coupling with the structure's continuum of modes, we estimate that a trap power at the level of a single intracavity photon should be capable of producing a significant effect within a realistic, chip-scale device. In the second half of the dissertation, we discuss progress toward realizing the requisite two-dimensional phononic crystal membranes for such experiments. We report the results of several fabrication techniques (each with their own drawbacks), finding it is possible to consistently produce 100 nm to 300 nm thick stoichiometric Si_3N_4 freestanding crystals with an area as large as 20 mm^2, up to 2750 crystal unit cells, and tethers as narrow as $\sim$ 1.5 μm, using wafer-scale photolithography. Preliminary mechanical characterization verifies that these devices indeed exhibit the phononic bandgap required for laser-induced localization experiments (with a ratio of gap width to band edge frequency as high as 80%).

Résumé

Dans le domaine de l'optomécanique, les forces de radiation ont permis un particulièrement grand degré de contrôle sur la fréquence et la dissipation d'éléments mécaniques. Dans le cadre de cette dissertation, nous proposons d'abord une catégorie de systèmes optomécaniques où la lumière exerce une forte influence similaire sur deux autres paramètres fondamentaux : la géométrie et la masse. En appliquant un piège optique au site réticulaire d'un cristal phononique élargi, nous démontrons qu'il devrait être possible de créer un mode mécanique localisé accordable. En raison des couplages simultanés et constructifs de la lumière avec le continuum de modes de la structure, nous estimons qu'un pouvoir de trappe au niveau de la cavité unique d'un photon devrait pouvoir produire un effet significatif à l'intérieur d'un appareil à puce. Dans la deuxième moitié de la dissertation, nous discutons du progrès accompli en vue de produire les membranes de cristal phononique à deux dimensions nécessaire à de telles expériences. Nous présentons les résultats de plusieurs techniques de fabrication (chacune avec ses lacunes particulières) et attestons qu'il est possible de produire constamment 100 nm à 300 nm de cristaux Si_3N_4 stoechiométriques indépendants épais avec une superficie pouvant aller jusqu'à 20 mm^2, jusqu'à 2750 de cristal avec des mailles et des ancrages aussi minces que $\sim$ 1.5 μm, en utilisant la photolithographie à l'échelle d'une plaquette. La caractérisation mécanique préliminaire indique que ces appareils exhibent le bord de bande phononique requis pour des expériences de localisation au laser (avec un ratio de fréquence aussi élevé que 80 % entre la largeur de bande et le bord de la bande).

Dedicated to...

My mother

The soul of my father

My husband

My kids

My brother and my sisters

May Allah bless them all.

Acknowledgment

All praises are due to Allah for giving me the health, courage and patience to complete this milestone of my life.

Most of all, I would like to express my deep and endless gratitude to my advisor Jack who has smartly, wisely and insightfully guided the overall evolution of my dissertation work. During my PhD thrilling journey, Jack has been always a rich source of knowledge and creative inputs with a great sense of intuition, continually helpful, patient and supportive during every single stage in this work, allowing exploring freedom, encouraging continuous self evaluation, and most importantly amending my never-ending pitfalls. Special thanks to him for enriching my vocabulary and idiom lists; it has been always exciting when I first try to grasp the meaning and then eventually learn how to use them by listening to his speech or reading his emails. I would say, he is a brilliant author. I have enjoyed my years learning from him scientifically and personally. More than that, working with him has been a great pleasure that is giving birth to great opportunities during my career. Thank you very much for everything!

Sincere thanks and appreciation go to my PhD committee advisors, Bill Coish and Michael Hilke, for their valuable evaluation, insightful feedback and support over all the years. It was a great pleasure to have this opportunity.

I also have had the pleasure of working with all Sankey lab members and I am grateful for their support at all times. Thanks for Tina Muller for being a smart young mentor and a great friend. Special thanks for helping with COMSOL simulations, coding, physics, life and of course for sharing hotel rooms in conferences. Thanks for Christoph Reinhardt for developing and sharing the trampoline fabrication knowledge which he used to produce the first two 100 nm thick devices, and for helping with the development of the fiber interferometer apparatus. Thanks for Simon Bernard for his help with ProTEK stripping, for automating the lock in, eliminating the classical laser noise, and his help with the characterization of the mechanical modes Brownian motion. Thanks for Raphael St-Gelais for being a knowledgeable fabrication advisor. Special thanks for showing me how to clean the photomask, for the suggestion of coating the devices with SiO_2 layer and for all other super useful tips used in the fabrication

and in the interferometric apparatus troubleshooting. Thanks for Alexandre Bourassa and Chris McNally for the design, the assembly and the setting up of the interferometric chamber and circuit. Thanks for Yishu Zhou for her helpful committed work on the initial testing steps towards phononic crystals mechanical modes characterization and for her help with coding. Thanks for Bogdan Piciu for introducing me to COMSOL and for all useful discussions. Thanks for Maximilian Ruf, Alexandre Bourassa, Erika Janitz and Lilian Childress for the training and the beneficial discussions they have shared during the initial time I spent with them in the optical fiber laser ablation project. Thanks for Vincent Dumont and Zack Flansberry for all the useful and nice discussions. I also want to take this opportunity to thank all Childress lab members for being friendly colleagues and for sharing some lab tools. Thanks all for all great memorable times we spent together during groups outings and enjoyable barbeques!

I owe a great deal to the excellent team in the McGill microfabrication facility. I especially wish to thank Sasa, Matthieu, Jun Li, Lino, Donald, Peng and Zhao for all the fantastic hands-on training, on demand help and all the fruitful discussions. Millions of thanks to all my clean room colleagues Menouer, Roksana, Mohannad, Paresa and Yong-Ho Ra for creating vibrant and safe work atmosphere and for the useful discussions.

Many thanks go also to all the professional, technical and administration staff in the physics department, Robert, John, Richard, Janney, Mario, Eddie, Bianca, Carolina, Sonia, Alba, Diane and Louise. They are always friendly and willing to help.

My years in graduate school would not have been magnificent without my friends. I don't think it would be possible to name everyone here, but I will always appreciate their sincere friendship, my dear Lili, Rabab, Muna, Arwa, Priscila, Dima, Fatima, Susan, Roksana and Hala. Thanks for all the coffee breaks, lunch, dinner and shopping times we have had together.

I owe a huge debt of gratitude to the honest love and the infinite support my family has been always providing. To the pure soul of my father, my greatest figure who got me started down this path and my first and best ever math and science teacher. To the source of my proudness and strength, my mother, for her prayers, for her solid faith and trust in me. Million thanks for taking the time and effort to telephone me everyday from Jeddah, for

FedExing everything I want from homeland, for lending an ear at all times, and for being my warm harbor always. To my husband for his unique wisdom and kindness, for being always up for all kinds of discussions, for his company in all thin and thick matters, and of course for taking me always to Laser Quest. To my kids for their infinite innocence, warm hugs and angelic smiles, all of which have been the best cure ever. To my brother, his wife and my sisters for believing in me, for all inspirations, and for the 24 hours / 7 guidance and helping hot lines. To all my nieces and nephews for their warm emotions and sincere respect. To my second father, my kind uncle, for being always generous and ready to help in all kinds of issues. I could not go without mentioning my mother and father in law for their absolute kindness and encouragement. Thank you very much!

I tremendously acknowledge the generous funding and the logistics support I received from King Abdulaziz University scholarship, the Saudi Arabian Cultural Bureau in Canada and the Sankeylab.

Statement of Originality

The author, Abeer Z. Barasheed, declares that the following materials of this dissertation to be considered original scholarship and distinct contribution to knowledge:

- *Optically defined mechanical geometry* [1]. [Puplished: Abeer Z. Barasheed, Tina Muller, and Jack C. Sankey, PHYSICAL REVIEW A 93, 053811 (2016)]
- The fabrication of large area (thousands and hundreds of unit cells) delicate suspended Si_3N_4 phononic crystal membranes and the initial characterization. [Manuscript will be prepared soon: Abeer Z . Barasheed et al. (2017)]

Contribution of co-Autohrs

- Chapter 2 is based on the published manuscript:

  Optically defined mechanical geometry [1]

  Abeer Z. Barasheed, Tina Muller, and Jack C. Sankey

  PHYSICAL REVIEW A 93, 053811 (2016)

  - One-dimensional model: Abeer Z. Barasheed and Jack C. Sankey performed the 1D calculations in parallel.
  - COMSOL calculations: Abeer Z. Barasheed performed all COMSOL simulations. Tina Muller helped with trapping and anti-trapping simulations and the initial code for plotting them. Jack C. Sankey supervised the project and provided: the idea of the paper, a great deal of help in coding and useful tips in COMSOL. All the authors wrote the manuscript.

- Chapter 3: Fabrication of stoichiometric silicon nitride phononic crystal membranes

  - Fabrication: Abeer Z. Barasheed designed the devices, wrote the majority of the photomask code and performed all fabrication of phononic crystal membranes. Christoph Reinhardt developed original trampoline fabrication [2], upon which this work is based and produced the first two devices of 100 nm. Simon Bernard helped with ProTEK stripping. Raphael St-Gelais cleaned the photomask and provided useful tips used in fabrication (SiO_2 layer, piecewise dry etching). Jack C. Sankey provided the fabrication ideas and guided all stages of the whole work. He also wrote a couple of primitive functions upon which the photomask code was based, and helped fix a memory issue in the gdspy library.
  - Mechanical modes characterization: The interferometric system used to probe the mechanical modes has been constructed by many people over the years. Alexander Bourassa designed and (together with Chris McNally) built the original chamber. Christoph Reinhardt helped develop the circuitry and software. He also redesigned

the stage mounts and assembled the new elements with the encoded XY stage. Abeer Z. Barasheed incorporated the Z-stage biasing circuitry and worked on some of the software. Simon Bernard automated the lock-in, eliminated classical noise peaks, and helped characterize the mechanical mode's Brownian motion. Yishu Zhou worked on some of the software and performed some initial interferometric troubleshooting and testing. Raphael St-Gelais provided useful tips for fiber interferometry troubleshooting and testing. Jack C. Sankey wrote the automating code for XY stage and Lock in measurements and supervised everything.

Contents

Chapter 1

Introduction

Solid-state mechanical systems are ubiquitous throughout society, from oscillators in time-keeping devices to accelerometers and electronic filters in automobiles and cell phones. They also comprise an indispensable set of tools for fundamental and applied science. For example, using tiny mechanical systems, it is possible to "feel around" surfaces at the atomic scale [3], detect mass changes from adsorbed chemicals with single-proton resolution [4], and sense the gentle magnetic "tugs" from individual electron spins [5], persistent currents in a normal-metal ring [6], or even element-specific nanoscale clusters of nuclei [7]. Meanwhile, human-scale masses (positioned kilometers apart) currently "listen" for gravitational waves emitted by violent events across the universe [8]. In the field of optomechanics [9], the forces generated by light provide a means of tuning the fundamental properties of mechanical systems at every size scale, namely their dissipation, frequency, normal-mode geometry, and effective mass.

The dissipation and frequency have been particularly well controlled, often tuned by many orders of magnitude using various techniques [9]. On the dissipation side, Cohadon *et al.* [10] used (for the first time) the radiation pressure forces applied by a feedback loop to cool down the Brownian motion of the fundamental mode of a mirror oscillator by a factor of 20. They also showed that, by reversing the sign of the electronic gain of the feedback loop, they can heat the mirror motion and increase its quality factor. In another effort, bolometric effects were used to tune the mechanical properties [11, 12, 13]. For example, Zalalutdinov *et al.* [11] demonstrated the possibility to increase the quality factor of a silicon disk (mirror-like) oscillator by an order of magnitude using bolometric (or photothermal)

radiation pressure forces. On the other hand, bolometric radiation pressure was used by Metzger *et al.* [13] to suppress the oscillation amplitude of a gold-coated silicon lever and hence cool it down from room temperature to 18 K. Purely radiation pressure forces (that are not of photothermal origin) had also allowed the same level of control [14, 15, 16, 17, 18, 19]. For example, radiation pressure forces were used (for the first time) by Carmon *et al.* [14] and Kippenberg *et al.* [15] to induce large amplitude oscillations (oscillation instability) in silica microtoroids. The amplitude of these oscillations (for instance in the later study) exceeded the thermally driven ones by two orders of magnitude. Moreover, Schliesser *et al.* [18] used, for the first-time, cavity induced radiation pressure forces to cool down (and hence decrease the oscillation amplitude of) a microtoroid oscillator from room temperature to 11 K. We emphasize here that the Cohadon [10] result involved electronic feedback to achieve cooling, whereas in these examples the cavity resonance is exploited to achieve the same thing.

On the frequency side, the strong tuning has been allowed through the optical spring effect (optical trapping) [9]. In [20], Corbitt *et al.* experimentally illustrated (for the first time) the trapping (frequency increase) of a gram-scale mirror from $\sim$ 170 Hz to 5kHz, demonstrating a column of light can be stiffer than a piece of diamond (but much more brittle!). In another study, Ni *et al.* [19] demonstrated the ability of light to increase the frequency of a suspended silicon pendulum, placed in a standing wave in an optical cavity, by many orders of magnitude, which also served to increase the mechanical Q by a factor of 50.

The geometry and mass have also been tuned via optically mediated normal-mode hybridization [19, 21, 22, 23, 24, 25, 26]. For example[1], besides the ability to increase the frequency of the silicon pendulum, Ni *et al.* [19] were able to hybridize two of this (single) pendulum mechanical modes using the optical spring effect. In another study, Lin *et al.* [21] showed that they can couple the "swinging" mechanical modes of separate nanobeams, each having a nanophotonic cavity, using the spring-like optomechanical forces in the nearfield of their cavity modes. When one of the cavities is driven at a frequency that is far from its resonance the two nanobeams vibrate independently. As the drive approaches the cavity resonance the strength of the coupling optical spring increases and the two nanobeams

[1] This is not the first demonstration of the concept but it is a clear example.

start to vibrate together (in phase or out of phase). Interestingly, this optically mediated mode hybridization was demonstrated by Shkarin *et al.* [25] in the membrane-in-the-middle fiber cavity system. Two degenerate modes of a stressed square silicon nitride membrane were coupled purely optically when a surrounding optical cavity was driven close to its resonance. This optical spring coupling allowed them to demonstrate energy transfer (with 40% efficiency) between the unperturbed modes. Also, optically driven synchronization of two optomechanical silicon nitride oscillators with different frequencies was demonstrated by Zhang *et al.* [23]. In this study, the "flapping" modes of two optical ring resonators are coupled through the evanescent optical field present in a small gap between them. This coupling resulted in the generation of two modes where the oscillators oscillate symmetrically and asymmetrically together. The off/on switching of the synchronization was enabled by tuning the relative optical resonance of the two oscillators by bolometric effects. In another study by Fu *et al.* [26], the mechanical modes of two elastically coupled freestanding cantilevers were hybridized through the optical tuning of one of the cantilevers oscillations in a fiber cavity. Importantly, these examples reveal that the optical tuning of geometry and mass is not so profound: In all of these studies, only a few (essentially two) normal modes are involved, and the resulting hybridized modes therefore exhibit a mass and spatial extent comparable to that of the unperturbed modes.

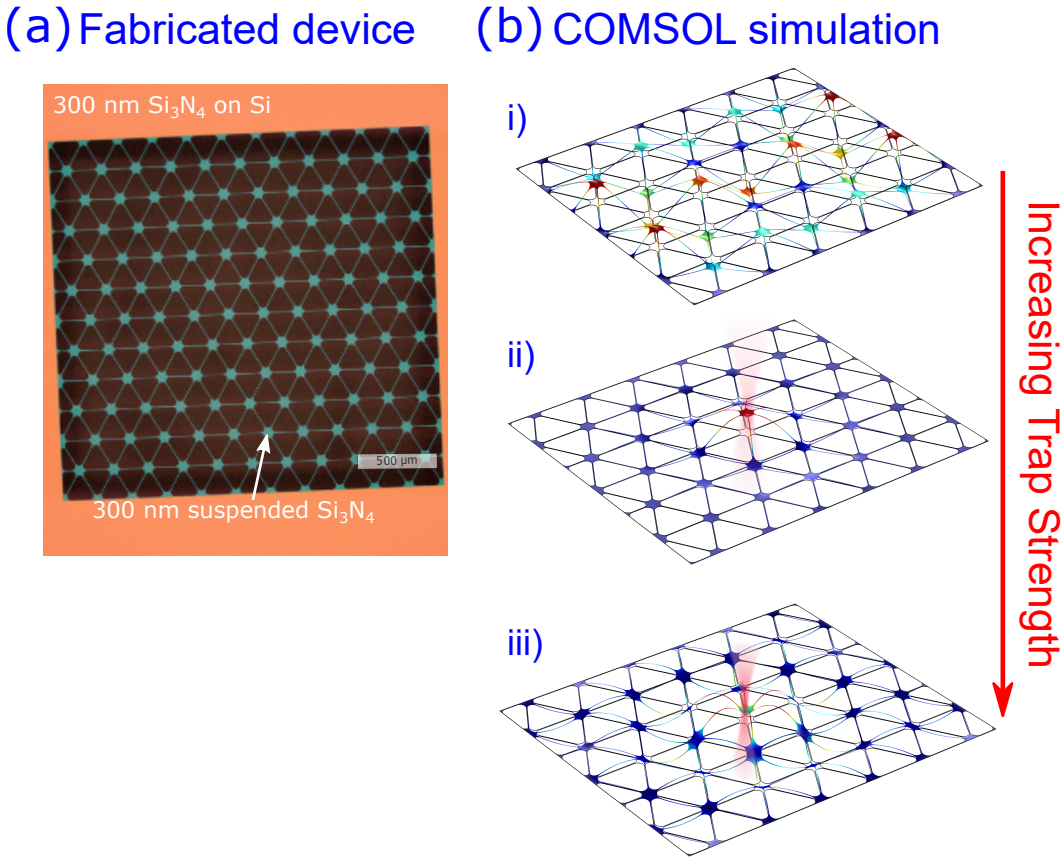

Figure 1.1: The new idea of this dissertation. (a) An example of a fabricated device. (b) The intensity of the laser field (i, ii, and iii) affects the amount (and spatial distribution) of oscillating mass in the phononic crystal membrane, which will provide a new (and previously unexplored) level of control.

In this dissertation, we propose and demonstrate some initial steps toward exploiting radiation pressure to *strongly tune* the geometry and mass of a mechanical system. The basic idea is to fabricate an extended phononic crystal structure [27] (an example device from Chapter 3 is shown in figure 1.1 (a), and apply an optical trap to one lattice site, thereby creating a defect that exponentially localizes one or more mechanical modes (a simulated mode evolution from Chapter 2 is shown in figure 1.1 (b)). We show that, unlike structurally defined defect modes [27], realized some time ago [28] and currently exploited with extraordinary success in optomechanics [29, 30, 31, 32, 33, 34, 35, 36, 37], the spatial extent and mass of optically defined defect modes can be tuned by many orders of magnitude using a realistic, chip-scale optomechanical geometry. Additionally, despite the comparatively weak optomechanical interaction with each of the unperturbed, extended mechanical modes, we

estimate that an optical trap having an average intracavity power corresponding to a single photon should, in principle, cause a macroscopic, measurable change in the amplitude of a millimeter-scale mechanical system. Moreover, we show that a larger structure will exhibit a larger response to a given trap, despite its larger mass.

It is currently not possible to achieve this level of in situ control over the geometry of a solid-state mechanical system, so these results provide a curious set of opportunities. For example, it is well known that partial optical levitation improves the coherence of mechanical elements [19, 38, 39, 40, 41, 42], and the addition of spatial localization would further isolate the system from the lossy clamped boundaries [43, 44, 45, 46, 47]. Along these lines, the ability to systematically tune a mechanical mode's interaction with the boundaries (or other fabricated structures) provides access to unique studies of dissipation mechanisms, a subject of central interest to all mechanical technologies. Specifically, instead of fabricating many (nominally) identical devices with systematically varied shapes, one could fabricate a single mechanical crystal and optically tune the mode shape to help separate the roles of bulk bending, clamping, or other structural losses. On a more fundamental side, this light-geometry interaction might aid in the pursuit of macroscopic quantum motion [31, 32, 48, 49, 50, 51, 52]. An immediately interesting question is how a large crystal, perhaps driven to very large amplitude, might evolve under the influence of a single cavity photon, a superposition of photon states, or squeezed light. If it is possible to generate large-amplitude superpositions or other nonclassical motional states with a sufficiently massive crystal, this could perhaps even provide a platform for tests of mechanisms leading to the collapse of macroscopic quantum behavior [53]. Alternatively, this system could be used to approach the goal of quantum state transduction [33, 54, 55, 56, 57, 58, 59, 60] from a different direction: a trap toggling the spatial extent of a mechanical mode could be used to toggle its interaction with an object at a different lattice site, e.g., a qubit or another optical resonator (perhaps operating at a very different wavelength). Finally, by intentionally adding spatial disorder (speckle) to the trapping field, it would be possible to perform controlled studies of Anderson localization [61] of phonons in one or two dimensions. Ultimately, however, it is our hope that this added control will inspire a set of nontraditional optomechanics and sensing applications beyond those naively imagined here.

The initial steps toward achieving these goals are as follows:

1. Develop a guiding intuition about the physics of laser localization.
2. Use numerical simulations to design realistic devices enabling this physics.
3. Develop a reliable fabrication technique for the requisite mechanical structures.
4. Characterize their unperturbed mechanical spectra to verify feasibility.
5. Demonstrate this localization.

This dissertation addresses the first four points and is organized as follows. Chapter 2 introduces a simple classical theory for these systems, beginning with a semianalytical toy model in one dimension (1D). We derive some key figures of merit and perform a minor optimization. Then we apply this intuition to guide the design of a realistic two-dimensional implementation accessible by our research group. Then, in chapter 3, we discuss several fabrication techniques based on standard photolithography (to produce stoichiometric silicon nitride phononic crystal membranes, figure 1.1 (a)), finding that, by protecting these delicate structures from the chemical etchant during release, we can boost the yield to more than 85%. This allows us to consistently fabricate 100 nm to 300 nm thick stoichiometric Si_3N_4 freestanding crystals with an area as large as 20 mm^2, up to 2750 crystal unit cells, and tethers as narrow as $\sim$ 1.5 μm. These devices indeed exhibit the phononic bandgap (with a ratio of gap width to band edge frequency as high as 80 %) required for laser-induced localization experiments, as confirmed by preliminary mechanical characterization. Finally, we present a summary to highlight the key results of this dissertation and the next steps for the near future in chapter 4.

Chapter 2

One dimensional model and two dimensional COMSOL simulation

The goals of this chapter are to build a simple picture for the physics of laser localization in one-dimension (1D), and, accordingly, employ this to design a realistic device (using finite element (FEM)) made of stochiometric Si_3N_4. Importantly, we find that it is possible to vary the spatial extent and the amount of participating mass in these optically defined defect modes by many orders of magnitude (see, for example, the simulation of figure 1.1 (b)), and that light at the level of a single photon, in a realistic cavity trap, can in principle cause a measurable change in the mode of a millimeter-scale membrane. Furthermore (and perhaps counterintuitively) we predict that large structures will have a larger response to a given trap as compared to small structures. We find surprisingly good agreement between our 1D model and the 2D simulation, with the 1D model predicting band edge frequencies within ~ 20 % of those simulated, and a semi-quantitatively similar response to an applied optical trap. We present in section 2.1 the 1D toy model. Then in section 2.2, we demonstrate the design of realistic two-dimensional (2D) system in COMSOL[1]. Finally, we summarise the key results in section 2.3.

[1]COMSOL Multiphysics® Modeling Software: https://www.comsol.com/

2.1 First Principles: Analytical Model in 1D

The systems we envision for accessing the physics of laser localization comprise a millimeter-scale freestanding sheet of stoichiometric silicon nitride ($\sim$ 100 nm thick Si_3N_4 on a single-crystal silicon frame), patterned into a periodic structure (phononic crystal, see figure 1.1 (b)), with optical forces applied to a single unit cell. Due to high temperature deposition and mismatched thermal expansion coefficients, Si_3N_4 is under $\sim$ 1 GPa of stress at room temperature, and is therefore well described by the "ideal drum limit", wherein the wave properties are entirely determined by the stress and mass density. In this section, we build intuition with a one-dimensional (1D) toy model comprising an ideal string under tension with periodically alternating mass density. In section 2.1.1, we review the basic properties of such a string without a light field, in particular deriving the dispersion and identifying (and maximizing) the phononic bandgap for transverse acoustic waves. Then in section 2.1.2 we incorporate a local optical trap, modeled as a uniform spring constant density over a small region of one unit cell, identify a resulting defect mode, and study the mode shapes and the effective mass change as a function of trap strength. Then, under the weak trap approximation, we analytically derive the defect frequencies and localization length (effective mass) as a function of the trap strength. We derive a few figures of merit for this style of optomechanical coupling to assess the localization efficiency, namely the localization length (and effective mass) and the ratio of the trapped pad's amplitude with the trap on and off for a fixed mechanical energy stored in the mode. We find that the localization length (and effective mass) scale as the inverse square of the trap power; even for an infinite lattice, this implies an infinitesimal trap will lead to a finite mechanical mode mass. Counterintuitively, we also find that the mechanical response to fixed trap power can increase for larger, more massive structures.

2.1.1 Phononic crystal ideal string under tension

Here we develop a basic intuition for an unperturbed, infinite phononic crystal system by considering a string of periodically alternating mass density under tension. This structure can be understood as a Bragg mirror for transverse waves. In section 2.1.1.1, we calculate

the dispersion identifying bands of frequencies wherein waves will propagate in the crystal, and "bandgaps" wherein they will not. Then in section 2.1.1.2, we discuss some rules for maximizing the size of the bandgap (and hence the degree of localization when trapped).

2.1.1.1 Transverse wave dispersion & modes of propagation (eigenvalues & eigenvectors)

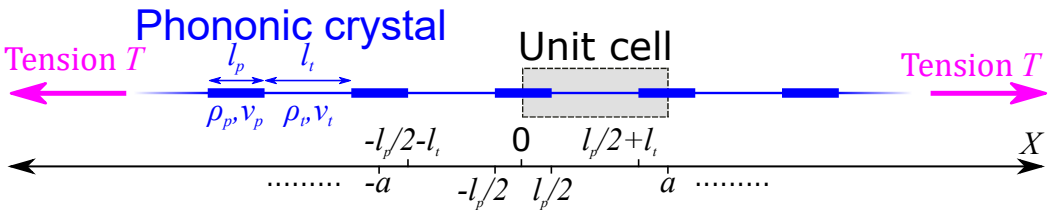

Figure 2.1: Infinite phononic crystal string under tension (T) with pad (tether) mass densities ρ_p (ρ_t), lengths l_p (l_t), and wave speeds v_p (v_t). The unit cell mass $m_{unit} = \rho_p l_p + \rho_t l_t$ and length $a = l_p + l_t$.

We first consider an infinitely long, ideal string under tension (T), with periodically alternating mass density $\rho(x)$, which takes on values ρ_p in the heavier "pad" region and ρ_t in the lighter "tether" region, as drawn in figure 2.1. The unit cell length is $a = l_p + l_t$, where l_p (l_t) is the pad (tether) length. The local wave equation of this system is

$$T\frac{\partial^2 y(x,t)}{\partial x^2} = \rho(x)\frac{\partial^2 y(x,t)}{\partial t^2}, \tag{2.1}$$

where x is the position, t is the time and $y(x,t)$ is the transverse displacement. The time dependent solution to equation 2.1 is

$$y(x,t) = y(x)e^{-i\omega t}, \tag{2.2}$$

where ω is the frequency. The spatial solution in any segment $y(x)$ is the sum of a left and right moving wave. Let A_{x_0} (B_{x_0}) be the local complex amplitude of the right-moving (left-moving) wave at location x_0. Within a pad or tether,

$$A(x) = A_{x_0}e^{ik_{p,t}(x-x_0)} \tag{2.3}$$

$$B(x) = B_{x_0} e^{-ik_{p,t}(x-x_0)} \tag{2.4}$$

where $k_{p,t}$ is the (pad, tether) wave number. The full local solution is

$$y(x) = A(x) + B(x), \tag{2.5}$$

Plugging equation 2.2 into equation 2.1 yields the familiar ideal string dispersion

$$\frac{\omega}{k_{p,t}} = \sqrt{\frac{T}{\rho_{p,t}}}, \tag{2.6}$$

from which we identify the local wave velocity, $v_{p,t} = \sqrt{\frac{T}{\rho_{p,t}}}$.

When crossing the boundaries between tethers and pads, however, the relationship between amplitudes becomes more complicated, as part of the waves will be reflected. To figure out what the whole structure is doing, we follow a "transfer matrix" approach [62]. The amplitudes of any two points at locations x_n and x_m can be related by a transfer matrix M as

$$\begin{bmatrix} A_{x_n} \\ B_{x_n} \end{bmatrix} = M \begin{bmatrix} A_{x_m} \\ B_{x_m} \end{bmatrix} \tag{2.7}$$

As discussed below, writing the relationship this way is mathematically convenient, because, if we know the transfer matrices of several features of a structure (e.g. propagation through a pad, a pad-tether boundary, propagation through a tether, etc), the relationship between the amplitudes at the ends of the structure will be a simple matrix multiplication.

We consider the unit cell of figure 2.1. We start with arbitrary amplitudes at the center (origin), $x = 0$, of the central pad, $\begin{bmatrix} A_0 \\ B_0 \end{bmatrix}$. The amplitude at the end of this pad ($x = p, end$), $\begin{bmatrix} A_{p,end} \\ B_{p,end} \end{bmatrix}$, can be related to that at the origin using the propagation matrix through a half pad of length $l_p/2$, M_{hp}as

$$\begin{bmatrix} A_{p,end} \\ B_{p,end} \end{bmatrix} = M_{hp} \begin{bmatrix} A_0 \\ B_0 \end{bmatrix} = \begin{bmatrix} e^{ik_p l_p/2} & 0 \\ 0 & e^{-ik_p l_p/2} \end{bmatrix} \begin{bmatrix} A_0 \\ B_0 \end{bmatrix}. \tag{2.8}$$

Imposing that the solution $y(x)$, equation 2.5, and its first derivative must be continuous across boundaries between different regions[2], we can relate the amplitudes across the pad-tether $\left(\begin{bmatrix} A_{p,end} \\ B_{p,end} \end{bmatrix} - \begin{bmatrix} A_{t,start} \\ B_{t,start} \end{bmatrix} \right)$ interface using a transformation matrix at pad-tether interface, M_{pt} as

$$\begin{bmatrix} A_{t,start} \\ B_{t,start} \end{bmatrix} = M_{pt} \begin{bmatrix} A_{p,end} \\ B_{p,end} \end{bmatrix} = \begin{bmatrix} t_{pt} - \frac{r_{tp} r_{pt}}{t_{tp}} & \frac{r_{tp}}{t_{tp}} \\ -\frac{r_{pt}}{t_{tp}} & \frac{1}{t_{tp}} \end{bmatrix} \begin{bmatrix} A_{p,end} \\ B_{p,end} \end{bmatrix}, \tag{2.9}$$

where the reflection and transmission coefficients for waves in a pad incident on a pad-tether interface are

$$r_{pt} = \frac{v_t - v_p}{v_t + v_p}, \tag{2.10}$$

$$t_{pt} = \frac{2v_t}{v_t + v_p}. \tag{2.11}$$

Similarly, the reflection and transmission coefficients for waves in a tether incident on a tether-pad interface are

$$r_{tp} = \frac{v_p - v_t}{v_t + v_p}, \tag{2.12}$$

$$t_{tp} = \frac{2v_p}{v_t + v_p}. \tag{2.13}$$

The matrix for propagating through a full tether length l_t, M_t, allows us to relate the amplitude of the wave at the beginning of the tether, $\begin{bmatrix} A_{t,start} \\ B_{t,start} \end{bmatrix}$, to that at the end of it, $\begin{bmatrix} A_{t,end} \\ B_{t,end} \end{bmatrix}$ as

$$\begin{bmatrix} A_{t,end} \\ B_{t,end} \end{bmatrix} = M_t \begin{bmatrix} A_{t,start} \\ B_{t,start} \end{bmatrix} = \begin{bmatrix} e^{ik_t l_t} & 0 \\ 0 & e^{-ik_t l_t} \end{bmatrix} \begin{bmatrix} A_{t,start} \\ B_{t,start} \end{bmatrix}, \tag{2.14}$$

and the transfer matrix of the tether-pad interface, M_{tp}, can be found by simply reversing the indices "t" and "p" in equation 2.9; hence we can write the amplitudes across the interface

[2] Otherwise, the wave would be broken or have infinite energy density at the discontinuity.

between the tether end and the begining of next pad as

$$\begin{bmatrix} A_{p,start} \\ B_{p,start} \end{bmatrix} = M_{tp} \begin{bmatrix} A_{t,end} \\ B_{t,end} \end{bmatrix} = \begin{bmatrix} t_{tp} - \frac{r_{pt}r_{tp}}{t_{pt}} & \frac{r_{pt}}{t_{pt}} \\ -\frac{r_{tp}}{t_{pt}} & \frac{1}{t_{pt}} \end{bmatrix} \begin{bmatrix} A_{t,end} \\ B_{t,end} \end{bmatrix}, \tag{2.15}$$

a propagation matrix through another half pad of length $l_p/2$ relates the amplitudes at the beginning and the center of the next pad, equation 2.8

$$\begin{bmatrix} A_a \\ B_a \end{bmatrix} = M_{hp} \begin{bmatrix} A_{p,start} \\ B_{p,start} \end{bmatrix}. \tag{2.16}$$

The total transfer matrix of the unit cell stack, $a = l_{p/2} + l_t + l_{p/2}$ (figure 2.1) is

$$M_{uc} = M_{hp}M_{tp}M_tM_{pt}M_{hp} = \begin{bmatrix} M_{11} & M_{12} \\ M_{21} & M_{22} \end{bmatrix}, \tag{2.17}$$

where

$$M_{11} = \frac{e^{i\omega(t_p+t_t)}(v_p+v_t)^2 - e^{i\omega(t_p-t_t)}(v_p-v_t)^2}{4v_pv_t}, \tag{2.18}$$

$$M_{22} = \frac{e^{-i\omega(t_p+t_t)}(v_p+v_t)^2 - e^{-i\omega(t_p-t_t)}(v_p-v_t)^2}{4v_pv_t}, \tag{2.19}$$

$$M_{12} = \frac{i(v_p^2 - v_t^2)\sin(\omega t_t)}{2v_pv_t}, \tag{2.20}$$

$$M_{21} = \frac{i(v_t^2 - v_p^2)\sin(\omega t_t)}{2v_pv_t}, \tag{2.21}$$

where and $t_t = \frac{v_t}{l_t}$, $t_p = \frac{v_p}{l_p}$ are the wave's "time of flight" in tethers and pads respectively, and the wave amplitudes after a unit cell propagation is given by equation 2.7 as

$$\begin{bmatrix} A_a \\ B_a \end{bmatrix} = \begin{bmatrix} M_{11} & M_{12} \\ M_{21} & M_{22} \end{bmatrix} \begin{bmatrix} A_0 \\ B_0 \end{bmatrix}. \tag{2.22}$$

Next, since $\rho(x)$ is periodic and invariant under the spatial translation by the lattice constant ($a = l_p + l_t$), the solutions to equation 2.6 must satisfy Bloch periodicity condition for infinite structures [63]

$$y(x+a) = (e^{iK_b a})y(x), \tag{2.23}$$

where K_b is the Bloch wave number, this can be written more generally as

$$y(x+na) = (e^{iK_b a})^n y(x), \tag{2.24}$$

where n is the unit cell index. Imposing this periodicity condition means the wave amplitudes at the origin and at the end of the first unit cell are also related through

$$\begin{bmatrix} A_a \\ B_a \end{bmatrix} = e^{iK_b a} \begin{bmatrix} A_0 \\ B_0 \end{bmatrix}, \tag{2.25}$$

This means that every time the wave moves a unit cell, its phase changes by $K_b a$. Equating the equations 2.22 and 2.25 yields

$$\begin{bmatrix} M_{11} & M_{12} \\ M_{21} & M_{22} \end{bmatrix} \begin{bmatrix} A_0 \\ B_0 \end{bmatrix} = e^{iK_b a} \begin{bmatrix} A_0 \\ B_0 \end{bmatrix}. \tag{2.26}$$

Equation 2.26 is an eigenvalue problem, with $e^{iK_b a}$ as the eigenvalue

$$\begin{bmatrix} M_{11} - e^{iK_b a} & M_{12} \\ M_{21} & M_{22} - e^{iK_b a} \end{bmatrix} \begin{bmatrix} A_0 \\ B_0 \end{bmatrix} = 0. \tag{2.27}$$

To solve it, we set the determinant to zero

$$e^{2iK_b a} - (M_{11} + M_{22})e^{iK_b a} + M_{11}M_{22} - M_{12}M_{21} = 0, \tag{2.28}$$

assuming a lossless system (M is unitary), we have

$$M_{11}M_{22} - M_{12}M_{21} = 1. \tag{2.29}$$

This yields

$$e^{2iK_b a} - (M_{11} + M_{22})e^{iK_b a} + 1 = 0, \tag{2.30}$$

$$e^{iK_b a} = \frac{M_{11} + M_{22}}{2} \pm \sqrt{\left(\frac{M_{11} + M_{22}}{2}\right)^2 - 1}. \tag{2.31}$$

Equation 2.31 gives the two eigenvalues which lead to the relationship between ω and K_b (the dispersion). Let $S = \frac{M_{11}+M_{22}}{2}$, plugging in for M_{11} and M_{22}, equations 2.18 and 2.19 respectively, yields

$$\begin{aligned} S =& \cos(\omega t_p)\cos(\omega t_t) - \frac{v_p^2 + v_t^2}{2v_p v_t}\sin(\omega t_p)\sin(\omega t_t), & (2.32)\\ =& \frac{1}{2}\cos\left[\omega(t_p + t_t)\right] + \frac{1}{2}\cos\left[\omega(t_p - t_t)\right] + \frac{v_p^2 + v_t^2}{4v_p v_t}\left\{-\cos\left[\omega(t_p - t_t)\right] + \cos\left[\omega(t_p + t_t)\right]\right\}, \\ =& \frac{(v_p + v_t)^2}{4v_p v_t}\cos\omega(t_p + t_t) - \frac{(v_t - v_p)^2}{4v_p v_t}\cos\omega(t_p - t_t), & (2.33) \end{aligned}$$

and equation 2.31 becomes

$$e^{iK_b a} = S \pm \sqrt{S^2 - 1}. \tag{2.34}$$

Based on the value that S will take, K_b have different scenarios:

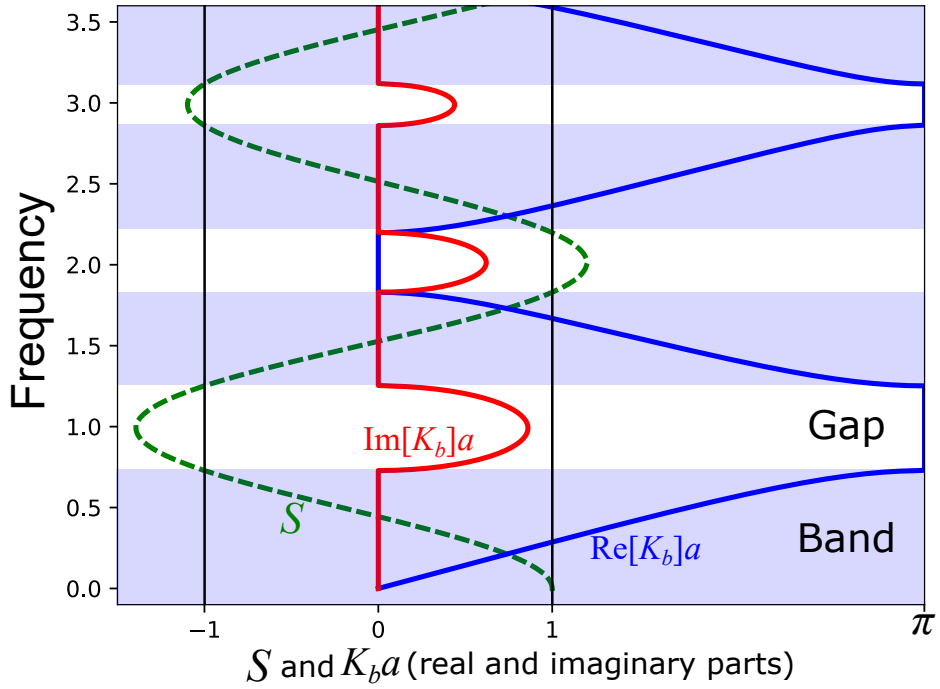

Figure 2.2: A plot shows the value of S as a function of frequency (green) and the corresponding $[K_b]\,a$ values that define the bands and the gaps for an arbitrary system

Complex eigenvalue, real K_b

If $-1 < S < 1$ (for example, the green curve in the region bounded by 1 and -1 of figure 2.2) then equation 2.34 is a complex value, and can be written as

$$e^{iK_b a} = \cos K_b a + i \sin K_b a = S \pm i\sqrt{1 - S^2}, \tag{2.35}$$

where S and $\sqrt{1 - S^2}$ are purely real,

$$\cos K_b a = S = \frac{M_{11} + M_{22}}{2}, \tag{2.36}$$

and

$$\sin K_b a = \pm\sqrt{1 - S^2} = \pm\sqrt{1 - \cos^2 K_b a} = \pm|\sin K_b a|. \tag{2.37}$$

So, equation 2.36 gives real-valued K_b as a function of ω, such that

$$\mathrm{Re}\left[K_b\right] a = \arccos(S). \tag{2.38}$$

Since cosine is periodic, there will in general be many "bands" over which this case applies, see the shaded areas of figure 2.2 (the [-1,1] green bounded S curve and the blue $\mathrm{Re}\left[K_b\right] a$ curve as a function in ω, note the zero red $\mathrm{Im}\left[K_b\right] a$ values). In this case, the magnitude of the waves does not change from unit cell to unit cell, representing propagating modes.

Real eigenvalue, complex K_b

If $S < -1$, then equation 2.34 is a negative and real value, so we can write it as follows

$$e^{iK_b a + (i\pi)} = -S \mp \sqrt{S^2 - 1}, \tag{2.39}$$

$$i\left(K_b a + \pi\right) = \ln\left(-S \mp \sqrt{S^2 - 1}\right), \tag{2.40}$$

$$K_b a = -i \ln\left(-S \mp \sqrt{S^2 - 1}\right) - \pi, \tag{2.41}$$

this is the value of the complex Bloch wave vector inside, for example, the lowest-frequency band gap in figure 2.2 . In this case, the magnitude of the waves attenuates from a unit cell to the other, representing evanescent modes. Also, if $S > 1$, then equation 2.34 is a positive and real value and written as

$$e^{iK_b a} = S \pm \sqrt{S^2 - 1}, \tag{2.42}$$

$$K_b a = -i \ln\left(S \pm \sqrt{S^2 - 1}\right), \tag{2.43}$$

this is the value of Bloch wave vector inside some gaps, purely imaginary, (for example, the second band gap in figure 2.2). Similarly, the magnitude of these waves attenuate from a unit cell to the other and hence they represent evanescent modes.

Propagating mode shapes (eigenvectors)

To calculate the propagating mode shapes, the first step is to solve the real part of equation 2.36 for ω, numerically, to obtain the edges of the lowest-frequency band gap (at $K_b = \frac{\pi}{a}$),

$$\mathrm{Re}\,[S] + 1 = 0. \tag{2.44}$$

In general, this is a transcendental equation requiring a numerical solution [3] (though under the "optimal" conditions of section 2.1.1.2, this can be solved analytically). Once we have these values (calling the lower and upper gap edge frequencies as ω_{lower} and ω_{upper} for convenience), we can calculate the eigenvectors $\begin{bmatrix} A_0 \\ B_0 \end{bmatrix}$ from equation 2.26 2.31. Assuming $A_0 = 1.0$, the first eigenvector is

$$\begin{bmatrix} A_0 \\ B_0 \end{bmatrix} = \begin{bmatrix} 1.0 \\ \frac{-M_{11}+(S+\sqrt{S^2-1})}{M_{12}} \end{bmatrix}, \tag{2.45}$$

and the second eigenvector is

$$\begin{bmatrix} A_0 \\ B_0 \end{bmatrix} = \begin{bmatrix} 1.0 \\ \frac{-M_{11}+(S-\sqrt{S^2-1})}{M_{12}} \end{bmatrix}. \tag{2.46}$$

M_{11} is given by equation 2.18, M_{12} is given by equation 2.20, and S is given by equation 2.32 . We can then propagate the modes within the pads or tethers using the corresponding local solution (equation 2.5) and propagation matrices (equations 2.8 and 2.14) and through interfaces (via equations 2.9 and 2.15) to plot the mode shapes.

For fixed values of $l_{p,t}$ and $v_{p,t}$, figure 2.3 (a) shows $\mathrm{Re}\,[K_b]$ and $\mathrm{Im}\,[K_b]$ as a function in ω and (b) shows the mode shapes spanning 10 unit cells at different frequencies labeled in (a). For low and high frequencies (shaded bands, where $\mathrm{Im}\,[K_b] = 0$), the structure supports a continuum of delocalized, propagating modes (green modes in (b)), while for frequencies in the gap (complex $[K_b]$), propagation decays exponentially (red modes in (b)).

[3] We use the bisection method to solve it.

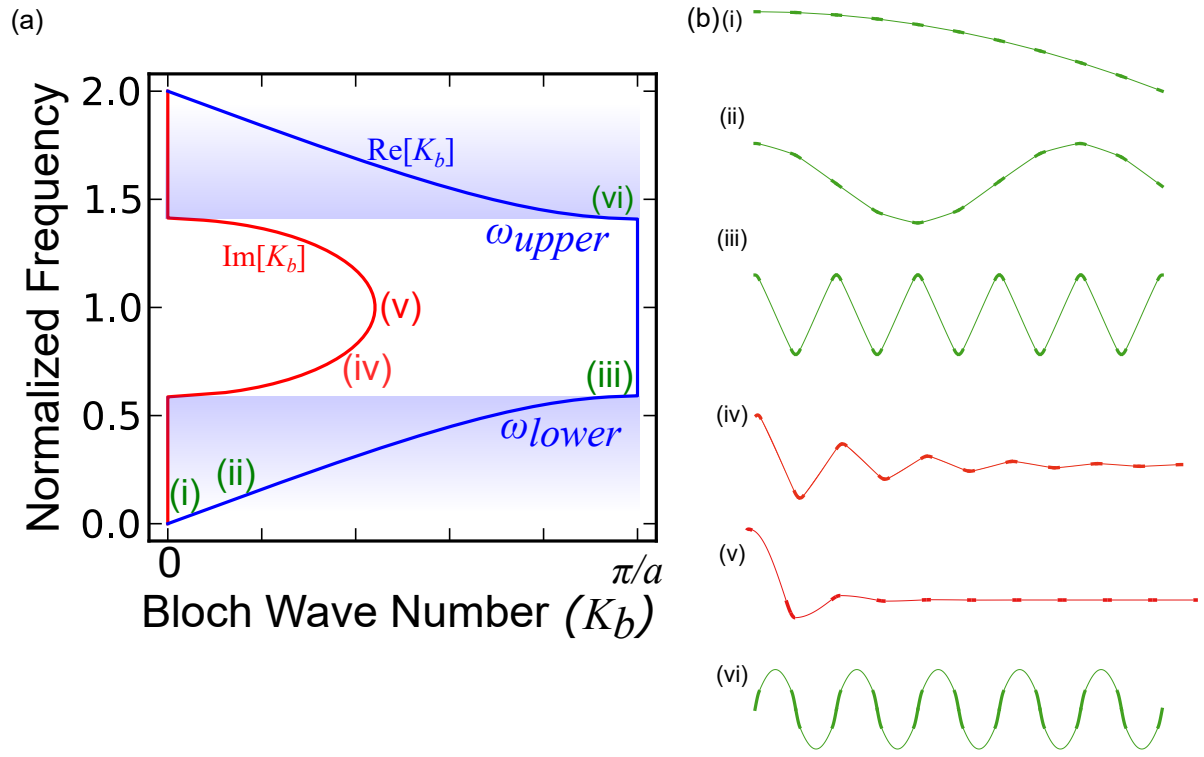

Figure 2.3: Dispersion : (a) Dependence of real (blue) and imaginary (red) components of the Bloch wave number K_b on mechanical frequency ω for the unperturbed crystal. For this calculation, $l_t/l_p = 4$ and $v_t/v_p = 4$, and all frequencies are normalized by the mid gap value $\omega_{mid} = \pi/(l_t/v_t + l_p/v_p)$. (b) Mode shapes at different ω, values are labelled by i,ii,..etc in (a)

2.1.1.2 Band gap optimization

Larger bandgaps have correspondingly larger Im $[K_b]$, meaning modes within the gap decay over shorter distances. One unitless figure of merit is therefore the size of the gap $\Delta\omega_{gap}$ relative to its mid value ω_{mid} ("gap to mid gap ratio"):

$$\frac{\Delta\omega_{gap}}{\omega_{mid}} = \frac{\omega_{upper} - \omega_{lower}}{0.5(\omega_{upper} + \omega_{lower})}, \tag{2.47}$$

which is related to the number of unit cells over which the mode decays. In our case, we are interested in maximizing the size of the first band gap. This means we are looking for the conditions that always keep S at the lowest possible value below -1. By looking at the

expression for S:

$$S = \frac{(v_p + v_t)^2}{4v_p v_t} \cos\omega(t_p + t_t) - \frac{(v_t - v_p)^2}{4v_p v_t} \cos\omega(t_p - t_t), \tag{2.48}$$

(reproduced from equation 2.33 for convenience), we note the following:

- $\omega(t_p + t_t)$ is always bigger than $\omega(t_p - t_t)$, i.e., the first term oscillates more quickly than the second.
- As $\cos\omega(t_p + t_t)$ approaches its lower bound, -1, S becomes most negative when $\cos\omega(t_p - t_t) = 1$ (or $\omega(t_p - t_t) = 0$) that is, when $t_p = t_t$.

This suggests that, if we are given v_p and v_t, we would do well to choose l_p and l_t such that

$$t_t = t_p, \tag{2.49}$$

$$\frac{v_t}{l_t} = \frac{v_p}{l_p}, \tag{2.50}$$

$$\frac{l_p}{l_t} = \frac{v_p}{v_t}, \tag{2.51}$$

This "principle of equal transit times" in fact maximizes the size of all the "odd" gaps centered at $\omega = (2n+1)\left(\frac{\omega_{upper}+\omega_{lower}}{2}\right)$ for integer n. Basically, if the speed in a segment is higher (i.e. due to lower mass density), the length of the segment should be larger in proportion to maximize the first gap. Under this condition, equation 2.33 becomes

$$S = \frac{(v_p + v_t)^2}{4v_p v_t} \cos\omega(t_p + t_t) - \frac{(v_t - v_p)^2}{4v_p v_t}, \tag{2.52}$$

which can be solved analytically to determine ω_{upper} , ω_{lower} , K_b and the modes, as discussed generally in section 2.1.1.1. To illustrate this result further, we plot the $\Delta\omega_{gap}/\omega_{mid}$ as function of l_t at fixed l_p, v_p and v_t in figure 2.4 (a), for convenience lets call $\left(\frac{v_p}{v_t}\right)$ the velocity (contrast) ratio, V_{ratio}, and $\left(\frac{l_p}{l_t}\right)$ the lengths (contrast) ratio, L_{ratio}. The figure shows how the $\Delta\omega_{gap}/\omega_{mid}$ reaches a maximum value at the optimal l_t. Like an optical Bragg mirror [64], the ratio of $\Delta\omega_{gap}/\omega_{mid}$ increases with velocity contrast V_{ratio} and is maximized when the wave transit times $t_{p,t} = l_{p,t}/v_{p,t}$ for the pad and tether are equal. This is clear when we

plot the V_{ratio}/L_{ratio}, of the same sequence of l_t, versus the $\Delta\omega_{gap}/\omega_{mid}$, figure 2.4 (b). We find that the maximum ratio happens when the $V_{ratio}/L_{ratio} = 1$, which is the condition of equal transit times 2.49. Note the curves in 2.4 are qualitatively similar to those determined by numerical optimizations for our two-dimensional systems discussed in section 2.2, figure 2.10.

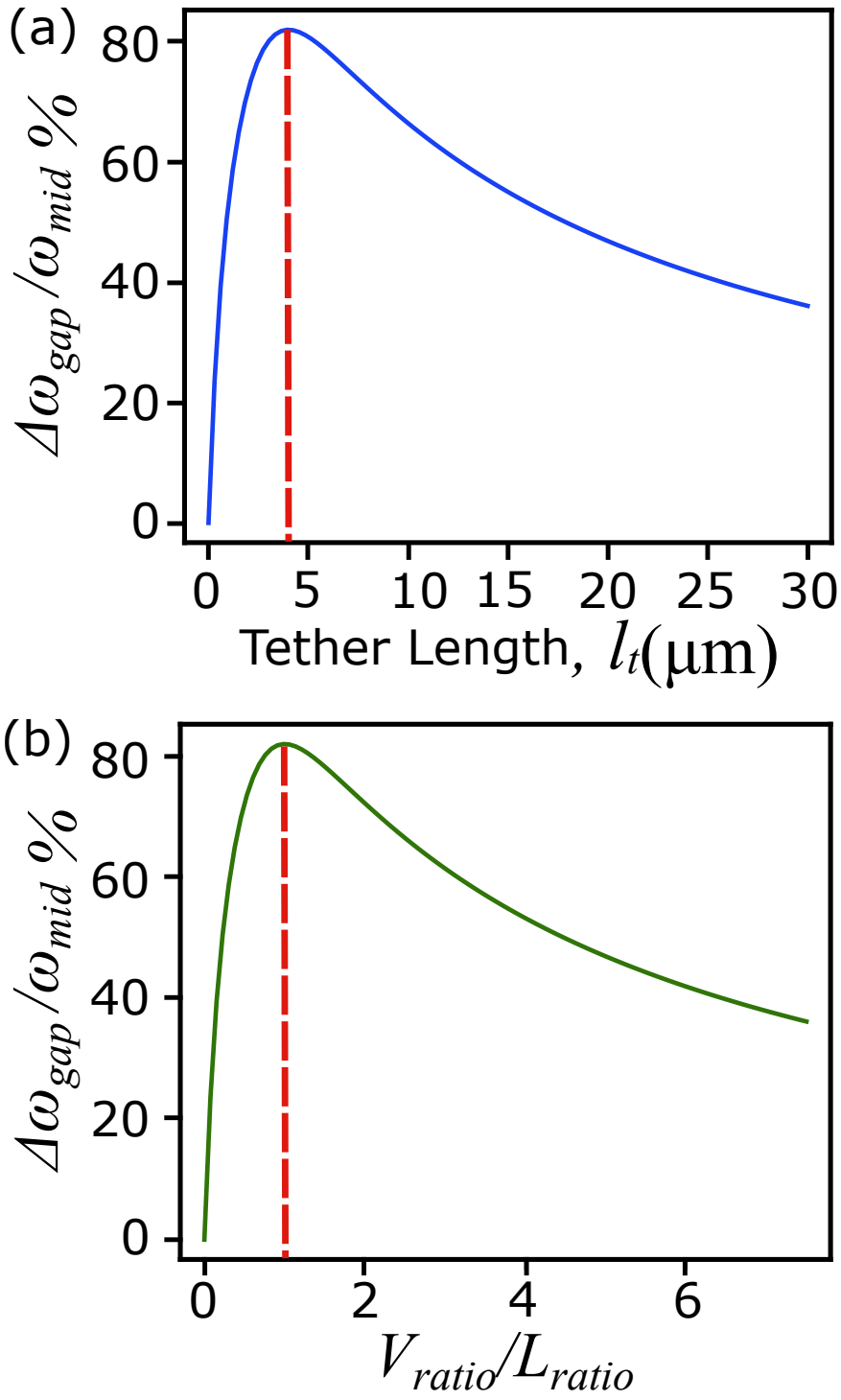

Figure 2.4: Optimum band gap ratio rules: (a) The gap ratio $\Delta\omega_{gap}/\omega_{mid}$ versus tether length l_t. (b) The gap ratio versus V_{ratio}/L_{ratio}. For this calculation, $l_p = 1$ and $v_t/v_p = 4$.

The origin of the band gap is the contrast between the wave velocities (or mass densities) in the heavy and light segments. To simplify the picture, we consider that we have satisfied

the equal transit times condition and re-parametrize the equation of S with the unitless contrast parameter V_{ratio}

$$V_{ratio} \equiv \frac{v_p}{v_t} = \frac{l_p}{l_t} = L_{ratio}, \tag{2.53}$$

so that

$$l_t = \frac{l_t}{l_t + l_p} a = \frac{a}{1 + V_{ratio}}, \tag{2.54}$$

$$t_t = \frac{l_t}{v_t} = \frac{a}{(1 + V_{ratio}) v_t} = t_p, \tag{2.55}$$

and

$$\begin{aligned} S =& \frac{-(1 - \frac{l_p}{l_t})^2 v_t^2 + (1 + \frac{l_p}{l_t})^2 v_t^2 cos(\frac{2l_t}{v_t} w)}{(4 \frac{l_p}{l_t} v_t^2)} \\ =& \frac{(1 + V_{ratio})^2}{4 V_{ratio}} \cos\left[2\omega t_t\right] - \frac{(1 - V_{ratio})^2}{4 V_{ratio}}. \end{aligned} \tag{2.56}$$

We can estimate the $\Delta\omega_{gap}/\omega_{mid}$ from this expression exactly; the lower band gap edge frequency happens when $S = -1$, so

$$\frac{(1 + V_{ratio})^2}{4 V_{ratio}} \cos\left[2\omega_{lower} t_t\right] = \frac{(1 - V_{ratio})^2}{4 V_{ratio}} - 1, \tag{2.57}$$

$$\omega_{lower} = \frac{1}{2t_t} \arccos\left[\frac{1 - 6V_{ratio} + V_{ratio}^2}{1 + 2V_{ratio} + V_{ratio}^2}\right]. \tag{2.58}$$

The mid gap frequency happens at $\omega_{mid} = \pi/2t_t$ (at $K_b = \pi/a$)

$$\Delta\omega_{gap}/\omega_{mid} = 2\left(\frac{\pi}{2t_t} - \omega_{lower}\right)\frac{2t_t}{\pi}, \tag{2.59}$$

$$\Delta\omega_{gap}/\omega_{mid} = \frac{2}{\pi} \arccos\left(-\frac{1 - 6V_{ratio} + V_{ratio}^2}{1 + 2V_{ratio} + V_{ratio}^2}\right). \tag{2.60}$$

As expected, this means that if $V_{ratio} = 0$ (no contrast), $\Delta\omega_{gap}/\omega_{mid} = 0$ (no band gap).

Interestingly, this simplified analysis for the optimal band gap size allows us to find an easy estimate for $\mathrm{Im}\left[K_b\right]$, that will help us quantify the crystal decay (localization) length, as defined in section 2.1.2.2, for frequencies in the middle of the gap, $\omega_{mid} = \pi/2t_t$. Using

equations 2.41 and 2.56, we find that:

$$\mathrm{Im}\left[K_b\right]_{(\omega=\omega_{mid})} = -\ln\left[\frac{V_{ratio}}{2} + \frac{1}{2V_{ratio}} \pm \frac{\sqrt{-2+V_{ratio}^2+1/V_{ratio}^2}}{2}\right]. \tag{2.61}$$

2.1.2 Phononic crystal ideal string under tension and subjected to an optical trap force

In this section, we expand our toy model to include the influence of an optical trap force applied to one pad of the infinite crystal. We numerically calculate the new defect (localized) frequencies, mode shapes and the effective mass in section 2.1.2.1. Then in section 2.1.2.2, we impose the weak trap approximation to exactly solve for the localized frequencies, the effective mass and the localization length as a function of trap power. Finally, besides the localization length (and the effective mass), we introduce another figure of merit, section 2.1.2.3, which is the ratio of the trapped pad's amplitude with the trap on and off for a fixed mechanical energy stored in the mode.

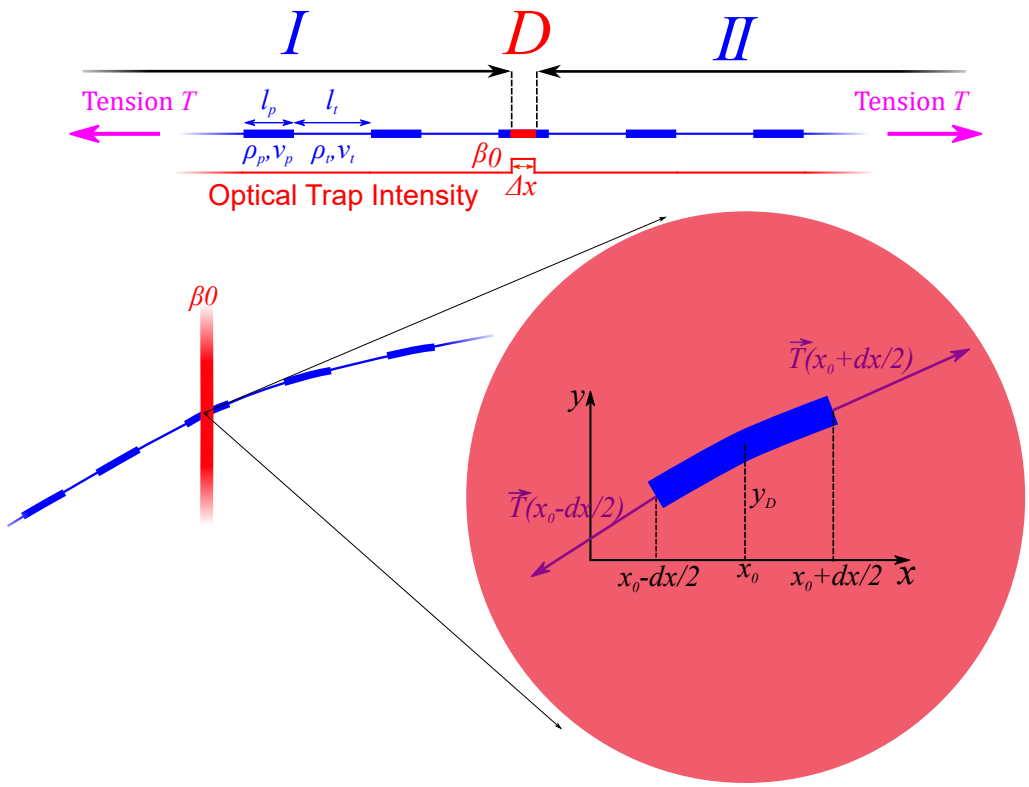

Figure 2.5: String under tension T and an optical trap $\beta(x) = \beta_0$ within $\Delta x = [-l_p/4, l_p/4]$ and zero everywhere; we consider transverse displacements only, along y.

2.1.2.1 Defect (localized) modes frequencies and shapes

We apply the optical trap to our infinite string (that has mass density, $\rho(x)$, and tension, T), figure 2.5. The optical trap is modeled as a transverse spring constant density $\beta(x)$ proportional to the average (classical) laser power or cavity occupancy n_γ [38, 39]. The total vertical force on a segment of length dx at location x_0 is given by (for small amplitudes)

$$dF_y = T\partial_x y(x_0 + dx/2) - T\partial_x y(x_0 - dx/2) - \beta(x)dxy, \tag{2.62}$$

where y is the transverse displacement, so that the local string's wave equation becomes

$$\rho(x)dx\partial_t^2 y = T\left[\partial_x y(x_0 + dx/2) - \partial_x y(x_0 - dx/2)\right] - \beta(x)dxy, \tag{2.63}$$

which, in the limit $dx \to 0$, becomes

$$\rho(x)\partial_t^2 y - T\partial_x^2 y + \beta(x)y = 0. \tag{2.64}$$

For simplicity, $\beta(x)$ is assumed to be a constant (β_0) within a region of length $\Delta x = [-l_p/4, l_p/4]$ at the center of one pad (central pad) and zero elsewhere, as illustrated in figure 2.5 (a), hence the equation of motion inside the trapped region is

$$\rho_p\partial_t^2 y_D - T\partial_x^2 y_D + \beta_0 y_D = 0. \tag{2.65}$$

where y_D is the transverse displacement in the trapped region of the central pad. The real trap will have a gaussian intensity profile with a width smaller than the pad [38, 39], which poses a difficult transfer matrix calculation. To gain quick insight, we approximate this distribution as rectangular, so that there are only two boundaries to worry about, and so that this model can be generalized to study the effect of beam size on the trapped modes.

Assuming the general wave solution 2.5 in the trapped pad region

$$y_D(x,t) = (A_D e^{ik_D x} + B_D e^{-ik_D x})e^{-i\omega t}, \tag{2.66}$$

where k_D is the wave number of the trapped pad, A_D and B_D are the complex wave amplitudes, yields

$$-\omega^2\rho_p + k_D^2 T + \beta_0 = 0, \tag{2.67}$$

or

$$\omega^2 = k_D^2\frac{T}{\rho_p} + \frac{\beta_0}{\rho_p}. \tag{2.68}$$

If we define the usual velocity $v_p^2 = T/\rho_p$, and trap frequency $\omega_{opt}^2 = \beta_0/\rho_p$, we have a dispersion relation

$$\omega = \sqrt{k_D^2 v_p^2 + \omega_{opt}^2}, \tag{2.69}$$

$$k_D = \frac{1}{v_p}\sqrt{\omega^2 - \omega_{opt}^2}. \tag{2.70}$$

Now if we trap a single pad of the infinite lattice, we have three regions with solutions that

should be tied together to fulfill the continuity condition, a region "I" spanning$\left[-\infty, \frac{-l_p}{4}\right]$, a region "$D$" spanning $\left[\frac{-l_p}{4}, \frac{l_p}{4}\right]$, and a region "$II$" spanning $\left[\frac{l_p}{4}, \infty\right]$, shown in figure 2.5. The solutions in regions I and II are those of the unperturbed equation 2.1, namely plane waves (equation 2.5) with $k_{p,t}$ wave numbers, since these regions do not see the optical trap. Given ω_{opt}, the goal is to find a frequency ω and combination of amplitudes A_D and B_D that properly connect region D to I and II having the same frequency (applying the continuity condition which determines A_I, B_I, A_{II} and B_{II} as shown in section 2.1.1). Since we want to trap the band edge mode (which is mirror symmetric about the trapping location; see figure 2.3 (b,iii), ω_{lower}) into the gap, we can restrict our search to mirror-symmetric wave functions. In this case, the mode in the pad is given by

$$y_D = A_D \cos(k_D x), \tag{2.71}$$

and we only need to connect this to the untrapped mode at one boundary (the other is redundant by symmetry). At the boundary $x = l_p/4$ in D region of figure 2.5, the amplitude and the derivative are

$$y_D(l_p/4) = A_D \cos(k_D l_p/4), \tag{2.72}$$

$$\partial_x y_D(l_p/4) = -A_D k_D \sin(k_D l_p/4), \tag{2.73}$$

The solution in region II is

$$y_{II}(x) = A_{II} e^{ik_{II}x} + B_{II} e^{-ik_{II}x}. \tag{2.74}$$

Starting with the eigenmode of the *untrapped* pad (equation 2.45), the amplitudes at the boundary of region II (A_{II} and B_{II}) are

$$\begin{bmatrix} A_{II} \\ B_{II} \end{bmatrix} = \begin{bmatrix} e^{ik_p l_p/4} & 0 \\ 0 & e^{-ik_p l_p/4} \end{bmatrix} \begin{bmatrix} A_0 \\ B_0 \end{bmatrix} = \begin{bmatrix} e^{i\omega t_p/4} \\ B_0 e^{-i\omega t_p/4} \end{bmatrix}. \tag{2.75}$$

Momentarily defining $x = 0$ at this boundary (for simplicity), the displacement and its derivative are

$$y_{II} = A_{II} + B_{II}, \tag{2.76}$$

$$\partial_x y_{II} = i\frac{\omega}{v_p}(A_{II} - B_{II}), \tag{2.77}$$

plugging in equation 2.75,

$$y_{II} = e^{i\omega t_p/4} + B_0 e^{-i\omega t_p/4}, \tag{2.78}$$

$$\partial_x y_{II} = i\frac{\omega}{v_p}\left(e^{i\omega t_p/4} - B_0 e^{-i\omega t_p/4}\right). \tag{2.79}$$

Applying the boundary conditions at this interface yields

$$A_D \cos(k_D l_p/4) = e^{i\omega t_p/4} + B_0 e^{-i\omega t_p/4}, \tag{2.80}$$

$$-A_D k_D \sin(k_D l_p/4) = ik_p e^{i\omega t_p/4} - ik_p B_0 e^{-i\omega t_p/4}, \tag{2.81}$$

The unknowns are A_D and ω, since, for a given ω, B_0 is known from equation 2.45. The first condition yields A_D

$$A_D = \frac{e^{i\omega t_p/4} + B_0 e^{-i\omega t_p/4}}{\cos(k_D l_p/4)}, \tag{2.82}$$

which can be plugged into equation 2.81, to yield the transcendental equation for ω

$$0 = i\frac{\omega}{v_p}\frac{e^{i\omega t_p/2} - B_0}{e^{i\omega t_p/2} + B_0} + k_D \tan(k_D l_p/4), \tag{2.83}$$

where k_D is given above in equation 2.70 and B_0 is given in equation 2.45.

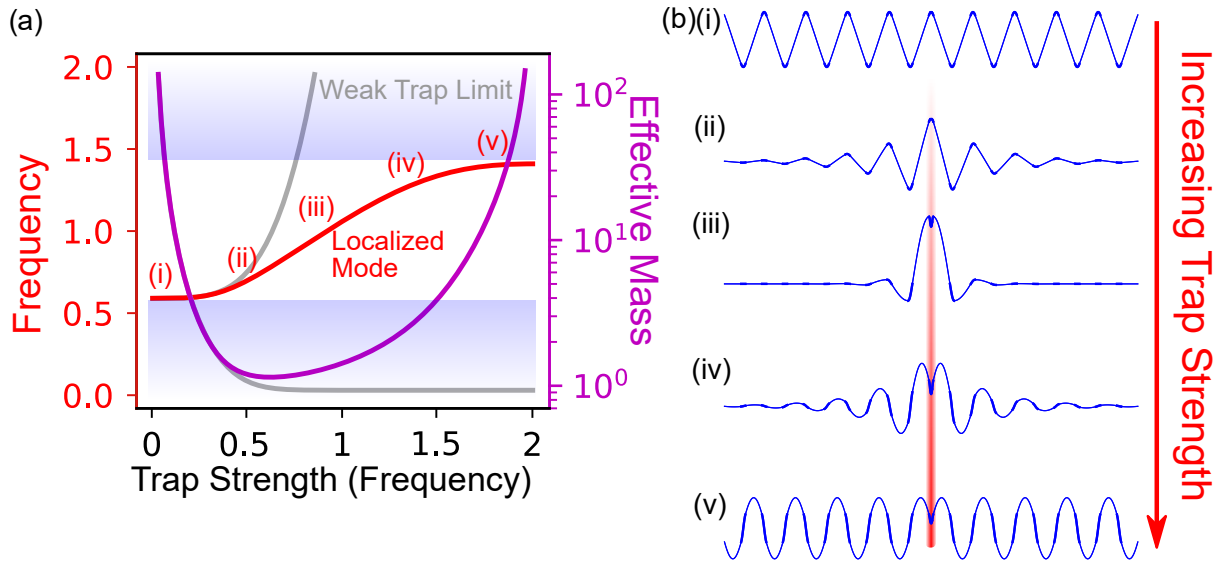

Figure 2.6: (a) Dependence of localized mode frequency (red) and effective mass (magenta, normalized by m_{unit}) on integrated trap strength $\sqrt{\beta_0 \Delta x / m_{unit}}$ (i.e., represented as the frequency of a rigid-point mass experiencing the same restoring force). Gray curves show the same calculation in the weak-trap limit for (frequency and mass). (b) Optically tuned mode shapes for values labeled in (a). The red gradient qualitatively indicates the location and intensity of the trap. For this calculation, $l_t/l_p = 4$ and $v_t/v_p = 4$, and all frequencies are normalized by the midgap value $\omega_{mid} = \pi/(l_t/v_t + l_p/v_p)$.

Solving equation 2.83 numerically (for specific system $v_{p,t}$ and $l_{p,t}$) at different ω_{opt}, yields the red curve (ω, "trapped" eigenfrequencies) in figure 2.6 (a). As expected, if $\omega_{opt} = 0$, we retain the band gap edge mode. As a function of trap strength, the mode initially "accelerates" into the band gap, then its progress slows as it approaches the upper band. Note this is not an asymptotic approach to the upper band edge; the defect mode frequency enters the upper band at finite trap power.

Once we have this eigenfrequency, we can plug it into equation 2.82 to calculate A_D above, then we can use it in equation 2.71 to plot the mode shape y_D within the trapped region, $x = [0, l_p/4]$. Then we propagate A_{II} and B_{II} in equation 2.75 using the individual transfer matrices of the previous section to produce the mode shapes. These mode shapes at different frequencies are shown in figure 2.6 (b), each mode shown is labeled with the same number as its frequency in (a). The mode, which initially is fully delocalized over the infinite string, localizes as its frequency enters the gap, it is maximally localized when the frequency is at the middle of the gap, and it then delocalizes into something resembling the upper band edge

mode at higher powers.

Effective mass

Suppose we have a specific mode shape $y(x)$. We can view this as a bunch of little segments that, under some combination of optical and material spring, oscillate up and down at frequency ω. A segment at location x of length dx, for example, has mass $dm = \rho(x)dx$, oscillates at ω with amplitude $y(x)$. Its stored energy must therefore be

$$dU = \frac{1}{2}\left[dm\omega^2\right] y^2 = \frac{1}{2}\omega^2\rho(x)y^2dx, \tag{2.84}$$

and the total energy of the structure is then

$$U_{tot} = \frac{1}{2}\left[\omega^2 \int \rho(x)\left(\frac{y}{y_0}\right)^2 dx\right] y_0^2, \tag{2.85}$$

we define y_0 to be the amplitude of the mode at some arbitrary location, such as $x = 0$. Since $y \propto y_0$ for all x, the integral as written is independent of y_0, because, for a given normal mode, y and y_0 scale together and their ratio is fixed. The term in brackets is the effective spring constant, K_{eff}, for displacement y_0 at $x = 0$, meaning the effective mass is

$$m_{eff} = \frac{K_{eff}}{\omega^2} = \frac{\int \rho(x)y^2dx}{y_0^2}. \tag{2.86}$$

To calculate the effective mass of our localized modes, we first calculate the effective mass of each section (of constant ρ). For each section, the general form of the local displacement is

$$\begin{aligned} y(x) =& Re\left[Ae^{ik_{p,t}x} + Be^{-ik_{p,t}x}\right], \\ =& Re\left[(A+B)\cos k_{p,t}x + i(A-B)\sin k_{p,t}x\right], \\ =& R\cos k_{p,t}x + I\sin k_{p,t}x, \end{aligned} \tag{2.87}$$

with $R \equiv Re\,[A+B]$ and $I \equiv Re[i(A-B)]$ and $x \equiv 0$ at the start of the region. Integrating y^2, yields

$$\begin{aligned}\int y^2 dx &= \int \left(R\cos k_{p,t}x + I\sin k_{p,t}x\right)^2 dx, \\ &= R^2\int \cos^2(k_{p,t}x)dx + I^2\int \sin^2(k_{p,t}x)dx + 2RI\int \cos(k_{p,t}x)\sin(k_{p,t}x)dx, \end{aligned} \quad (2.88)$$

and so

$$\int_0^L y^2 dx = R^2\left(\frac{L}{2} + \frac{1}{4k_{p,t}}\sin(2k_{p,t}L)\right) + I^2\left(\frac{L}{2} - \frac{1}{4k_{p,t}}\sin(2k_{p,t}L)\right) + RI\frac{1}{k_{p,t}}\sin^2(k_{p,t}L), \quad (2.89)$$

each is taken from 0 to the length L of the segment in question, where, in the last step, we have defined the start (stop) of the segment in question to occur at $x = 0$ ($x = L$) for convenience. Since $\rho(x)$ is an alternating mass (periodic), we evaluate $\int y^2 dx$ and m_{eff} for three main sections in the crystal. The trapped region of the trapped pad $x = [0, l_p/4]$, the free region of the trapped pad $x = [l_p/4, l_p/2]$ and the rest of the crystal. With this simple formula for the effective mass contribution from a single segment, we can then calculate the total effective mass of the infinite structure as the sum over the trapped pad region, the untrapped (central) pad region, and then an exponentially decaying sum of the subsequent unit cells (with relative amplitudes related by the Bloch condition). Doing so on the right-half of the structure yields $\frac{1}{2}m_{eff}$ as

$$\frac{1}{2}m_{eff} = \int_0^{l_p/4}\rho_p y^2 dx + \int_{l_p/4}^{l_p/2}\rho_p y^2 dx + \frac{\int_{\text{tether}}\rho_t y^2 dx + \int_{\text{pad}}\rho_p y^2 dx}{1 - e^{i2K_b a}}. \quad (2.90)$$

where K_b is Bloch wave vector, n is the number of unit cells. The first two terms correspond to the central (trapped) pad. The third term is the sum over subsequent unit cells, where we have used the periodicity equation 2.1.1 2.24,

$$y(x + na) = (e^{iK_b a})^n y(x), \quad (2.91)$$

to calculate the amplitude of each segment, and evaluated the geometric series for the exponential decay. For simplicity, we also scaled all waves amplitudes by that at $x = 0$ (the

center of the central pad) so that $y_0 = 1$. The magenta curve in figure 2.6 (a) shows the m_{eff} scaled by the mass of a unit cell m_{unit} at different trap strengths, where

$$m_{unit} = l_t\rho_t + l_p\rho_p = l_tT/v_t^2 + l_pT/v_p^2. \tag{2.92}$$

This definition of m_{eff} equation 2.86 is intuitively consistent with the mode profiles in 2.6 (b), as well as the functional form of the localized mode frequency [2.6 (a)]:the trap's ability to tune ω is largest when m_{eff} is small (roughly[4]).

2.1.2.2 Weak trap limit

We emphasize that for this infinite structure (i.e., having infinite untrapped m_{eff}), even an infinitesimal trap will produce a finite value of m_{eff}. In the following lines, we illuminate this behavior by extracting analytical expressions for the trapped mechanical frequency ω and the localization length $\mathscr{L} \equiv 1/\mathrm{Im}\,[K_b]$ for the case of an optimal crystal (i.e., with equal pad/tether wave transit times $t_p = t_t$, as discussed in section 2.1.1.2, and lower band edge frequency ω_{lower}) and a weak trap $\omega_{opt} \ll \omega_{lower}$.

Localized frequencies

Here we wish to estimate what happens to the band edge mode for very small traps. For the optimal case recall that (when $t_p = t_t$) the band edge mode has the frequency (see equations 2.58, 2.53)

$$\omega_{lower} = \frac{1}{2t_t}\arccos\left[\frac{1 - 6V_{ratio} + V_{ratio}^2}{1 + 2V_{ratio} + V_{ratio}^2}\right], \tag{2.93}$$

with

$$V_{ratio} \equiv \frac{v_p}{v_t} = \frac{l_p}{l_t}. \tag{2.94}$$

Suppose we apply an infinitesimal trap strength

$$\Delta \equiv \frac{\omega_{opt}^2}{\omega_{lower}^2} \ll 1, \tag{2.95}$$

[4]Note the deviation from this simple intuition arises from the choice of x_0 in equation 2.85. The trap essentially serves as a "partially clamped" region that suppresses the amplitude at x_0, leading to the "dimples" at high trap strength in figure 2.6(b), a systematically larger m_{eff}, and a reduced trap efficiency.

this will cause the band edge frequency to shift slightly

$$\omega \equiv \omega_{lower}(1+\delta). \tag{2.96}$$

For $\Delta \ll 1$, we can then expand the transcendental 2.83 into the small parameters Δ and δ. In this equation, we need to expand B_0 and k_D

$$0 = i\frac{\omega}{v_p}\frac{e^{i\omega t_p/2} - B_0}{e^{i\omega t_p/2} + B_0} + k_D \tan(k_D l_p/4), \tag{2.97}$$

where again, at $(t_p = t_t)$, equation 2.45

$$B_0 = \frac{-M_{11} + (S + \sqrt{S^2 - 1})}{M_{12}}, \tag{2.98}$$

and equation 2.52

$$S = \frac{(v_p + v_t)^2}{4v_p v_t}\cos(\omega 2t_p) - \frac{(v_t - v_p)^2}{4v_p v_t}, \tag{2.99}$$

with (equations 2.18 and 2.19)

$$M_{11} = \frac{e^{i\omega 2t_p}(v_p + v_t)^2 - (v_p - v_t)^2}{4v_p v_t}, \tag{2.100}$$

$$M_{22} = \frac{e^{-i\omega 2t_p}(v_p + v_t)^2 - (v_p - v_t)^2}{4v_p v_t}. \tag{2.101}$$

So, expanding S about $\omega = \omega_{lower}$, keeping only the leading-order terms in Δ and δ, yields

$$\begin{aligned} S \approx & \frac{(v_p + v_t)^2\left(\cos(2\omega_{lower}t_p) - 2\omega_{lower}t_p\delta\sin(2\omega_{lower}t_p)\right) - (v_p - v_t)^2}{4v_p v_t}, \\ = & -1 - (\delta S_\delta), \end{aligned} \tag{2.102}$$

with

$$S_\delta = \frac{(v_p + v_t)^2}{2v_p v_t}\omega_{lower}t_p\sin(2\omega_{lower}t_p), \tag{2.103}$$

since S passes through -1 at the band edge. We use this S expansion to expand B_0, which, after algebra gives

$$B_0 \approx B_0(\omega_{lower}) + B_\delta \sqrt{\delta}, \tag{2.104}$$

where

$$B_\delta = \frac{2v_p v_t \sqrt{2S_\delta}}{i(v_p^2 - v_t^2)\sin(\omega_{lower} t_p)}, \tag{2.105}$$

and we have used the property of the stationary (standing-wave) band edge mode

$$\begin{aligned} B_0(\omega_{lower}) =& \frac{-4v_p v_t - e^{2i\omega_{lower} t_p}(v_p + v_t)^2 + (v_p - v_t)^2}{2i(v_p^2 - v_t^2)\sin(\omega_{lower} t_p)}, \\ =& 1. \end{aligned} \tag{2.106}$$

So,

$$B_0 \approx 1 + B_\delta \sqrt{\delta}. \tag{2.107}$$

Finally, we expand k_D (keeping only terms up Δ to and δ), which is the only place the optical trap enters the problem

$$\begin{aligned} k_D \approx& \frac{\omega_{lower}}{v_p}\sqrt{1 - \Delta} \\ \approx& \frac{\omega_{lower}}{v_p} - \frac{\omega_{lower}}{2v_p}\Delta. \end{aligned} \tag{2.108}$$

Plugging all of this into the transcendental equation 2.52 and throwing away the self-canceling (unperturbed) band-edge components

$$0 \approx \frac{1}{2}\tan(\omega_{lower} t_p/4) + \frac{\omega_{lower} t_p/4}{2}\sec^2(\omega_{lower} t_p/4)\,\Delta + \frac{iB_\delta}{2cos^2(\omega_{lower} t_p/4)}\sqrt{\delta}, \tag{2.109}$$

and finally

$$\delta \approx \frac{(v_p - v_t)^2 \left(\sin(2\omega_{lower} t_p/4) + 2\omega_{lower} t_p/4\right)^2 \tan(\omega_{lower} t_p)}{32 v_p v_t \omega_{lower} t_p}\Delta^2, \tag{2.110}$$

or, in terms of ω_{opt}

$$\delta \approx \frac{(v_p - v_t)^2 \left(\sin\left(2\omega_{lower}t_p/4\right) + 2\omega_{lower}t_p/4\right)^2 \tan(\omega_{lower}t_p)}{32 v_p v_t \omega_{lower} t_p} \left(\frac{\omega_{\text{opt}}}{\omega_{lower}}\right)^4, \tag{2.111}$$

where, recall (section 2.1.2.1)

$$\omega_{\text{opt}}^2 \equiv \beta_0/\rho_p. \tag{2.112}$$

Here we see that the frequency shift $\delta \propto \omega_{opt}^4$ for weak traps. We show this trapped frequency plot in gray, figure 2.6 (a). It represents a very good approximation for small changes. The fact that both (weak trap limit and the numerical result) initially scale as the fourth power is the statement that the effective mass is decreasing, making it increasingly easier to trap. The red curve slows down relative to the gray because the effective mass reaches a minimal value and starts to increase again when it enters the delocalization zone.

Localization length and effective mass

The localization length is defined as the length at which the displacement amplitude decreases to $1/e$ of that at the center of the central pad and is given by

$$\mathscr{L} \equiv \frac{1}{\text{Im}\left[K_b\right]}. \tag{2.113}$$

To get $\mathscr{L}$ analytically in the limit $\Delta \ll 1$, we use the S expansion in the expression for K_b (equation 2.34)

$$\begin{aligned} K_b a =& \pi - i \ln\left(-S - \sqrt{S^2 - 1}\right), \\ \approx& \pi - i \ln\left(1 + S_\delta \delta - \sqrt{2 S_\delta \delta}\right), \\ \approx& \pi - i \ln\left(1 - \sqrt{2 S_\delta \delta}\right), \\ \approx& \pi + i\sqrt{2 S_\delta \delta}, \end{aligned} \tag{2.114}$$

so that,

$$\text{Im}\left[K_b\right] \approx \sqrt{2 S_\delta \delta}, \tag{2.115}$$

and

$$\frac{\mathscr{L}}{a} \approx \frac{1}{\sqrt{2S_\delta \delta}}, \tag{2.116}$$

after substituting S_δ and δ, we get

$$\mathscr{L} \approx \frac{4v_p v_t}{\left(v_t^2 - v_p^2\right)\left(\sin\left(2\omega_{lower}t_p/4\right) + 2\omega_e t_p/4\right)\sin(\omega_{lower}t_p)} \frac{1}{\Delta}, \tag{2.117}$$

or, in terms of ω_{opt},

$$\mathscr{L} \approx \frac{4v_p v_t}{\left(v_t^2 - v_p^2\right)\left(\sin\left(2\omega_{lower}t_p/4\right) + 2\omega_e t_p/4\right)\sin(\omega_{lower}t_p)} \left(\frac{\omega_{lower}}{\omega_{opt}}\right)^2. \tag{2.118}$$

This expression shows that in this limit ($\Delta \ll 1$), the localization length is much bigger than the unit cell, $\mathscr{L} \gg a$, as expected. We can also derive an analytical expression for m_{eff}, equation 2.86 from this expression. We know from above that at this limit the band edge mode has $K_b = \pi/a + (i/\mathscr{L})$, and we can use the periodicity condition to simplify m_{eff} calculation for crystals that has n unit cells equation 2.24, as we did before. To start, we find the m_{eff} for the first unit cell at the origin. Since the first pad's integral is (equation 2.88, 2.89 above),

$$m_{p,0} \approx \int_{-l_p/2}^{+l_p/2} \rho_p \cos^2(k_p x)dx = \frac{\rho_p l_p}{2} + \frac{\rho_p}{2k_p}\sin(k_p l_p), \tag{2.119}$$

we can automatically write down the integral of the n^{th} pad to the right based on Bloch periodicity, and this pad's contribution to the effective mass is then

$$m_{p,n} \approx e^{2ani(\pi + \frac{i}{\mathscr{L}})}\frac{\rho_p}{2}\left(l_p + \frac{v_p}{\omega_{lower}}\sin(\omega_{lower}t_p)\right) = e^{-2n\frac{a}{\mathscr{L}}}\frac{\rho_p}{2}\left(l_p + \frac{v_p}{\omega_{lower}}\sin(\omega_{lower}t_p)\right). \tag{2.120}$$

Next, we calculate the effective mass contribution from the tethers. We start by finding the oscillation amplitude of the first tether. The first tether oscillates approximately anti-symmetrically about its middle, and it oscillation amplitude must match at the boundary, so

$$\begin{aligned} A_t \sin(k_t l_t/2) &= \cos(k_p l_p/2) \\ A_t &\approx \cot(\omega_{lower}t_p/2), \end{aligned} \tag{2.121}$$

where A_t is the oscillation amplitude of the tether. Hence the effective mass of the n^{th} tether is

$$\begin{aligned} m_{t,n} \approx & e^{-2n\frac{a}{\mathscr{L}}} \rho_t \cot(\omega_{lower} t_p/2) \int_{-l_t/2}^{+l_t/2} \sin^2(k_t x) dx, \\ = & e^{-2n\frac{a}{\mathscr{L}}} \frac{\rho_t}{2} \cot(\omega_{lower} t_p/2) \left(l_t - \frac{v_t}{\omega_{lower}} \sin(\omega_{lower} t_p) \right). \end{aligned} \tag{2.122}$$

The total mass then reduces to a geometric series

$$\begin{aligned} m_{eff} = & m_{p,0} + 2 \sum_{n=1}^{\infty} (m_{p,n} + m_{t,n}) \\ \approx & m_{p,0} + 2 (m_{p,0} + m_{t,0}) \sum_{n=1}^{\infty} \left(e^{-2\frac{a}{\mathscr{L}}} \right)^n, \\ \approx & m_{p,0} + \frac{2m_{p,0} + 2m_{t,0}}{e^{2\frac{a}{\mathscr{L}}} - 1}, \end{aligned} \tag{2.123}$$

approximating $\frac{1}{e^{2\frac{a}{\mathscr{L}}}-1}$ as $\frac{\mathscr{L}}{2a}$, means $m_{eff} \sim (m_p + m_t)\frac{\mathscr{L}}{a} \sim \frac{1}{\Delta} \sim 1/\omega_{opt}^2$, where m_p and m_t are the effective masses of the pad and tether for the unperturbed band-edge mode

$$\begin{aligned} m_p \equiv & \frac{\rho_p l_p}{2} + \frac{\rho_p v_p}{2\omega_{lower}} \sin(\omega_{lower} t_p), \\ m_t \equiv & \rho_t \cot(\omega_{lower} t_p/2)(\frac{l_t}{2} - \frac{v_t}{2\omega_{lower}} \sin(\omega_{lower} t_p)), \end{aligned} \tag{2.124}$$

The effective mass m_{eff} in this limit is also plotted in gray in figure 2.6 (a). The localization length, and hence the effective mass are $\propto 1/\omega_{opt}^2$, which explains why the frequency shift δ is quartic in Δ.

2.1.2.3 Another figure of merit: amplitude change at the defect

We now introduce another figure of merit, which is the ratio of amplitudes of the trapped and untrapped modes, for fixed mechanical energy in the lattice. For the untrapped mode, consider the situation where the band edge mode (figure 2.6 (b,i)) of a crystal comprising N unit cells in total, with the trapping laser off, driven to some amplitude y_{off}. In this case,

the stored energy is

$$\begin{aligned} U_{tot,off} &= \sum_{n=1}^{N} \tfrac{1}{2} m_n \omega_{lower}^2 y_{off}^2 \\ &= \tfrac{1}{2} N m_{unit} \omega_{lower}^2 y_{off}^2. \end{aligned} \tag{2.125}$$

Where n is the distance from the central pad (the unit cell index). If we compare it with the same system at the same energy but with the central pad weakly trapped, this will induce the localization length $\mathscr{L}$ given above, and the amplitude profile will follow

$$y = y_{on} e^{-|n|a/\mathscr{L}}, \tag{2.126}$$

which oscillates at a new amplitude y_{on}

$$U_{tot,on} = \frac{1}{2} m_{unit} \omega_{lower}^2 \left(y_{on}^2 + 2 \sum_{n=1}^{N/2} \left(y_{on} e^{-na/\mathscr{L}} \right)^2 \right). \tag{2.127}$$

We can now estimate the ratio of the trapped pad amplitude y_{on} to that of the untrapped pad y_{off} for a given energy by equating the two

$$\begin{aligned} \frac{1}{2} N m_{unit} \omega_{lower}^2 y_{off}^2 \approx & \frac{1}{2} m_{unit} \omega_{lower}^2 \left(y_{on}^2 + 2 \sum_{n=1}^{N/2} \left(y_{on} e^{-na/\mathscr{L}} \right)^2 \right), \\ = & \frac{1}{2} m_{unit} \omega_{lower}^2 y_{on}^2 \left(1 + 2 \sum_{n=1}^{N/2} e^{-2na/\mathscr{L}} \right), \\ = & \frac{1}{2} m_{unit} \omega_{lower}^2 y_{on}^2 \left(\frac{-1 - e^{2a/\mathscr{L}} + 2e^{-Na/\mathscr{L}}}{1 - e^{2a/\mathscr{L}}} \right), \end{aligned} \tag{2.128}$$

$$\frac{y_{on}^2}{y_{off}^2} = \left(\frac{-1 - e^{2a/\mathscr{L}} + 2e^{-Na/\mathscr{L}}}{1 - e^{2a/\mathscr{L}}} \right) N. \tag{2.129}$$

So, for a 1D crystal having N unit cells in the weak-trap limit $\Delta \ll 1$, the localization length $\mathscr{L} \gg a$ and the ratio is

$$\frac{y_{on}^2}{y_{off}^2} \approx \frac{Na}{\mathscr{L}} \frac{1}{1 - e^{-Na/\mathscr{L}}}. \tag{2.130}$$

In the "small-crystal" limit $Na \ll \mathscr{L}$, then we can Taylor expand this function, and it becomes

$$\frac{y_{on}}{y_{off}} \approx 1 + \frac{1}{4}\frac{Na}{\mathscr{L}}. \tag{2.131}$$

This highlights the enhancement from light's combined influence over the many modes of a large crystal: for a given trap, the change scales with N, so larger crystals exhibit a larger response, despite the correspondingly larger mass. This perhaps unintuitive result can be understood by noting that a larger structure has more mechanical energy to draw inward to the trapping site, or, equivalently, that the density of band-edge modes scales roughly as N, and the hybridization of these modes leads to a larger trapped pad amplitude. On the other hand, if the localization length is smaller than the crystal $Na \gg \mathscr{L}$ (big crystal limit), this equation reduces to

$$\frac{y_{on}}{y_{off}} \approx \sqrt{\frac{Na}{\mathscr{L}}}. \tag{2.132}$$

In this limit, the entire structure's mechanical energy is drawn to within a radius $\sim \mathscr{L}$ of the trap, and the resulting amplitude changes can be significantly larger (scaling even more favorably in higher dimensions).

2.2 Realistic Implementation: Finite Element Model in COMSOL

We show here a relatively straightforward realization in two dimensions (2D) based on standard fabrication techniques and a "membrane-in-the-middle" optomechanical geometry [65]. First, section 2.2.1, we calculate the dispersion of a 100-nm-thick Si_3N_4 membrane patterned into an infinite 2D hexagonal lattice to find a bandgap for out-of-plane (OOP) waves. Then in section 2.2.2 we calculate the localized frequencies, mode shapes and effective mass of a finite 2D hexagonal lattice under the effect of an optical trap (positive trap), finding a very good quantitative and qualitative a agreement between our 1D approximation and this 2D calculation. In another scenario, we apply a negative trap (an anti-trap) and demonstrate that one can localize modes from the upper band. Finally, in section 2.2.3, we show the band gap size optimization results.

2.2.1 Dispersion of an infinite 2D crystal

In figure 2.7, we simulate the normal modes of a 100- nm-thick Si_3N_4 membrane patterned into the hexagonal lattice inset in 2.7. The pad diameter $d = 16$ μm, tether width $w = 1$ μm, and tether length $l = 52.5$ μm; these parameters are chosen because (i) the unit cell is relatively small (meaning a millimeter-scale structure can contain many of them), (ii) the tether width is compatible with large-area photolithography (single-pad structures have recently achieved extraordinarily low dissipation rates [2, 48]), (iii) the pads are large enough to not result in significant optical clipping losses [38, 2] when positioned within a fiber cavity [66], and (iv) this tether width of value 1 μm maximizes the gap ratio $\Delta\omega_{gap}/\omega_{mid}$. Applying Bloch-periodic boundary conditions (wave vector K_b) to the parallelogram unit cell (inset) yields the dispersion relation plotted in 2.7, following the first Brillouin zone path (1BZ, inset). The blue out-of-plane (OOP) modes exhibit a gap between 2.0 and 3.8 MHz[5]. The in-plane modes (burgundy) are significantly stiffer than the OOP modes, cutting through the gap. However, since we assume the optical restoring force is applied in the OOP direction, the in-plane modes should remain orthogonal and not play a role in OOP dynamics.

[5]Note we find that square lattices of similar dimensions behave qualitatively similarly but exhibit a smaller gap due to a combination of reduced rotational symmetry (i.e., the shift between ω_{lower} for the K and M directions is larger) and a more gradual taper between high and low wave velocities associated with the fillets (see Ref. [2] for the pad shape).

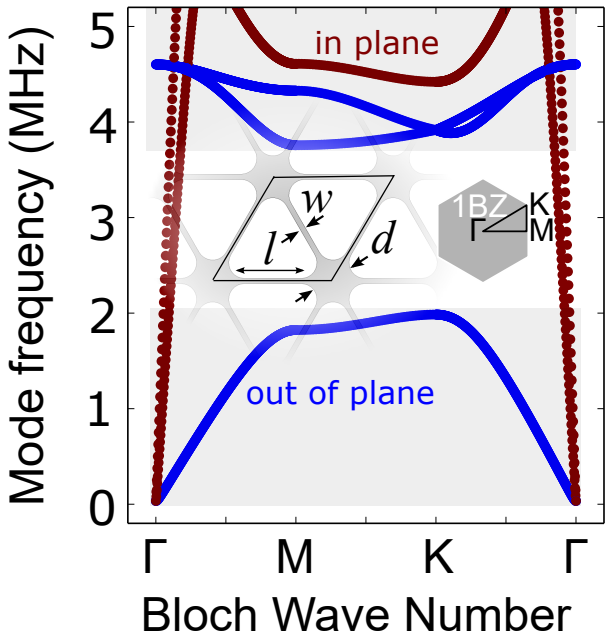

Figure 2.7: Finite-element (COMSOL) simulation of the dispersion of an infinite phononic pseudo gap membrane, fabricated from 100-nm-thick Si_3N_4 with an internal stress of 1 GPa; the unit-cell inset shows the dimensions $w = 1$ μm, $d = 16$ μm, and $l = 52.5$ μm. Red points show in-plane modes, and blue shows out-of-plane (OOP) modes. The right-hand inset shows the first Brillouin zone (1BZ, gray) and the K_b- labeling convention.

2.2.2 Localized modes

Figure 2.8 (a) shows the normal-mode frequencies for the finite crystal in Figure 2.8 (b), with a megahertz-scale optical trap having a Gaussian intensity profile with a diameter of 8 μm applied to the central pad [38, 39]. Similar to the 1D model, the nominally delocalized band-edge mode [Figure 2.8 (b), profile (i)] initially localizes [profile (ii)] and then delocalizes again [profile (iii)] as it enters the upper band. This result agrees surprisingly well with the infinite 1D model (faint red curve, 2.8 (a)) if we employ linear mass densities $\rho_p = 5.7$ pg/μm and $\rho_t = 0.81$, estimated from the density variations of a unit cell along the "K" direction [Figure 2.7, inset], and string tension $T = 230$ μN, estimated from the cross-sectional area of the tethers. The effective mass (magenta) again plummets to a value comparable to that of a single unit cell ($m_{unit}\sim$ 90 pg), with $m_{eff} \sim \rho_{SiN} t d^2 \sim$100 pg near the middle of the gap. Other modes of the structure are trapped as well [note the subtle frequency shifts in Figure 2.8 (a)], but the band-edge mode is the first to benefit from a reduced m_{eff}, allowing it to

quickly pull away from the band.

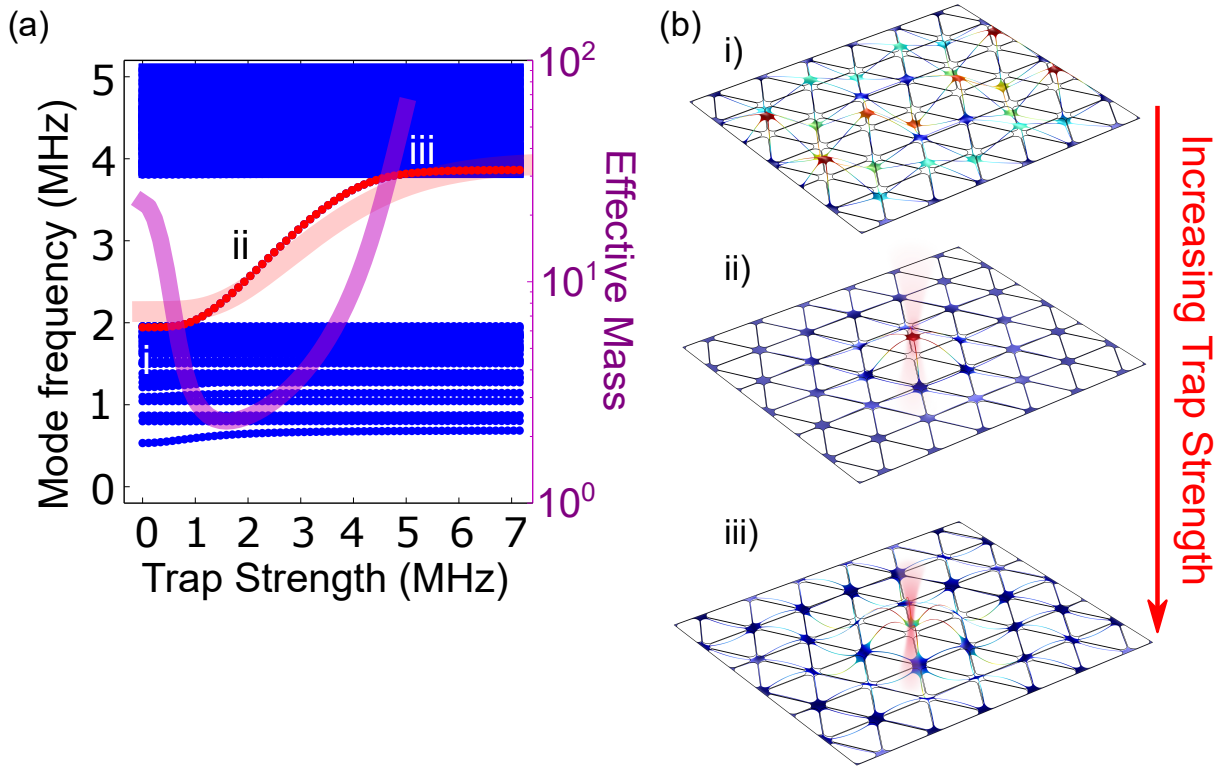

Figure 2.8: Trapping COMSOL simulation. (a) Eigenfrequencies of a finite structure with an 8- μm-diameter optical trap applied to the central pad. Trap strength is scaled by the mass of a single unit cell. The band-edge mode [red, see (i) in (b)] can be tuned through the OOP gap. The effective mass (magenta, normalized by m_{unit}) calculated from COMSOL plummets as the mode localizes. The faint red line shows the prediction of the 1D analytical model with linear mass densities and tension determined by the structure's periodicity in the K direction. (b) Mode profiles at the points indicated in (b), showing (i) the untrapped mode, (ii) localization, and (iii) delocalization.

In another scenario, as shown in Figure 2.9 (a), one can also achieve localization of the upper band-edge modes by applying a trap of negative strength (i.e., an "anti-trap"). Anti-traps can be achieved, for example, by positioning the pad at the node of an optical standing wave where, advantageously, optical loss in the nitride is minimized, thereby alleviating the problem of excessive heating. However, for our naively applied trap, the fundamental mode becomes unstable long before significant localization can occur, as evidenced by its immediate drop to zero frequency. On the other hand, the localized modes (Figure 2.9 (b)) are torsional in nature, meaning a purely torsional trap might circumvent this problem, at the expense of

increased absorption [39].

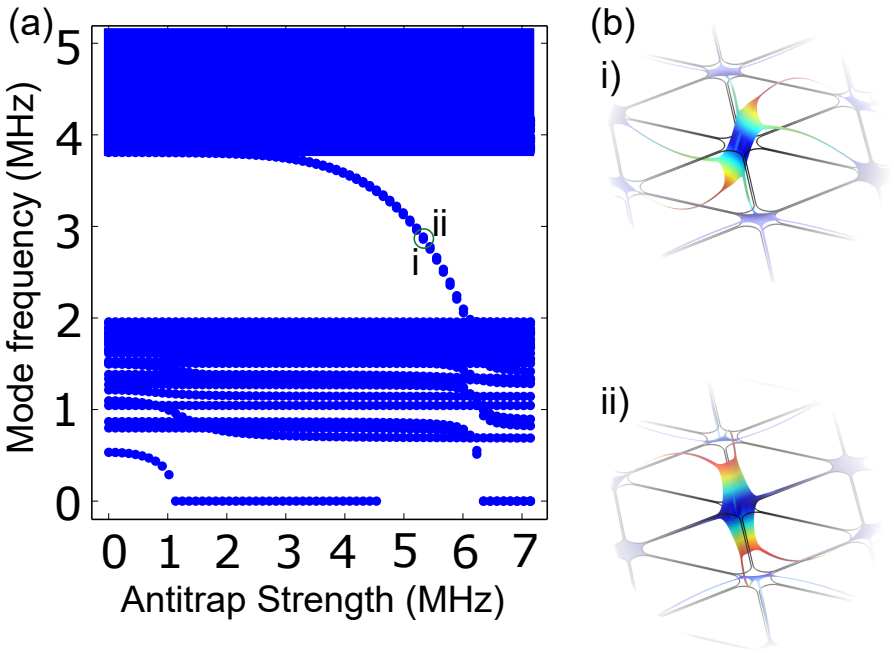

Figure 2.9: Anti-trapping COMSOL simulation. (a) localization of the upper band-edge modes by applying an anti-trap .(b) Two nearly degenerate modes localized by an optical anti-trap,(i) and (ii) shown in (a).

2.2.3 Optimization

While patterned membranes, fiber cavities, and megahertz frequency optical traps together represent a viable means of optically localizing a mechanical mode, for lower-frequency applications one may prefer to work with larger pads and free-space optics. A potential advantage of larger pads is that the increased ratio d/w (assuming $w = 1$ μm remains fixed by photolithography) results in a larger velocity contrast v_t/v_p . This in turn creates a larger gap ratio $\Delta\omega_{gap}/\omega_{mid}$ and a larger difference in amplitude between neighboring pads when localized. Figure 2.10 shows the dependence of the band-edge frequencies on tether length for the original pads with $d = 16$ μm (blue) and larger pads with $d = 128$ μm (red). The fractional gap $\Delta\omega_{gap}/\omega_{mid}$ can, indeed, be much higher for the large pads ($\Delta\omega_{gap}/\omega_{mid} = 0.9$) than for the smaller pads ($\Delta\omega_{gap}/\omega_{mid} = 0.6$), and all mechanical frequencies of course decrease with increasing size. The trade-off for larger structures is that, in order to achieve the optimal gap, the tethers must be correspondingly lengthened to the millimeter scale (although a

sub-optimal gap still exists for significantly shorter tethers).

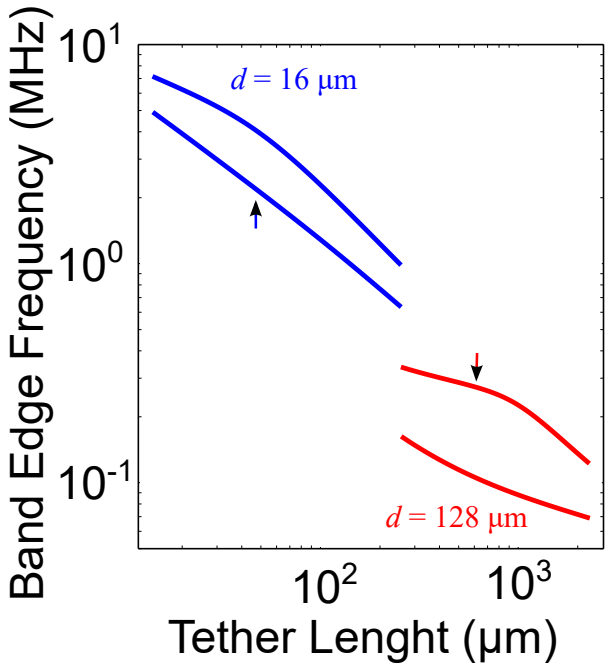

Figure 2.10: Dependence of the band-edge frequencies on the tether length for small $d = 16$ μm (blue) and large $d = 128$ μm (red) structures with $w = 1$ μm. At the optimal tether lengths (arrows), the small structure has a gap ratio $\Delta\omega_{gap}/\omega_{mid} = 0.6$, and the larger structure (higher velocity contrast) has $\Delta\omega_{gap}/\omega_{mid} = 0.9$.

2.3 Summary & conclusion

In this chapter, we explored the physics of laser localization in one dimensional ideal string under tension with periodically alternating mass density. We calculated the dispersion, identified and maximized the band gap of the out-of-plane modes. Then we applied a uniform optical spring constant density over a small region of one unit cell and numerically calculated the resulting optically driven defect modes, their mode profiles and effective mass. We found that it is possible to vary the spatial extent and the amount of participating mass in these optically defined defect modes by many orders of magnitude. We find that the localization length (and effective mass) scale as the inverse square of the trap power; even for an infinite lattice, this implies an infinitesimal trap will lead to a finite mechanical mode mass. Also, under the weak trap approximation, we analytically derive the defect frequencies and effective mass finding a very good agreement between the analytical and numerical analysis. We

derived another figure of merit for this style of optomechanical coupling which is the ratio of the trapped pad's amplitude with the trap on and off for a fixed mechanical energy stored in the mode. Counterintuitively, we found that the mechanical response to fixed trap power can increase for larger, more massive structures. Then, guided by the intuition we have developed in the one-dimensional toy model, we designed realistic two-dimensional Si_3N_4 phononic crystal membranes using FEM (COMSOL). We calculated their dispersion showing the presence of out of plane modes band gap and calculated the optically defined defect modes. We found a very good agreement between our 1D model and the 2D simulation, with the 1D model predicting band edge frequencies within ~ 20 % of those simulated, and a semi-quantitatively similar response to an applied optical trap and band gap size maximizing rules.

Furthermore, we have chosen this transverse-wave geometry because it is easy to visualize and relevant to our group's experimental capabilities, but the same physics will occur in any periodic mechanical structure, provided a local optical trap can be applied.

Since a typical optomechanics laboratory is incapable of fabricating an infinite phononic crystal, an important figure of merit is the localization length $\mathscr{L}_{1photon}$ that can be achieved with an average cavity occupancy $n_\gamma = 1$. In the calculations above figure 2.8, the trap strength is normalized to avoid any dependence on a particular trapping mechanism. To get a sense of scale for a realistic system, suppose a trap is applied to a 1D crystal having the parameters discussed in figure 2.8 by a fiber cavity [66] of length $L = 10$ μm and finesse $\mathcal{F} = 10^5$ at a wavelength $\lambda = 1064$ nm, using the (stable) "quadratic" optomechanical coupling found near avoided crossings [39, 67]. In this case, the upper limit on the per-photon spring constant $\mathbf{K_1}$ [39] produces a normalized trap strength $\sqrt{\mathbf{K_1}/m_{unit}} \sim \sqrt{16hc\mathcal{F}/L\lambda^2 m_{unit}} \sim$ 75 kHz, a localization length $\mathscr{L}_{1photon} \sim 30$ mm (570 unit cells), and an effective mass $m_{1photon,eff} \sim 50$ ng[6]. Remarkably, $\mathscr{L}_{1photon}$ is not a quantity naturally measured in parsecs, and this extremely low level of light should be capable of producing significant changes in the mode of a chip-scale mechanical element. To further quantify this statement, we estimate the ratio of the trapped pad's amplitude with the trap on (y_{on}) and off (y_{off}), for a fixed mechanical energy U_{tot} stored in the mode, derived in section 2.1.2.3, using the same

[6]Note the "linear" optical spring produces a comparable trap with some cold anti-damping in this system [68].

parameters; this effect can be quite large even for the case $n_\gamma = 1$, producing an $\sim 5\%$ amplitude change in an ~ 7 -mm-long ($N = 120$) 1D crystal. In principle, this means light at the level of a single photon, in a realistic cavity trap, can cause a measurable change in the mode of a millimeter-scale membrane.

Chapter 3

Fabrication of stoichiometric silicon nitride phononic crystal membranes

Given the promising theoretical results in chapter 2, we move now to the fabrication of two-dimensional crystals, figure 1.1 (a), similar to those simulated in chapter 2. In section 3.1, we outline the design guidelines we follow to construct the layout of the "photomask" we use in the fabrication process. Then, in section 3.2, we apply a process flow developed (by our group) for creating ultralow-noise trampolines [2]. We find that it is possible to successfully create 100-nm-thick and 300-nm-thick phononic crystals (especially those having larger pads and longer tethers), but that the yield is relatively low, with $\sim$ 15 % (for the 100 nm membranes) and $\sim$ 35 % (for the 300 nm membranes), the rest of the devices break when we attempt to release the structure. Finally, in sections 3.3, 3.4 and 3.5, we present several modified process flows that improve the yield, to as much as $\backsim$ 90 %, by protecting the crystal from turbulence and bubbles during release. Interestingly, we produce suspended phononic crystal membranes with an area as large as 20 mm^2 and up to 2750 crystal unit cells, with tethers as narrow as $\sim$ 1.5 μm. Preliminary mechanical characterization, presented in section 3.6, confirms that these devices indeed exhibit the phononic bandgap (with a ratio of gap width to band edge frequency as high as 80 %) required for laser-induced localization experiments. We finish the chapter with a summary of the main findings, section 3.7.

3.1 Device Design

In this section, we explain the design rules and considerations we have followed to construct the "photomask" layout (figure 3.1) we use in the microfabrication process.

The photomask is a glass plate coated with chrome (a metallic material that blocks UV light) in the shape of the phononic crystal structure; see figure 3.1 (a,b,c)[1]. It spans the 6" circular wafer, leaving a border of at least 0.5 cm between any device and the wafer edge. The mask is divided into 7 mm $\times$ 7 mm chips, each containing a single crystal structure at the center.

The goal of this initial work is to gain basic information about what device geometries tend to survive the process. To this end, the "front-side" mask contains devices of hexagonal (figure 3.1 (b)) and square (figure 3.1 (c)) lattices, having all combinations of the following parameters (geometrically defined for both cases in figure 3.1): window sizes (WS) of [0.35, 0.7, 1.4, 2.5, 4.5] mm, pad diameters (PD) of [16, 32, 64, 128, 256] μm, tether width (TEW) of [1, 1.5, 2, 3, 5] μm, and tether length (TEL) spans the range [26, 530] μm, using the following rule: for each combination of PD and TEW, we have chosen 5 TEL values that span +/- 30% of the optimal length (that gives the optimal gap ratio, $\Delta\omega_{gap}/\omega_{mid}$, as calculated by COMSOL for each device). We have applied this optimal TEL choice to the small pad diameter devices (only) since in the case of large pad diameter devices, the optimal tether is around a millimetre in length. For large pads, we imposed a ceiling of 500 μm on the tether length.

Small windows will ensure at least some devices survive; we know, for example that single-unit-cell systems (trampolines [2]) survive with $> 90\%$ using the simple technique of section 3.2 . The largest windows will be more than sufficient to observe interesting localization physics. The pad diameter range is chosen to have some devices compatible with both fiber and free-space cavities, and to see how large we can make the velocity contrast (see section 2.1.1.2) to maximize the gap ratio, $\Delta\omega_{gap}/\omega_{mid}$.

Note that we avoid convex or straight pad edges by adding circular fillets to result in concave pad edges [2]. We choose the fillet radius such that it gives the correct PD. For

[1]The white areas are the opaque chrome areas and the digitized (pink in the frontside mask and purple in the backside mask) areas are the clear, glass, ones.

example, in the case of hexagonal pads the radius of the fillet (RF) is given by: RF = 0.5PD. Since these nitride films are under high tensile stress ($\backsim$1 GPa) that is nonuniform through the thickness of the layer, the use of concave edges minimizes the upwards folding after release. Also, we avoid the sharp corners (locations of high stress) at the clamping regions in the frame by adding fillets (which makes them curved and smooth) to reduce the concentrated stress. In our case, the fillet radius at the frame is half that at the pad, to reduce the mass of the membrane at the clamping regions.

Figure 3.1 (d,e) also shows the backside mask. The backside has square and rectangular windows for etching through the silicon (step 15, explained below in section 3.2), and dicing lanes (we remove the nitride from these lanes so they become defect lines in the silicon; this is to assist in cleaving the wafer after the silicon etch and to get the crack to start). The width of the dicing lanes is 440 μm. Each window in the backside mask corresponds to a device in the front. The dimensions of the backside window must be chosen such that the opening at the front side, after a KOH silicon etch (see step 15 of section 3.2), matches the dimensions of the phononic crystal window. The etch profile of silicon in KOH is shown in figure 3.2 for reference.

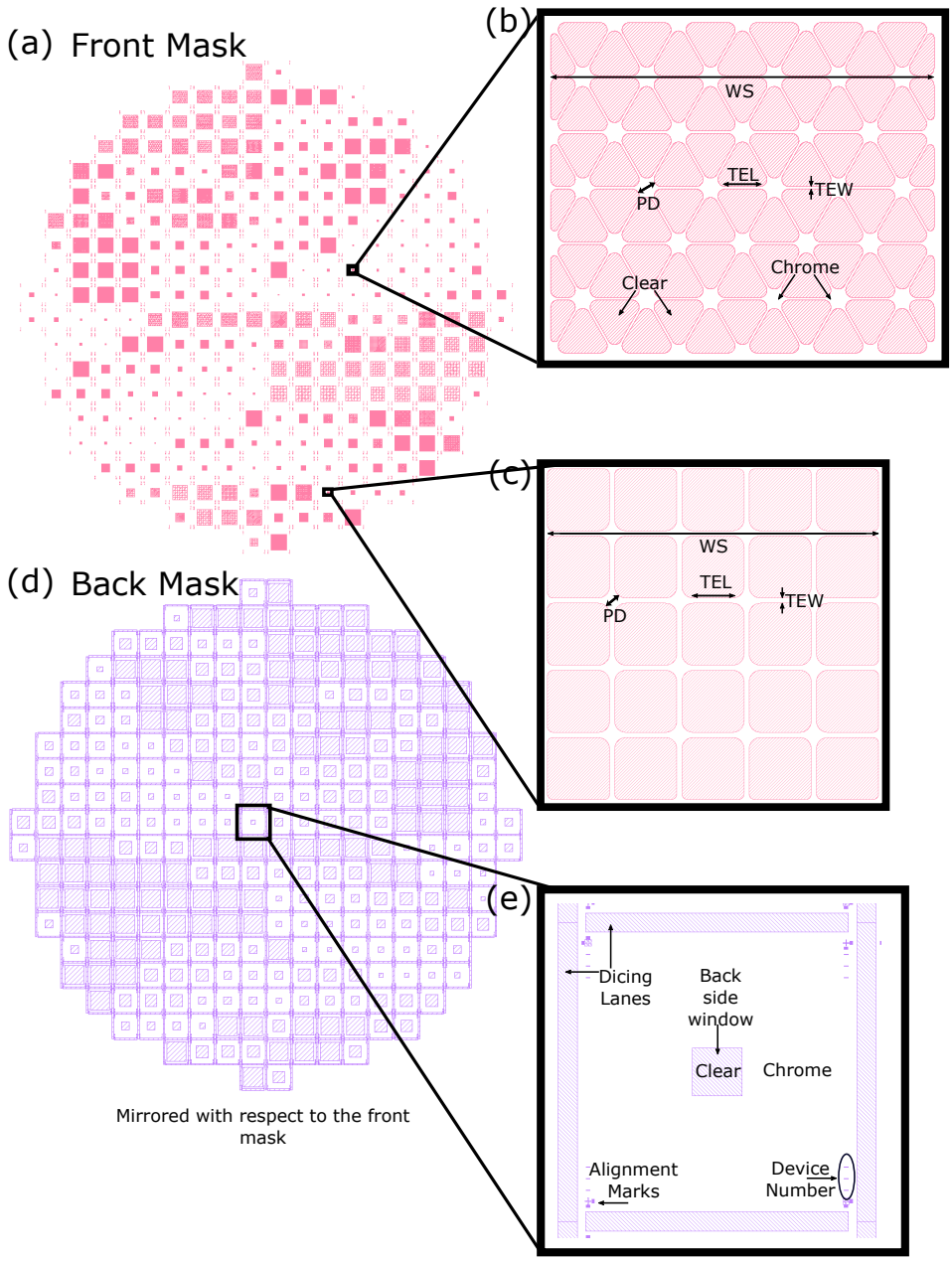

Figure 3.1: Photomasks for phononic crystal membranes. (a) Front mask layout, showing the locations and window sizes of each device (spans the 6" circular wafer, leaving a border of at least 0.5 cm between any device and the wafer edge). Devices are separated by 7 mm. (b) Example hexagonal lattice, showing the definition of tether length (TEL), tether width (TEW), pad diameter (PD) and widow size (WS). Colored regions have no chrome (clear), allowing UV light to pass through the mask. (c) Example square lattice. (d) Backside mask: each device has a corresponding etch window with a size chosen to match that of the frontside window (see figure 3.2). (e) Example device showing the etch window (central rectangle), alignment marks and device numbers (for backside alignment; a complementary set of marks and device numbers exists on each frontside device), and dicing lanes.

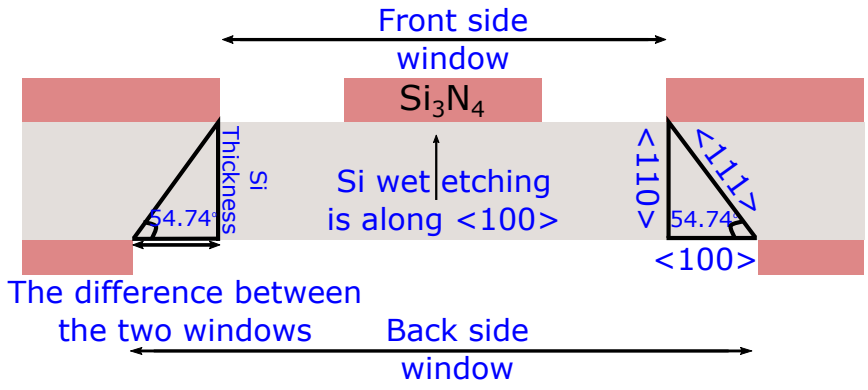

The difference between the two windows =
1.414 x Si Thickness

Figure 3.2: Cross-section of the wafer showing the KOH etch profile (stops at the 111 plane with an angle 54.74^{o}) and the relative size of the back and front windows; the back window is 1.414 x (silicon thickness) larger than the front window.

3.2 Existing process flow: unprotected front side

3.2.1 Fabrication

We first apply the process flow of reference [2]. Figure 3.3 shows a detailed view of the steps. We use a 6-inch single-crystal silicon wafer (<100> orientation) that is both polished and coated (by Addison Engineering, Inc., using low-pressure chemical vapor deposition (LPCVD)) with 100 nm silicon nitride on both sides[2]; see step one of figure 3.3. The details of the process flow are as follows (see figure 3.3):

1. Removing dust with a N_2 gun & vapor priming using YES oven: We remove dust from the wafer by blowing the wafer with the N_2 gun. Then we apply an adhesion promoter, hexamethyldisilazane (HMDS) to the wafer surface through a process called vapor priming. This is done by placing the wafer vertically inside the YES Priming Oven and running the 2 minutes priming recipe. HMDS makes a good adhesion between the photoresist (explained next in step number 2) and the wafer surface. Once inside the YES oven, moisture on the wafer is removed through heating the wafer (to 150 $^{\circ}$C)

[2]The quality of the 100 nm nitride films coated by Addison is good, however the 300 nm nitride films, (we use 300 nm nitride later as we explain in the subsequent sections), exhibit more pinholes as compared to those coated by NOVA Electronic Materials.

in low pressure below $\sim$ 10 Torr, which removes most of the water from the surface (dehydration and purging O_2 away from the chamber by flushing it with N_2 gas, then evacuating the chamber through a pump). Then, the chamber is further evacuated to below $\sim$ 1 Torr and the wafer is primed in the YES oven for two minutes such that the surface is left with a monolayer of HMDS, which bonds well with photoresist. This results in a dehydrated and hydrophobic surface (hydrophobic surface has big contact angle with water molecules or equivalently does not allow water to wet the surface). After this is done, we place the wafer vertically in a wafer container with a lid (it has a cassette that allows placing more than one wafer vertically). Then we close the lid until we prepare the next step.

2. Front side photoresist (Laurell Spin Coater): We spin-coat the frontside of the wafer with a "positive photoresist" (Shipley 1813). The photoresist is an organic viscous solution (polymer) that is sensitive to light (ultraviolet (UV) in this case). When a photoresist is exposed to UV light, the polymer reacts chemically to the light. In positive photoresist, the polymer chains break as a result of the reaction, and they become soluble in base solutions (developers, explained in step number 5). The spin coating technique is used to coat the wafer with the photoresist; it starts with dispensing the photoresist in the center of the wafer and then spinning it at high speeds to spread the photoresist and create the resist thin film using the centrifugal force. Generally speaking, the centrifugal force competes with the photoresist surface tension and viscosity; a photoresist with high surface tension tends to form balls like droplets with big contact angle. Simultaneously, the surface energy determined by the dangling bonds density on the wafer surface plays an important role in determining the wetting level of the photoresist. Ultimately, the thickness of a spun photoresist film is found to scale linearly with the viscosity and inversely as the square root of the spin speed [69, 70]. The viscosity is affected by the temperature and the solvent concentration inside the photoresist. Further, the clean room moisture and exhaust conditions influence the evaporation rate of the photoresist solvents across the wafer, which impacts the thickness uniformity. The photoresist we apply here is 1.5 μm thick; in order to obtain this thickness, we use spin speed of 4000 rpm for 30 seconds; see table 3.1. Using these

parameters, we measure around 0.1-0.2 μm thickness variation between the center and the edge of the wafer. After this is done, we transfer the wafer to a hotplate.

Step	Time (s)	Spin Speed (rpm)	Acceleration (rpm/s)
Photoresist Spreading	5	500	1305
Photoresist Spinning	30	4000	1305
Deceleration	5	0	1305

Table 3.1: Photoresist spin coating parameters (1.5 μm).

3. Soft bake: In this step we put the wafer on the hotplate at 110 ° C for one minute, with the frontside up. This removes excessive solvents from the photoresist layer and dries it. Once this is complete, we place the wafer in its container.

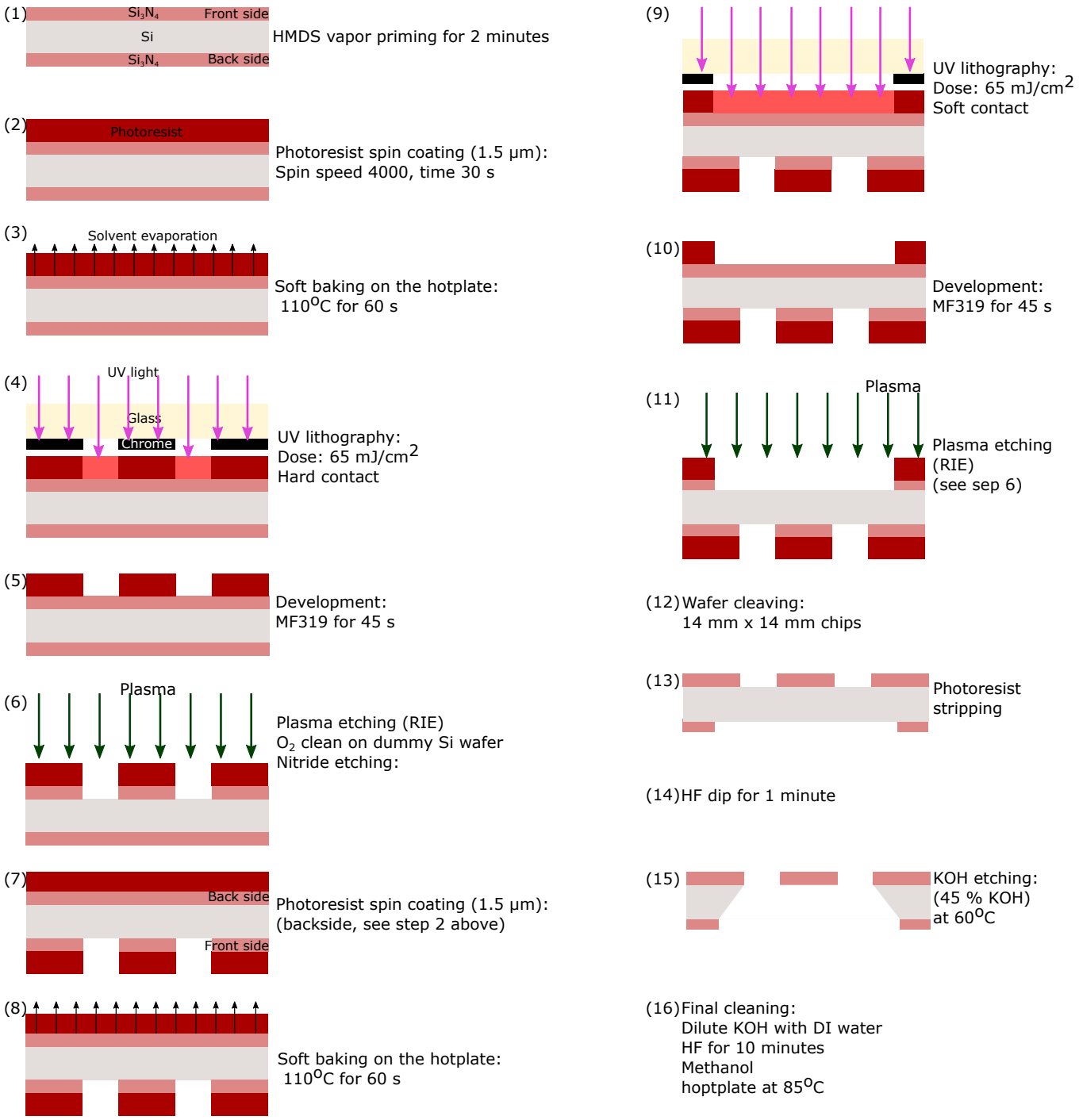

Figure 3.3: Existing process flow: unprotected front side microfabrication process flow [2] applied to 6" single crystal silicon wafer; the orientation of the crystal is <100>; the wafer is polished on both sides and coated with 100 nm LPCVD silicon nitride on both sides, (note: for steps number 6 and 11, we recommend lower RF power; this is to avoid burning the photoresist; see the revised process flow figure 3.6).

4. Expose resist to ultraviolet (UV) light (EVG 620 Contact Aligner): In this step, UV

light is used to transfer the phononic crystal pattern from the front mask (hexagons and squares grids discussed in section 3.1 and figure 3.1 (a,b,c)) to the photoresist. In general, the smallest feature that can be created with UV lithography (the resolution) is determined by the wavelength of the writing light, the separation between the photomask and the wafer, and the dose of the UV light (illumination density) measured in mJ/cm^2. The dose we use here is 65 mJ/cm^2, the reference (non-contact) separation between mask and wafer is 50 μm and the exposure is done in a hard contact mode. In our system, achieving 2 μm features is straightforward, and by properly tuning the dose of UV and development time (steps 4 and 5), we can achieve $\backsim$ 1 μm. Other details that need to be typed explicitly in the EVG recipe program are mask-holder size: 7 inch, mask thickness: 3.06 mm, substrate thickness: 0.68 mm, process: manual frontside, process mode: transparent, exposure mode: constant dose. After this is done, we place the wafer again inside its container.

5. Develop photoresist (MF 319): Once exposed, we immerse the wafer in a base solution MF 319, which serves to dissolve only the photoresist that was exposed to UV light in the previous step. In practice, we take two dishes that can accommodate the 6" wafers, and fill one of them with MF 319 developer and the other one with deionized water (DI water). We immerse the wafer, frontside up, inside MF 319. We start the timer and agitate the dish by hand to make sure a fresh developer is delivered continuously to the wafer surface for 45 seconds. When the timer is done counting, we transfer the wafer immediately to the water bath in the other dish. We agitate for a couple of seconds (50 seconds) then grab it with the wafer tweezers and wash it under the DI water tap, then blow dry it with dry nitrogen (N_2 gun). Finally, we check the newly created pattern under the optical microscope. If the patterns look clear and well resolved, then we place the wafer inside the container and move to the next step.

6. Transfer pattern to nitride with Magnetically-Enhanced Reactive Ion Etch (MERIE P5000): In this step we etch (remove) the nitride from the exposed areas using a plasma that is created and accelerated by an electromagnetic field. The etching process takes place chemically (the plasma reacts with the nitride to produce volatile byproducts),

and physically through the ion bombardment (the energetic plasma ions remove nitride atoms by collision). We use a mixture of Fluorine chemicals (CHF_3/CF_4) and argon (Ar); the fluorine is responsible for the chemical etching and the argon is mainly for the ion bombardment. The etch rate depends on many factors, such as the total pressure of the etching species and the radio frequency (RF) power. We first insert a "dummy" [3] silicon wafer in the chamber and run O_2 plasma cleaning recipe, with parameters shown in table 3.2. This is to ensure the chamber does not have other species from previous recipes executed by other users.

Parameter	Value
RF Power	200 W
Etch (cleaning)Time	3 minutes
Total Pressure	50 mTorr
Gas / Flow Rate	O2 /80 scc

Table 3.2: RIE parameters to O_2 clean the chamber

Then, we take the Si wafer out of the chamber. Second, we insert the nitride wafer (frontside up). We run the recipe in table 3.3. For these parameters, we find an etch rate of 2.2 nm / second, step 6 of figure 3.3. After this is done, we place the wafer in the container again. The photoresist is kept on the front to protect it during the next steps.

Parameter	Value
RF Power	500 W
Total Pressure	30 mTorr
Etch Time	45 s
Magnetic Field	70 Gauss
Gas / Flow Rate	CHF_3 / 30 scc
Gas / Flow Rate	CF_4 / 7 scc
Gas / Flow Rate	Ar / 70 scc

Table 3.3: RIE parameters to etch 100 nm Si_3N_4

7. Backside photoresist (Laurell Spin Coater): We place the wafer on the spinner such that backside is facing up. We apply step 2 that is detailed above with the same recipe

[3] Dummy Si wafer is usually multi crystals orientations, known as mechanical grade wafer.

to coat the backside with 1.5 μm.

8. Backside soft bake: We transfer the wafer to the hotplate such that the backside is facing up. We apply step 3, that is detailed above with the same recipe, step 8 of figure 3.3. After this is done, we place the wafer inside the container.

9. Expose backside resist to ultraviolet (UV) light (EVG 620 Contact Aligner): We apply step 4, that is detailed above to pattern rectangular and square windows on the backside. The main differences in this step are that we use another mask (the backside mask shown in figure 3.1(d, e)), we use the alignment marks shown in figure 3.1 (e) to align the backside mask to the frontside pattern that is created in steps 4, 5, and 6, and we apply a soft contact mode to reduce the pressing force applied to the frontside patterns. After this is completed, we place the wafer inside the container.

10. Develop backside photoresist (MF 319): We apply step 5 to remove the photoresist from the rectangular and the square windows on the backside. We place the wafer in the developing dish such that the backside is facing up. Note that since there is no fine size feature in the backside, we can develop for a bit longer than 45 seconds. After this is done, we place the wafer inside the container.

11. Transfer pattern to backside nitride with Magnetically-Enhanced Reactive Ion Etch (MERIE P5000): We apply step 6, that is detailed above to etch the nitrite from the rectangular and the square windows. We insert the wafer such that the backside is facing up.

12. Cleave wafer using a diamond scribe: We cleave (cut) the wafer by hand into square pieces (chips) that are 14 mm x 14 mm. We place the wafer on a clean room wipe, such that backside is facing up. Then, using the diamond scribe (a sharp diamond pen) we add a little vertical scratch to the edge of the wafer near the central dicing lane (from the flat region side of the wafer). This little scratch is sufficient to initiate the cut through the whole wafer (to two halves) using a wafer cleaving plier. Then using the same method, we cut each half to two quarters and each quarter to 15 mm x 15 mm chips (dicing lanes are shown in (e), figure 3.1).

13. Strip photoresist using organic solvents: We strip (remove) the photoresist from the two sides of the chips using acetone (an organic solvent). We immerse the chips inside an acetone beaker and place the beaker inside a warm water bath at 40 $^\circ$C for 30 - 60 minutes (we agitate from time to time), then we transfer the chips (while spraying them with isopropanol to prevent the acetone from drying and leaving a residue) to an isopropanol (IPA, another organic solvent) beaker and immerse them to remove acetone residues for 5 minutes. Finally, we transfer the chips to a DI water beaker for 5 minutes and dry the chips one by one with the N_2 gun.

14. Hydrofluoric Acid (HF) dip: We immerse the chips inside the HF that has (10 : 1 DI Water : HF 49%) concentration to remove the native oxide from the silicon windows. In practice, we install the chips in a Polytetrafluoroethylene (PTFE) holder and dip the whole assembly vertically into HF for 1 minute. Next, we transfer the holder with chips from HF to a DI water beaker for a couple of seconds then we transfer them to a second DI water beaker to make sure we removed all HF from the chips and the holder. PTFE is a highly resistive material to all corrosive acids and basis even at high temperatures (up to 300 $^\circ$C). This holder is especially designed [2] to keep the chips vertically still during the subsequent manipulation, especially when the phononic crystal membranes are released. We keep the holder with the chips inside the water beaker until we prepare the next step.

15. Etch silicon using Potassium Hydroxide (KOH): The KOH is a base solution used to etch silicon through a chemical reaction. The etch rate depends on the concentration of the KOH, the crystalline orientation of the silicon and the temperature of the solution. It is anisotropic etching that results in an undercutting (see figure 3.4 where the undercut is shown in (a) and (b)). Since the chips are already inside the water beaker from the previous step, we transfer them with the holder to a beaker of 45% KOH (we make sure all chips are well immersed), then we place the chips with the KOH beaker on the hotplate, and heat the solution to $\backsim$ 60 $^\circ$C. The etch rate of the <100> crystal plane at 60 $^\circ$C is $\backsim$ 18 μm / hour, so after around 19 hours the phononic crystal membranes are released.

16. Final cleaning: When the membranes are fully released in KOH, we dilute the KOH with DI water and a syringe, until the solution becomes clear and the KOH concentration is less than 1%. We transfer the holder with the chips from the water to HF for 10 minutes. The HF etches the nitride at an etch rate of $\backsim$ 1 nm / minute and hence it removes the outermost layers from the surface of the released membranes, resulting in clean devices. Then we transfer the holder with the chips to two DI water beakers successively to remove all remaining HF as we do in step 14. After that we transfer the holder and the chips to methanol (an organic solvent) beaker. Methanol reduces the surface tension the membranes experience when they dry and evaporates quickly without leaving a residue. Finally, we transfer the chips one by one using the tweezers to the hotplate such that the frontside is facing up at 85 $^\circ$ C to dry. The drying process happens in a "flash", leaving a very clean surface. Critical point drying is also a viable solution, but in practice this produced significantly dirtier devices in our system.

When fabricating individual trampoline structures [2], the yield can exceed 90%. However, with these more complicated structures, the yield is below 15%. For example, two devices out of 24 have survived in the first trial, and no devices have survived in the second one. Figure 3.4 shows the two survived devices and two examples of the broken ones. We observe that devices with relatively small number of pads, big pads radii and long tethers survive more than those having many pads and short tethers, consistent with observed trends for trampolines [2]. We suspect that this low yield is a result of the penetration of the H_2 gas bubbles (generated inside KOH during the silicon wet etching) through the frontside of the structure. In figure 3.5, we show schematically our vision on how they might be breaking inside KOH solution. Presumably, the pressure exerted by the expanding bubbles and the surface tension provides sufficient force to crack these delicate structures.

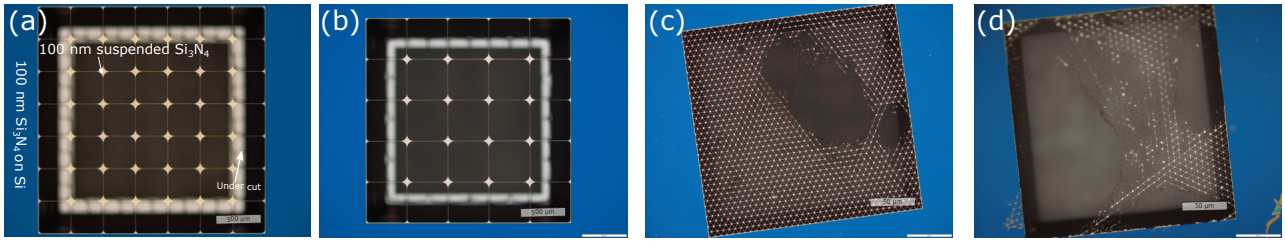

Figure 3.4: Suspended Si_3N_4 phononic crystal membranes, 100 nm thick. We produced these devices by applying the existing process (unprotected front side) explained in figure 3.3 [2]. (a) and (b) show the first two survived devices with the following device parameters, respectively, (64 µm pad diameter, 1.5 µm tether width, 200 µm tether length, 2750 µm front window size, and 36 pads) and (64 µm pad diameter, 1.5 µm tether width, 350 µm tether length, 2300 µm front window size, and 16 pads). (c) and (d) show two examples of broken devices with the following device parameters respectively, (16 µm pad diameter, 1.5 µm tether width, 50 µm tether length, 2750 µm front window size, and 1404 pads) and (16 µm pad diameter, 1 µm tether width, 50 µm tether length, 2750 µm front window size, and 1258 pads).

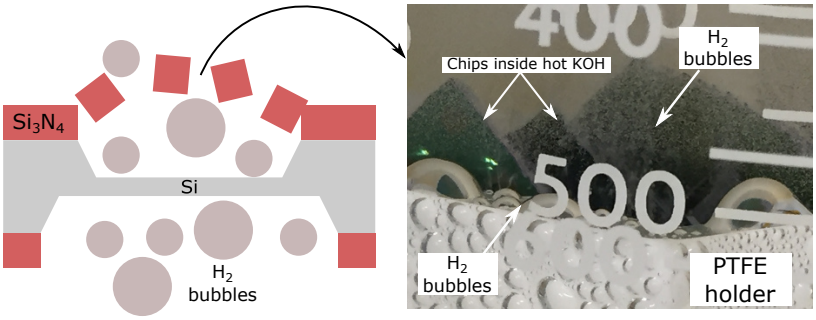

Figure 3.5: Hydrogen (H_2) bubbles in KOH solution. (right) A schematic view of a patterned device that is placed inside hot KOH; it shows how bubbles penetration from the front can break the structure and (left) a picture of the chips placed in the PTFE holder inside hot KOH solution; it shows the real H_2 bubbles everywhere.

However, to improve the yield, we have attempted the same process flow but with 300 nm LPCVD (thick) nitride wafers that is both polished and coated (by NOVA Electronic Materials) on the two sides. The schematic details are in figure 3.6. All photolithography and etching parameters have been re-optimized for this 300 nm nitride thickness. Besides that we have implemented some extra steps:

- We use 2.0 µm photoresist thick and hence we increase the UV light dose to 80 mJ / cm^2 and the development time to 55 s; see table 3.4 for the recipe details.

Step	Time (s)	Spin Speed (rpm)	Acceleration (rpm/s)
Photoresist Spreading	5	500	1305
Photoresist Spinning	30	2000	1305
Deceleration	5	0	1305

Table 3.4: Photoresist spin coating parameters (2.0 μm).

- We use lower RF power (100 W instead of 500 W) during the nitride etch. We think low RF power is a better choice as compared to the 500 W we have used in the previous process flow. This reduces the energy of the impinging ions, the temperature of the resist, and its tendency to burn, making it easier to remove. Table 3.5 shows the RIE parameters in details, which result in an etch rate of 0.25 nm / second.

- We do this slowly (20 minutes) etching in a piecewise fashion: we divide the etch time into three segments (10 minutes, 5 minutes, 5 minutes), with a $\sim$ 2 minutes rest in between, allowing the wafer to cool down, thereby further reducing the probability of burning the photoresist. See table 3.5.

Parameter	Value
RF Power	100 W
Total Pressure	30 mTorr
Etch Time	20 minutes = (10 + 5 + 5 minutes)
Magnetic Field	70 Gauss
Gas / Flow Rate	CHF_3 / 30 scc
Gas / Flow Rate	CH_4 / 7 scc
Gas / Flow Rate	Ar / 70 scc

Table 3.5: RIE parameters to etch 100 nm Si_3N_4.

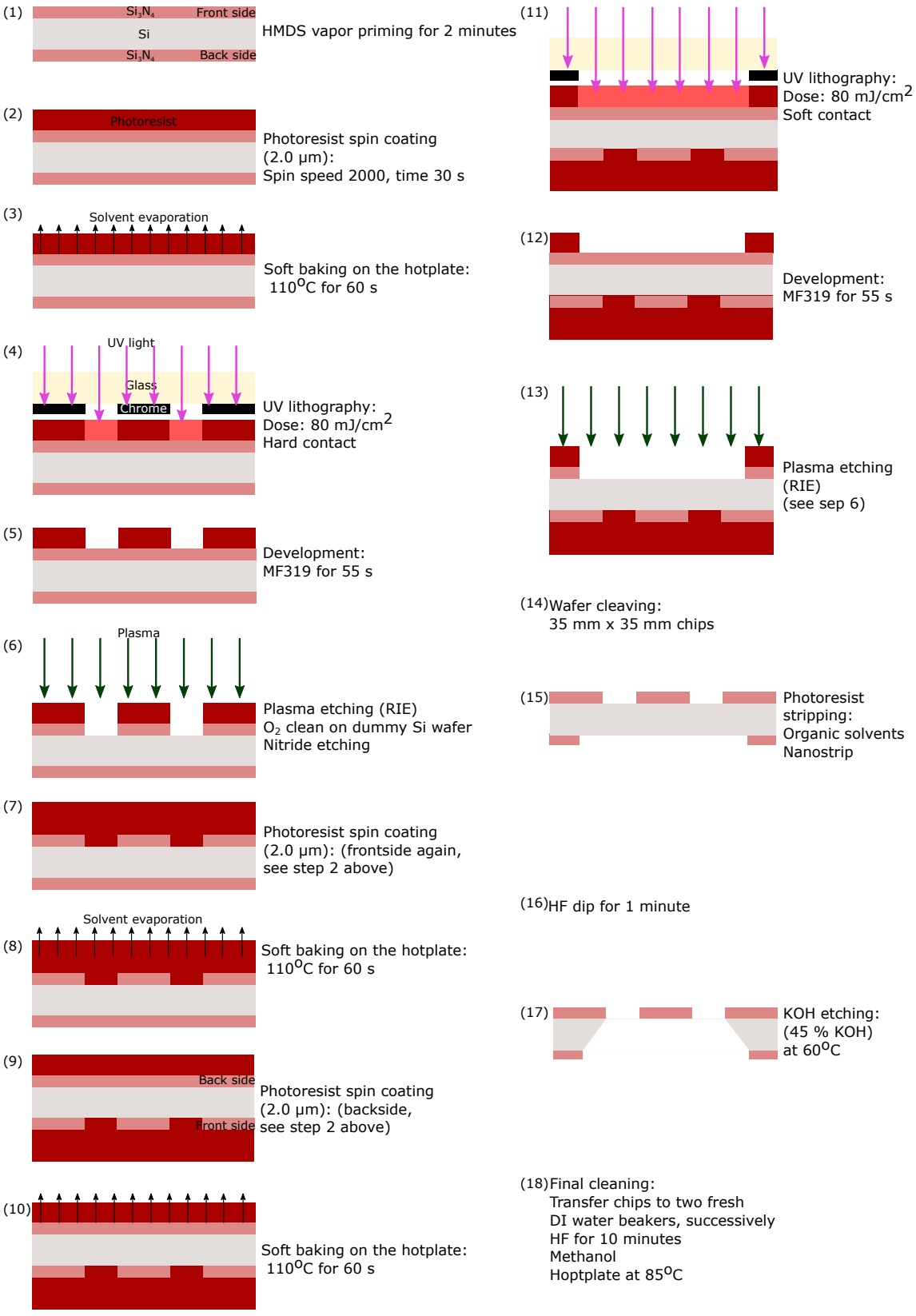

Figure 3.6: Slightly modified microfabrication process flow applied to 6" single crystal silicon wafer; the orientation of the crystal is <100>; the wafer is polished from the two sides and coated with 300 nm LPCVD silicon nitride on both sides.

- We added one more step to the process, which is coating the front side with a 2 μm photoresist after the front RIE step to enhance the protection of the patterned devices in the front side as we complete the process of the backside patterning. We use the recipe in table 3.4, step 7 of figure 3.6.

- We started to use a clean dummy silicon wafer on the hotplate we use to soft bake the photoresist in steps 3, 8, and 10 of figure 3.6. We make sure the silicon wafer has been heated for enough time to reach the required temperature, 110 $^\circ$ C. We place the nitride wafers on top of this clean one to make sure our wafer does not grab dirt or residues from the hotplate.

- We started to cleave the chips into 35 mm x 35 mm squares instead of 14 mm x 14 mm. We found that this increases the yield of the devices located at the center of the chip as compared to the devices located near the chip edges. We suspect that this might be due to the fact that when we cleave the wafer into small chips by hand, we might be introducing fractures into this high stress thin film, this might affect the survival rate of the devices that are close to the chip edges. Furthermore, devices that are close to the chip edges have higher probabilities of being damaged by the tweezers; see step 14 of figure 3.6.

- We use "Nanostrip" sometimes, (this is a chemical solution that is composed of sulfuric acid (H_2SO_4, 90%), peroxymonsulfuric acid (H_2SO_5, 5%), hydrogen peroxide($< 10\%$) and water (H2O, 5%)), to strip the leftover photoresist residues after organic solvents. In practice, we immerse chips with the holder in Nanostrip and heat it on a hotplate until it reaches 90°C. We leave them for 30 minutes at 90°C. Then we transfer the assembly to two beakers of fresh DI water successively to remove all residues. We repeat this step until there is no evidence of remaining resist when viewed under an optical microscope.

- As we buy these wafers from different vendors, we have no control over the nitride film quality, for example the pinholes density. As pointed out earlier, we found fewer pinholes in the wafers coated by NOVA Electronic Materials as compared to those

coated by Addison Engineering, Inc. We also started to handle the chips more carefully, so as to minimize the introduction of additional fractures in the nitride: we eliminated or minimized sonication whenever possible, and avoided letting the wafers tap hard surfaces such as the sides of dishes. We found some (somewhat unconvincing) evidence that sonication in particular increased pinhole density in thicker high-stress nitride.

- After KOH etching, when the chips are released, we stopped diluting the KOH and started to wash samples by the direct transfer from KOH solution to DI water. Practically, we transfer the chips with the holder to a beaker of DI water and immerse them completely for a couple of seconds ($\backsim$1 minute), then we transfer the assembly to another beaker with fresh DI water (second time) and leave them there until we prepare the HF beaker; see step 18, figure 3.6.

- Otherwise, the remaining steps, HF cleaning and methanol-hotplate drying have been kept the same as in [2] and as mentioned earlier in this section.

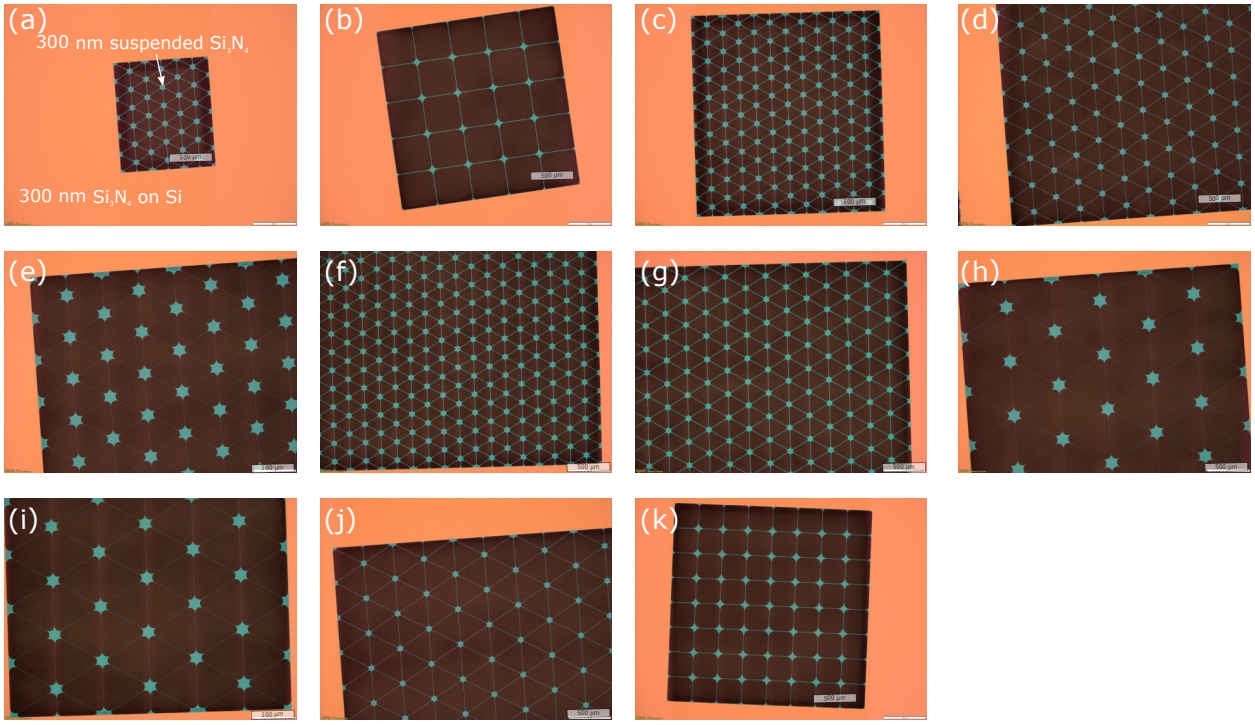

Figure 3.7: Suspended Si_3N_4 phononic crystal membranes, 300 nm thick. We produced these devices by applying the slightly modified microfabrication process flow explained in figure 3.6. (a) has the following parameters: 64 µm pad diameter, 5 µm tether width, 144 µm tether length, 1400 µm front window size, and 30 pads. Note the difference in Si_3N_4 color between the 300 nm suspended membrane and the 300 nm thin film on silicon. (b) has the following parameters: 64 µm pad diameter, 5 µm tether width, 300 µm tether length, 2150 µm front window size, and 16 pads. (c) has the following parameters: 64 µm pad diameter, tether width 5 µm, 144 µm tether length, 2400 µm front window size, and 121 pads. (d) has the following parameters: 64 µm pad diameter, 3 µm tether width, 250 µm tether length, 4500 µm front window size, and 196 pads. (e) has the following parameters: 128 µm pad diameter, 1 µm tether width, 350 µm tether length, 4500 µm front window size, and 81 pads. (f) has the following parameters: 64 µm pad diameter, 5 µm tether width, 125 µm tether length, 4400 µm front window size, and 400 pads. (g) has the following parameters: 64 µm pad diameter, 5 µm tether width, 185 µm tether length, 4500 µm front window size, and 256 pads. (h) has the following parameters: 128 µm pad diameter, 1µm tether width, 500 µm tether length, 3800 µm front window size, and 36 pads. (i) has the following parameters: 128 µm pad diameter, 1.5 µm tether width, 450 µm tether length, 3880 µm front window size, and 36 pads. (j) has the following parameters: 64 µm pad diameter, 3 µm tether width, 350 µm tether length, 4200 µm front window size, and 100 pads. (k) has the following parameters: 64 µm pad diameter, 3 µm tether width, 170 µm tether length, 2400 µm front window size, and 49 pads.

3.2.2 Device yield and discussion

As a consequence of using thicker nitride, re-coating the patterned front side, careful handling and bigger size chips, the yield has increased to around 30%, and devices with up to 400 and 256 (relatively big pads) made it all the way to the end. Figure 3.7 (a)-(k) shows images of some of the surviving devices and figure 3.8 shows a three dimensional space of survived and broken devices of both geometries (hexagons and squares) as a function of PD (pad diameter), TEL (tether length) and total number of pads.

Ultimately, this fabrication technique can be used to produce clean, large, and delicate devices, but we now wish to maximize the yield for devices of all dimensions. And as mentioned earlier, we suspect the main reason why they break is the aggressive penetration of the H_2 bubbles inside the hot KOH solution, so we now apply a method that protects the frontside of the devices inside KOH etching and only allows etching to take place from the backside.

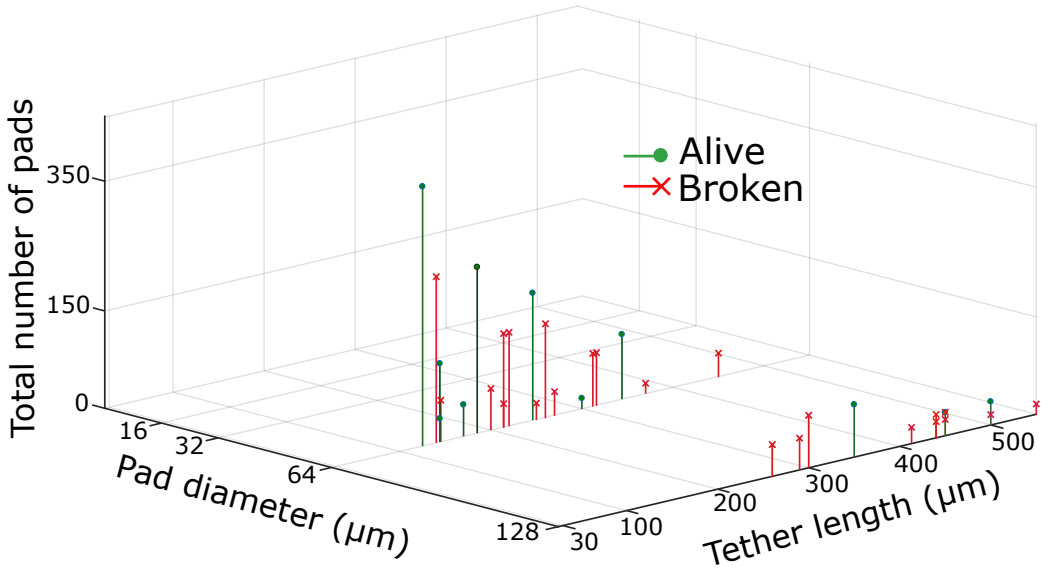

Figure 3.8: The yield of the modified microfabrication process flow shown in figure 3.6. Three-dimensional space map that shows the survived (circles) and broken (crosses) devices as a function of the PD, TEL and the total number of pads; the map has considered hexagons and squares together.

3.3 Front-side protection with partially etched silicon nitride

Our first method of protecting the front side from KOH is to not etch the 300 nm Si_3N_4 from the nitride openings (colored areas in the mask, shown in figure 3.1) of the frontside completely; instead, we leave a thinner layer of approximately 200 nm. This layer serves as a mask for the frontside; it prevents H_2 bubbles from penetrating through the frontside during KOH etching. We then perform the final release in BHF (Buffered Hydrofluoric Acid)[4]. BHF etches Si_3N_4 isotropically (note that Si_3N_4 is an amorphous material; it does not have long range order) at an etch rate (ER) of ~0.62 nm / minute (room temperature). Most importantly, the chemical reaction of BHF with nitride does not produce gases, which means that the phononic crystal structures are released in a bubbling free solution. Note that no devices survived this process (the devices all break during the final HF release), but we include the details here in hopes that someone sees a pathway forward with this simple technique.

The first steps are to calibrate RIE parameters, find the etch rate, and find what limits the uniformity we can achieve. Following the steps from 1 to 5 of figure 3.3, we start with a 6" single-crystal silicon wafer (<100> orientation, polished from one side and coated by Addison Engineering, Inc.with 100 nm LPCVD silicon nitride on both sides) and use the backside mask (shown in figure 3.1 (d)) to create a set of unpatterned rectangular and square windows, with a wide range of dimensions on the polished side; see figure 3.9(a). We then cleave the wafer into different chips sizes to test RIE parameters. We use the small chips, for example, to calibrate the RF power and the etching time. Then we measure the thickness of the remaining nitride using a spectroscopic ellipsometer to calculate the etch rate[5], [6]. The local nitride thickness is written (in nm) explicitly at each location on the chip as shown

[4]HF (10.0 : 1.0 DI water : HF 49%) can be used as well, but at that time our clean room has stopped supplying it

[5]We have etched many small chips for this purpose and constructed a kind of a chart for the nitride thickness on silicon. We found that it is consistent with the charts in literature [71]

[6]The spectroscopic ellipsometer is a thin film characterization tool. It is based on measuring the reflectance (or transmittance) and the polarization change of a laser beam, that is directed at a non-normal incidence, after it is reflected from a surface of a thin film or transmitted through it. It measures, for example, the refractive index, the roughness and the thickness of thin films.

in figure 3.9. We also test the etching uniformity by measuring the etch rate at different locations within the single window and across the chip; see (b, c), figure 3.9. We find an etch rate of $\sim$ 0.23 nm / second, at the chip center, when applying RF power of 100 W, total pressure of 30 mTorr, (CHF_3 (30 sccm), CF_4 (7 sccm), Ar (70 sccm)), and etch times between 121 and 320 seconds; for the recipes details; see figure 3.9 (a)-(c).

(a) Etch test on Chips

(1) 6" double sided polished silicon wafer
Si thickness: 670 µm, Orientation <100>
Coated with 100 nm LPCVD SiN on both sides
Following the process flow in Fig 3.3 (until step 5), we create this test wafer, using the backside mask shown in (d) of figure 3.1

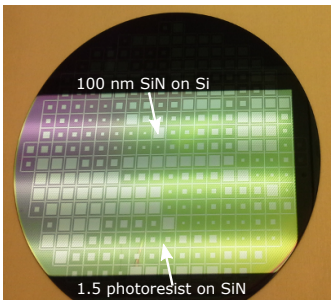

(2) Cleave the wafer to small chips
Fix the chip in the center of a clean carrier silicon (dummy) wafer, using wax

(3) Insert another dummy Si wafer in the RIE machine
Run the O_2 clean recipe (5 minutes)
Insert the Si carrier wafer with the chip
Run the nitride etching recipe below

Parameters	Value
RF Power	100W
Total Pressure	30 mTorr
Etch time	Shown below each chip
Magnatic Field	70 Gauss
Gas/Flow rate	CHF_3/30 sccm
Gas/Flow rate	CF_4/7 sccm
Gas/Flow rate	Ar/70 sccm

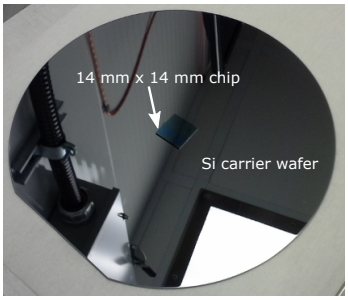

(b) Small Chips

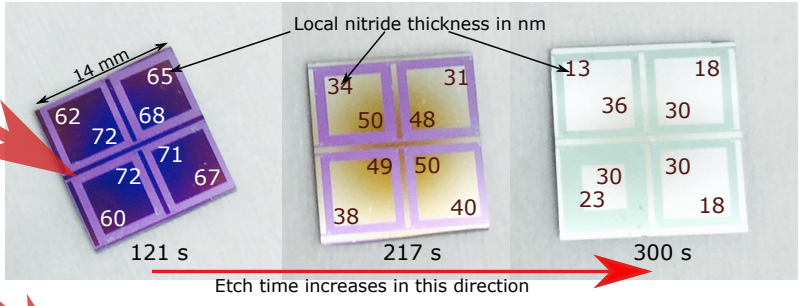

(c) Larger Chips

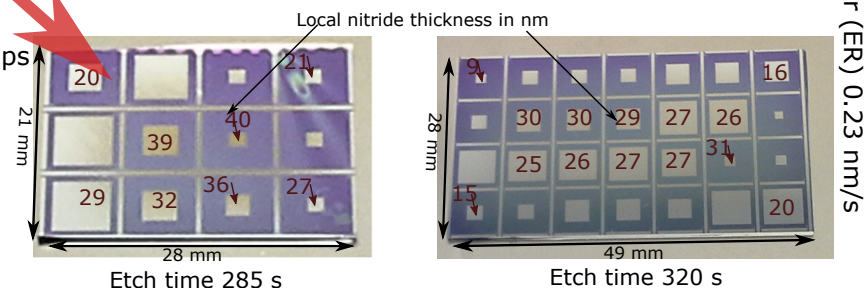

Figure 3.9: Etch rate and uniformity of small chips. (a) A brief description of the process steps we use to make the etch test on small chips: (1) A test wafer shows the square and rectangular Si_3N_4 windows after development; we produce it using the process flow in figure 3.3, steps 1 to 5. (2) We cleave the wafer into small chips using the same side (we created) that has the dicing lanes. (3) We mount the chip on a dummy Si wafer and run the recipes (O_2 clean, table 3.2, nitride etch, shown above in the figure). (b)/(c) Small chips / big chips showing the thickness of the nitride at different locations (original nitride thickness is 100 nm) and the etch time used for each chip. Note that the etching uniformity improves in bigger chips. We measure the thickness using the spectroscopic Ellipsometer.

As shown in figure 3.9, when we etch small chips, the etch rate increases radially, from the center of the chip towards the edges; note the small nitride thickness close to the chip edges as compared to the center. More notably, we find that the etching uniformity of the central region of the chip improves as the chip area increases. For example, one can compare the nitride thickness in the windows in (c) versus (b), figure 3.9; while there is at least 10 nm change in the thickness in the single window in the case of 14 mm x 14 mm chips, (a), we do not see this thickness change within the single window in the chips shown in (c). Also, the big chip (49 mm wide) in (c) has almost 10 windows that have very close nitride thickness as compared to only two windows with close thickness in the smaller chip (28 mm wide).

Therefore, this result has motivated us to test the etching uniformity across the full 6" wafer. To do this, we follow the steps from 1 to 5 of figure 3.6. We start with a 6" single-crystal silicon wafer (<100> orientation, polished from one side and coated by NOVA Electronic Materials with 300 nm LPCVD silicon nitride on both sides) and use the frontside mask (shown in figure 3.1 (a)) to create the phononic crystal structures on the polished side. Then we apply the RIE recipes shown in (a) and (b) of figure 3.10. The recipe in (a) results in a nonuniform etching, i.e., $\sim 40\%$ variation in etch rate across the wafer. However, the recipe in (b) results in a uniform etching, i.e., $\sim 20\%$ variation in etch rate across the wafer. This could in principle be improved further, but it is already sufficient for our purposes; ignoring outliers, there will be many devices having an etch rate within +/- 5% of our targeted etch rate. Note also that when we have the phononic crystal structures, which is partially etched on the the frontside, we can only measure the nitride thickness in the devices openings that are bigger than the reflectometer laser spot size. For other devices, where the openings are smaller than the laser spot size, we can estimate the nitride thickness from the color we see under the optical microscope by comparing it to the color chart [71] we have produced before when we did the RIE calibration on many small chips (provided that we keep the optical microscope at the same settings every time we compare the nitride thickness with the reference chart)[7]. Note that, the recipes in (a) and (b) employ the same RIE parameters such as, the RF power (50 W) and the pressure (30 mTorr); they only vary in the etching time.

[7] We will use this chart thickness trick later to estimate the nitride thickness and hence the HF time needed to release the structure.

When the etching time in (figure 3.10 (a)) drops by ~ 70 %, keeping all other parameters the same, the etch rate decreases (as expected) and more surprisingly the uniformity improves; see (figure 3.10 (b)). This suggests that RIE in general is a quite complicated process and that we are fortunate to find these parameters in one of the RIE runs we have attempted.

(a)

Parameters	Value
RF Power	50W
Total Pressure	30 mTorr
Etch time	333 seconds
Magnatic Field	70 Gauss
Gas/Flow rate	CHF_3/30 sccm
Gas/Flow rate	CF_4/7 sccm
Gas/Flow rate	Ar/70 sccm

(b)

Parameters	Value
RF Power	50W
Total Pressure	30 mTorr
Etch time	93 seconds
Magnatic Field	70 Gauss
Gas/Flow rate	CHF_3/30 sccm
Gas/Flow rate	CF_4/7 sccm
Gas/Flow rate	Ar/70 sccm

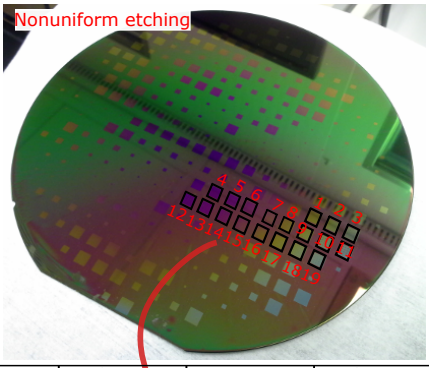

Location	Nitride thickness (nm)	Location	Nitride thickness (nm)
1	166.8	11	141.45
2	152.38	12	201
3	139.62	13	197.25
4	205	14	192.85
5	201	15	186.05
6	197.8	16	176.4
7	191.52	17	164.22
8	184	18	148.89
9	172.3	19	131.34
10	158.59		

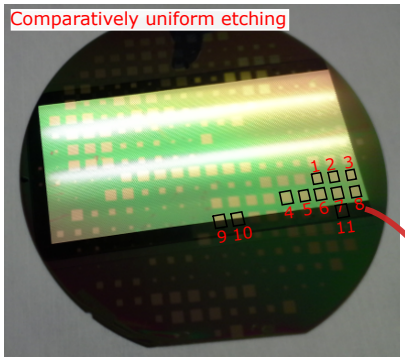

Location	Nitride thickness (nm)	Location	Nitride thickness (nm)
1	250	7	245.46
2	248.5	8	244.38
3	247.58	9	258.7
4	253	10	257.21
5	251	11	241.8
6	248.29		

Figure 3.10: Etch rate and uniformity of full wafers. We use 6" single sided polished silicon wafers, Si thickness: 670 μm, orientation <100>, coated with 300 nm LPCVD SiN on both sides. By following the process flow in figure 3.6 (until step 5), we create these wafers using the frontside mask, shown in figure 3.1 (a). Then, we run the O_2 clean recipe, table 3.2. Next, we run the nitride etching recipes (a, b), shown above in the figure, for each wafer, respectively. The etching parameters resulted in (a) a nonuniform / (b) a comparatively uniform etching across the wafers. The tables show the nitride thickness in the nitride openings of different devices (highlighted with black squares). The dimensions of the nitride openings of the other devices are smaller than the spot size of the laser beam used in the reflectometer (the reflectometer is another thin film characterization tool. It is based on measuring the reflectance of the laser light, that is directed at a normal incidence, after it is reflected from the surface of a thin film. It can also measure the optical properties such as the refractive index and the thickness of thin films), so we could not measure them, but the colors provide an approximate estimate of thickness, implying that the selected measurement points are representative of the variations across the wafer.

At this point, we can carry on the process flow of figure 3.11 . We proceed from step (7)

all the way to step (15) with the same protocol we discussed formerly in detail in 3.2 . For example, we show in figure 3.12 (a), a chip after cleaving and photoresist stripping (before BHF dip). The zoom in shows an optical microscope image of one of the devices under maximum illumination; the device parameters are pad diameter: 64 μm, tether width: 3 μm, tether length: 150 μm, front window size: 2400 μm, and total number of pads: 330. The structured nitride, in the shape of the phononic crystal, on silicon (dark pink color, which is the same as the chip) is 300 nm thick, the nitride openings on silicon (yellow color) are $\sim$ 250 nm. We then dip the chip (already installed in the PTFE holder) in BHF, step (16) figure 3.11, to remove the native oxide for 5 minutes. As a result, the structured nitride (the nitride on chip) thickness and the thickness of the nitride in the device opening are reduced by $\sim$ 3 nm. If the etch rate of nitride in BHF is 0.62 nm / minute, then we need $\sim$ 3.3 hours (3 hours and 18 minutes) of BHF etching (to remove the nitride in the openings) and will end up with phononic crystal membranes that are $\sim$ 50 nm thick. We move now to step 17, figure 3.11.

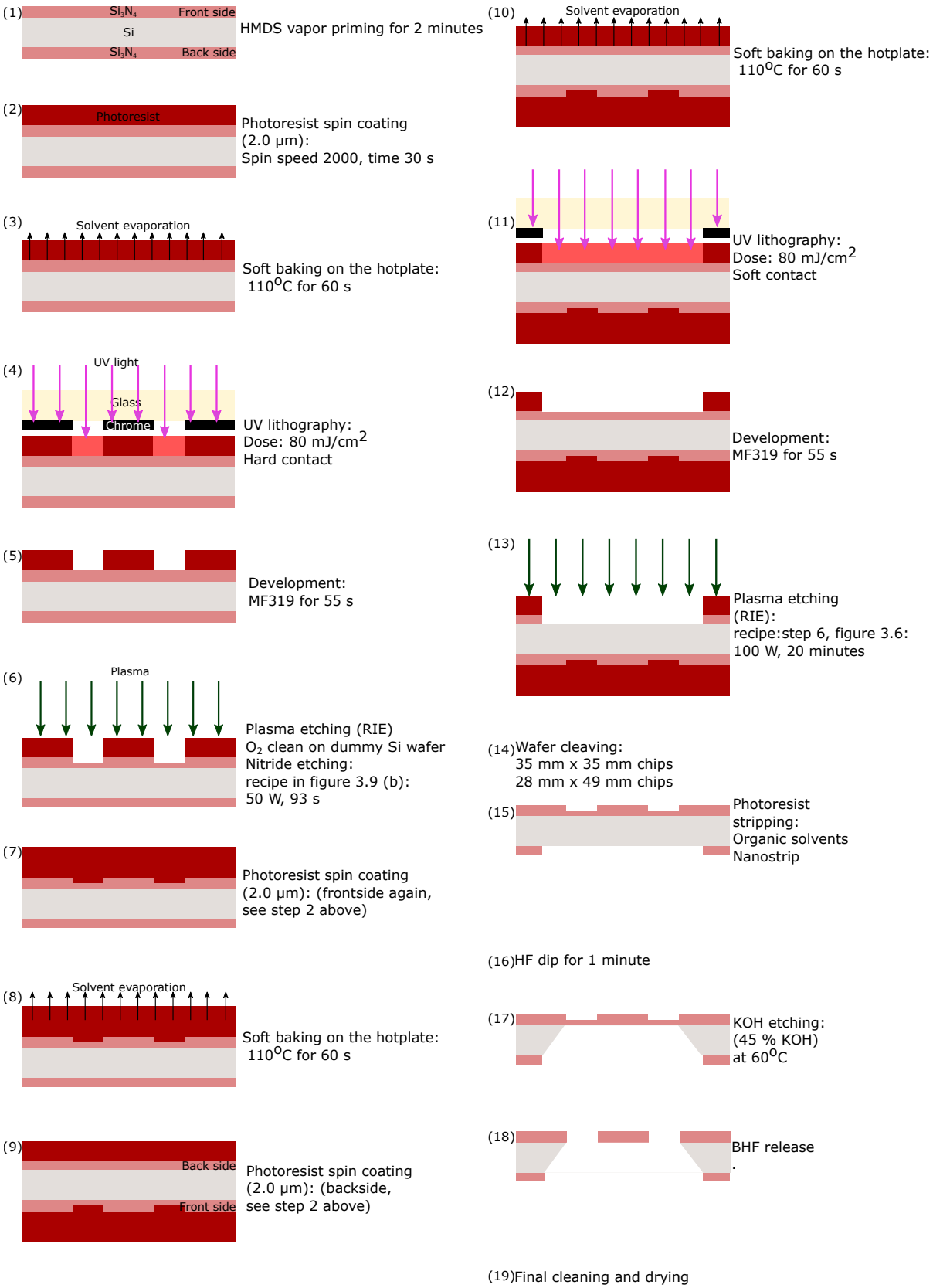

Figure 3.11: Partial etching microfabrication process flow.

At step 17, we etch the silicon in KOH, which now can only attack from the backside; this will double the etching time, as expected. We found it takes $\sim$ 46.5 hours to remove 670 μm of silicon at 56 $^{\circ}$ C, which means the etch rate of silicon at this temperature is $\sim$ 14.5 μm / hour. After all silicon is removed, we transfer the chips with the PTFE holder to a beaker of DI water, then again we transfer them to another beaker of DI water, to clean the chips of KOH. Figure 3.12 (b) shows the chip after 46.5 hours of KOH. The zoom in pictures have been taken with the optical microscope and they show the nitride thickness at different locations. We verify the thickness of the nitride on chip (297 nm) using the reflectometer after KOH; see the zoom in picture of the corner. Note that the left side of the chip is etched more than desired and there are many pinholes, this might have resulted in KOH attacking the windows that are close to the chip edge. Despite the careful handling we have applied to this partial etching run, the density of pinholes in the unpolished backside of this wafer is relatively high as compared to the polished side. Also if a pinhole forms in a device window frame, it can result in a weird irregular window shape as shown in the zoom in of the backside in figure 3.12 (b). Next, at step 18, we transfer the chips with the holder to a beaker of BHF, we make sure all chips are well immersed. We leave them inside BHF for the time needed to remove the nitride from the openings and release the structure. According to the rough estimates we have shown previously, we need around 3 hours and 18 minutes to release the structure. Figure 3.12 (c), shows the evolution of the device after successive dips in BHF; after 78.5 minutes, after 1.8 hours and then after 2.3 hours. The measured nitride thickness on the chip is consistent with what we expect each time, but all devices break when they are close to being released. Note each time we want to measure the thickness of the nitride and take a picture of the device (at each BHF stage), we transfer the chips to DI water beaker two times to rinse the acid completely. Then we transfer the chips to methanol and the hotplate to dry at 85 $^{\circ}$ C. We then measure the nitride thickness on the chip with the reflectometer.

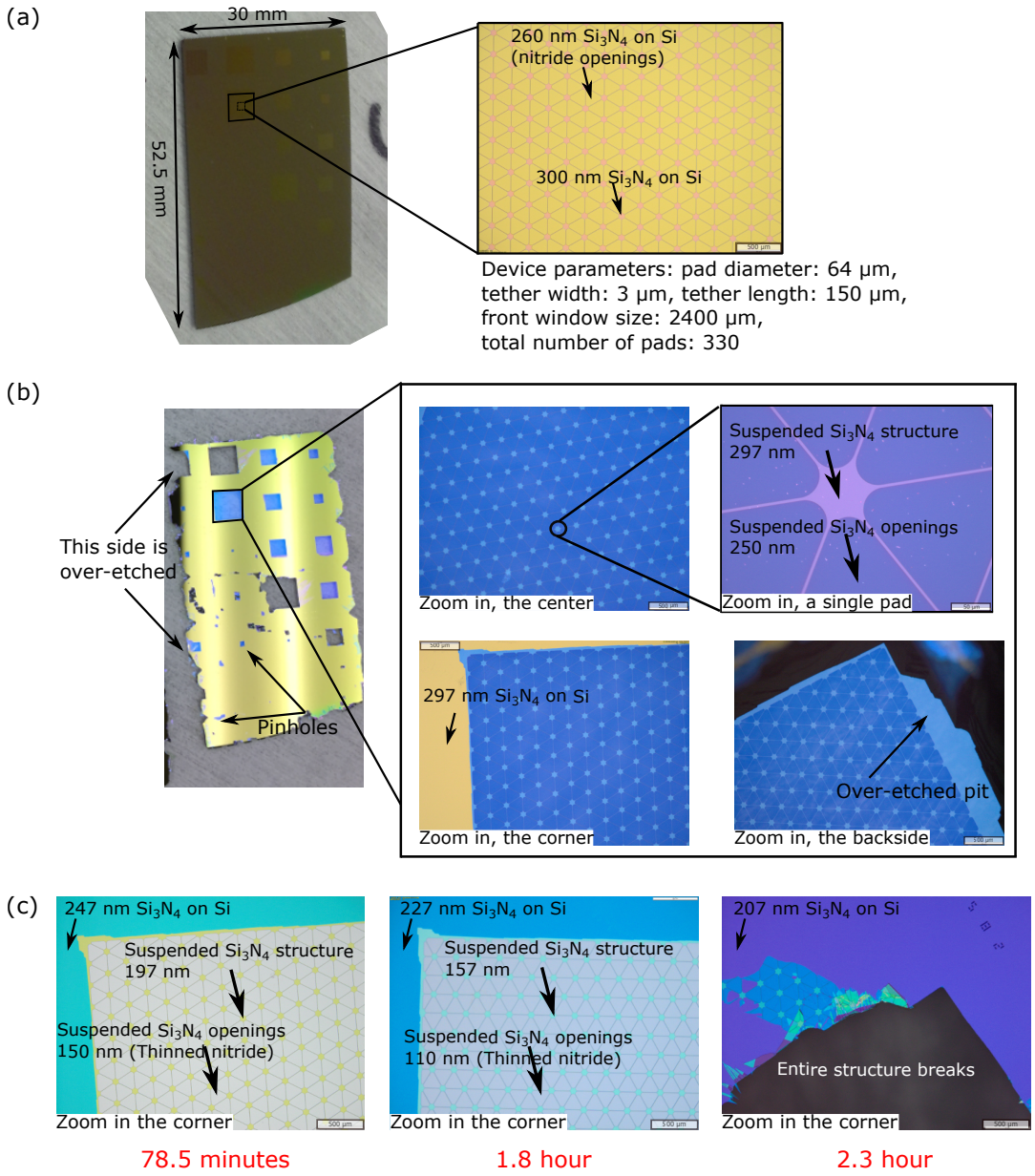

Figure 3.12: The progression of an example device until HF release. (a) The chip and the device after the photoresist stripping, step 15 of figure 3.11. Since the nitride openings are smaller than the spot size of the reflectometer laser, we estimate the thickness of the nitride from the color chart of the nitride on Si. (b) The chip and the device after HF dip (5 minutes) and KOH etching (47 hours), steps 16 and 17, figure 3.11. Over-etched side is likely due to the pinholes we observe in the unpolished side. (c) The device after successive dips in HF, step 18, figure 3.11. After each dip we transfer the chip to DI water, Methanol and hotplate, step 19, figure 3.11.

We suspect (without convincing evidence) that the devices all break due to the sudden redistribution of stress when the HF cuts its first hole in the structure. This would be

in contrast with fully etched nitride structures, wherein silicon pedestals provide structural support under each pad until just before release; releasing one pad at a time in this case likely produces a comparatively small changes in displacement and stress due to relaxation.

It may also be that we simply need to optimize this process further. The targeted devices could be thicker (e.g. 150 nm instead of 50 nm), we could use wafers polished on both sides to avoid backside pinholes, and we could "get lucky", finding a wafer with fewer pinholes. However, in parallel with this effort, we also developed another front-side protection technique that immediately yielded positive results, as will be discussed in the following sections.

3.4 SiO_2 ProTEK protective coating

In this section, we demonstrate a successful method of protecting the front side (during KOH etching) that allows for higher-yield fabrication spanning most device geometries. The concept is that after patterning the front and backsides of the wafer, we coat the front side with two layers, SiO_2 (oxide deposited on the nitride) and ProTEK (a robust polymer deposited on the oxide) prior to placing them inside KOH solution. ProTEK is the main shielding layer; however, since it is difficult to remove (often leaving residues), we use an oxide layer to prevent the polymer from adhering heavily to the nitride (the device surface). We assume the oxide might operate as a lifting off layer for the polymer, thus we reduce surface contamination in the final result. In section 3.4.1, we discuss the process flow, and in section 3.4.2, we discuss the device yield and future directions.

3.4.1 Fabrication

The details of the process flow is laid out in figure 3.13; we may view this process flow as two parts:

Part I

We start with the HMDS priming of a 6-inch single-crystal silicon wafer (<100> orientation) that is both polished and coated (by NOVA Electronic Materials) with 300 nm low-pressure chemical vapor deposition (LPCVD) silicon nitride on both sides. We follow the same recipe

and protocol we presented in step 1 of figure 3.6. Then we follow through all the steps of figure 3.13 until step 10 at which point both the front and back nitride has been patterned and fully etched. For all these steps, we employ the same corresponding recipes and protocols we previously explained in details in figure 3.6, section 3.2. The new steps begin at step number 11 of figure 3.13, which we discuss in details in part II.

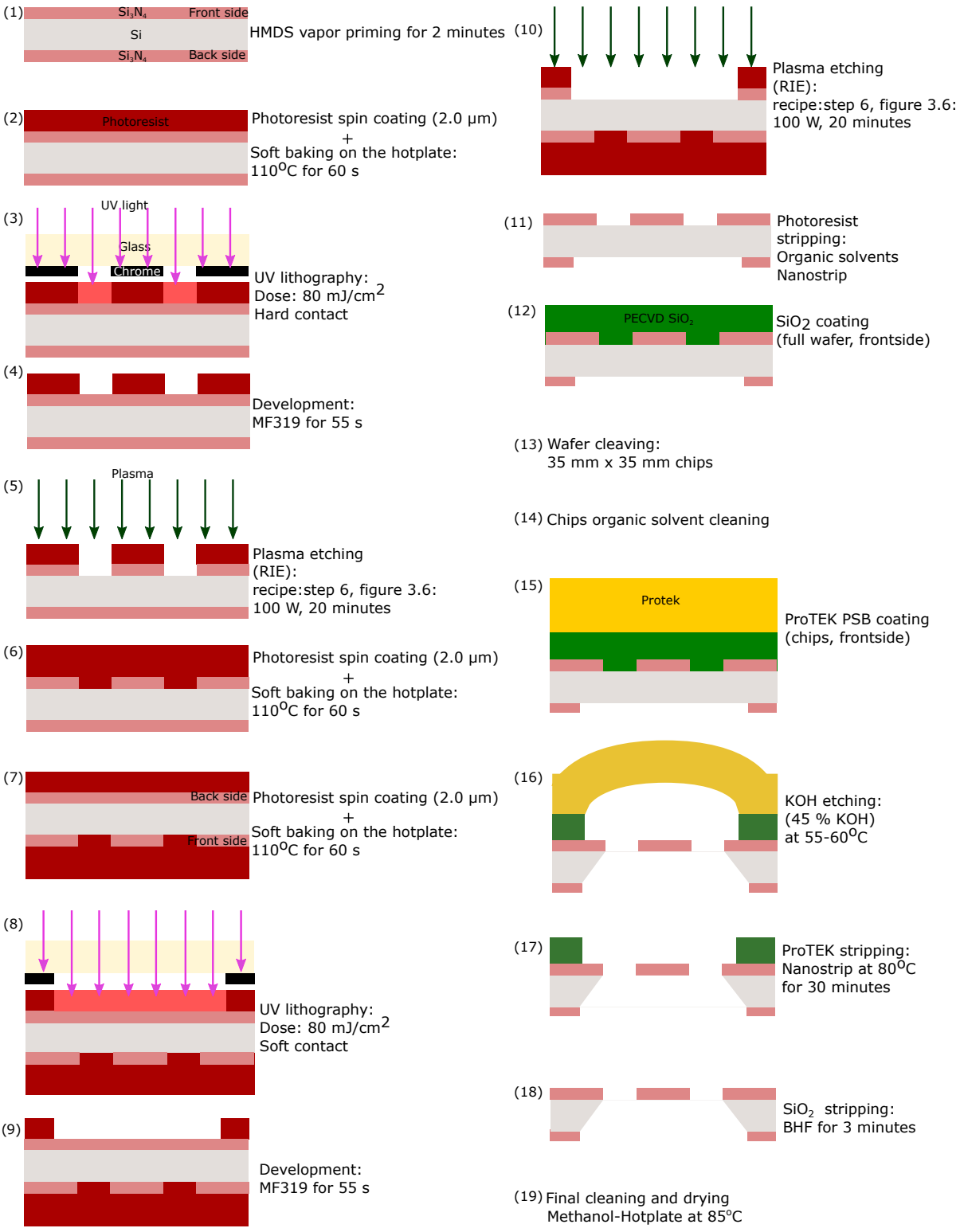

Figure 3.13: SiO_2/ ProTEK protecting mask process flow

Part II

Below are the details of the remaining steps 11-19 of figure 3.13:

11. Strip the photoresist from the entire wafer using organic solvents and acidic solution: We strip the photoresist from the two sides of the wafer using acetone. In practice, we immerse the wafer inside an acetone beaker and place the beaker inside a warm water bath at 40 $^\circ$C for 30 - 60 minutes (we agitate gently); then we transfer the wafer to IPA beaker and immerse it to remove acetone residues. Finally, we transfer the wafer to a DI water beaker and dry the wafer with the N_2 gun. We inspect the wafer under the optical microscope. If there are photoresist residues, we immerse the wafer inside a beaker of Nanostrip and heat the solution (with the wafer) on a hotplate until it reaches 90 $^\circ$C; we leave it for 30 minutes. After 30 minutes, we switch off the hotplate and allow the wafer with the solution to cool down for a couple of minutes; then we transfer the wafer to a beaker full of DI water for 1 minute. After that, we transfer the wafer again to another DI water beaker. Next, we place the wafer in the 6 inch wafer's spin dryer[8].

12. Deposit silicon dioxide (SiO_2) using plasma enhanced chemical vapor deposition (PECVD) on the frontside of the entire wafer: PECVD is a chemical vapor deposition that utilizes plasma to deposit solid thin films from gaseous species [69, 72]. When the gas species flow inside the deposition chamber, the RF power is triggered to create the plasma. The resulting energetic electrons also ionize more atoms and create more energetic radicals, that react to form the thin film on the substrate. The energetic plasma provides the necessary heat needed for the chemical reactions to take place, hence alleviating the need to incorporate an additional heating element. Generally speaking, this makes the deposition temperature in PECVD relatively low, in the range between 200 $^\circ$C and 400 $^\circ$C. PECVD SiO_2 thin films are commonly used in semiconductor industry [69, 72]. Since they are deposited at low temperatures, they can be safely applied to integrated circuits for different purposes and used for example as insulating layers. However,

[8]The spin dryer is a machine that washes 6 inch wafers with water and dry them using the centrifugal force (through spinning) and N2 gas. Wafers are installed in the 6 inch wafer cassette of the machine

these films tend to have many pinholes as compared to the films deposited at higher temperatures, but the pinholes density can be decreased by increasing the thickness and / or deposition temperature. SiO_2 thin film characteristics such as the deposition rate, the uniformity and the stress (oxide layers have compressive stress when deposited on top of silicon substrates) are controlled in a complicated manner by all deposition parameters such as the gas flow rates, the RF power, the total pressure, the temperature [69, 72]. We make this SiO_2 deposition as follows:

(a) First, we run a chamber cleaning recipe that consists of three steps, cleaning (shown in table 3.6), pumping for 60 seconds and N_2 purging for 60 seconds. We do this without any wafer in the chamber.

Parameter	Value
RF Power	700 W
Total Pressure	5 Torr
Pumping time	120 seconds
Temperature	300 °C
Gas / Flow Rate	CF_4 / 680 scc
Gas / Flow Rate	N_2O / 320 scc

Table 3.6: Pre-oxide deposition chamber cleaning recipe

(b) Second, we insert the wafer frontside up into the deposition chamber; then we run the recipe shown in table 3.7.

Parameter	Value
RF Power	125 W
Total Pressure	2.8 Torr
Deposition Time	75 seconds
Temperature	300 °C
Gas / Flow Rate	SiH_4 / 60 scc
Gas / Flow Rate	N_2O / 1200 scc

Table 3.7: Oxide deposition recipe

(c) Third, we run the cleaning recipe of the first step again to leave the chamber clean for the next user. Under these conditions, we found

a deposition rate of $\backsim$7.5 nm / second (which resulted in $\backsim$550 nm of SiO_2). We preferred to start with a relatively thick oxide film to reduce the probability of having high pinholes density. The deposition rate nonuniformity from the center of the wafer to its edge is in the range (1-4 %). In figure 3.14(a) , we show the full wafer after SiO_2 deposition, the numbers show the local deposition rate across the wafer, we use the reflectometer to measure the thickness.

13. Cleave the wafer: We apply the same procedure as in step 12, section 3.2 to cut the wafer into 35 mm x 35 mm and / or 35 mm x 28 mm chips.

14. Clean chips after cleaving: We clean the chips from the dust created during the cleaving step, to apply ProTEK on a clean surface. We immerse them and agitate for 3-5 minutes in acetone, then IPA, then DI water. Finally, we dry them with N_2 gun.

15. Coat chips with ProTEK: In this step, we coat the chips frontside with ProTEK PSB. ProTEK is a polymer coating used as a protecting mask for integrated circuits during silicon etching [73]. ProTEK coating takes place in two steps:

(a) Coat chips with ProTEK PSB primer: This is an adhesion promoter that is especially designed for ProTEK coating [73]:

1. ProTEK primer coating: We first place the chip in Laurell spin coater (frontside up). We cover from $\frac{1}{2}$ to $\frac{1}{3}$ of the chip with the primer and run the spin coating recipe with the parameters shown in table 3.8.

Step	Time (s)	Spin Speed (rpm)	Acceleration (rpm/s)
Spreading	5	500	5220
Spinning	60	1000	5220
Deceleration	5	0	5220

Table 3.8: ProTEK primer spin coating recipe

2. First baking: Then we bake the primer on the hot plate for 60 seconds at 110 $^\circ$ C.

3. Second baking: After that, we bake it for 5 minutes at 220 ° C.

4. PGMEA wash: we wash the chip frontside very well with a PGMEA solution[9]. We do this in two steps:

   - First, we hold the chip with the tweezers from one of its corners; then we spray the frontside for 30-45 seconds with the PGMEA solution. We make sure no PGMEA on the backside of the chip by blowing the backside with the N_2 gun[10].
   - Second, we place the chip on Laurell coater (frontside up) and cover it again (from $\frac{1}{2}$ to $\frac{1}{3}$ of the chip) with PGMEA; we spin dry it in Laurell using spin speed of 2000 rpm and acceleration of 1305 rpm / second for 45 seconds, table 3.9.

Time (s)	Spin Speed (rpm)	Acceleration (rpm/s)
5	500	1305
45	2000	1305
5	0	1305

Table 3.9: PGMEA spin drying recipe

(b) Coat chips with ProTEK PSB protective coating:

1. The chip is already installed in Laurell from the previous step, so we cover it (from $\frac{1}{2}$ to $\frac{1}{3}$) with ProTEK PSB protective coating and spin it at spin speed of 1500 rpm and acceleration of 5220 rpm / second for 60 seconds (table 3.10). The thickness of the ProTEK we measure in the profilometer is $\backsim$ 3.5 µm.

Step	Time (s)	Spin Speed (rpm)	Acceleration (rpm/s)
Spreading	5	500	5220
Spinning	60	1500	5220
Deceleration	5	0	5220

Table 3.10: ProTEK PSB spin coating recipe

[9]PGMEA is an organic chemical solution, known also as SU-8 developer, it is composed of 1-methoxy-2 propanol acetate, 98-100% and 2 methoxy-1-propanol acetate, 0-2%. We put this solution in a lab washing bottle to simplify the chips washing process (the spraying).

[10]This is to make sure the backside is dry before placing the chip on Laurell vacuum chuck again

2. After that we bake it on the hotplate for 2 minutes at 110 ° C.

16. Etch silicon in KOH: We load the chips into the PTFE holder; then we immerse them inside KOH 45%. We switch on the hotplate and heat the solution to 55-60 ° C; we leave them in KOH around 56-60 hours, until all the silicon is removed (they become transparent). Then we switch off the hotplate and transfer the holder with the chips to a beaker of DI water; we leave them for 2-3 minutes; then we transfer them to another DI water beaker. We leave them there until we prepare the next step.

17. Strip ProTEK in Nanostrip:

    (a) We transfer the chips with the holder to a beaker full of Nanostrip solution. We make sure the chips are well immersed. Then we transfer the beaker to the hotplate.

    (b) We heat the Nanostrip to around 90 ° C; we leave them inside for around 30 minutes[11] (until the Nanostrip solution becomes clear).

    (c) Then we remove the Nanostrip beaker carefully from the hotplate to cool down. After 3-5 minutes we transfer the chips with the holder to a beaker of DI water. We leave them for a minute, and then again transfer the chips with the holder to another DI water and immerse them inside the water for a couple of seconds (dipping for few seconds while holding the holder).

    (d) We transfer them to the BHF solution making sure they are well immersed.

18. Strip SiO_2 in BHF: We leave the chips with the holder in BHF for 3 minutes; then we transfer the holder with the chips to a beaker of DI water for 30 seconds; then to another DI water beaker where we leave them until we prepare the next step.

[11] During this time, we start preparing the BHF step; we fill a beaker with BHF and other two beakers with DI water

19. Dry the devices: We transfer the holder with the chips to a beaker of methanol; we leave them for 30 seconds before we start transferring them to the hotplate. We use the tweezers to grab one chip at a time. We place it on the hotplate at 85 $^{\circ}$ C (frontside up); we wait until all the solvent evaporates (10's of seconds).

Figure 3.14 shows images of the wafer and an example chip at various stages of fabrication from step 12 to 16. We show in (a) the full wafer after SiO_2 deposition, which is step 12 of figure 3.13. The deposition rate is relatively uniform across the wafer, with $\sim \pm$ 3 % variation. Then we show the chip after primer and ProTEK coatings, (b, c) respectively. ProTEK thickness is $\sim$ 3.5 μm with $\sim$ 2 % thickness variation across the chip. In (d) we show the chip after KOH. Note how the devices windows become transparent as all the silicon has been etched away and the chip edges become irregular in shape due to the Si etching at the chip borders, probably causing ProTEK to peel off at the edges. Then, in (e) we show zoom in pictures of some devices after KOH, these represent the different scenarios we have observed. For example, (i) shows an example where the ProTEK and the device are severely broken; it is mainly broken from the center as if the ProTEK layer has buckled. (ii) shows a broken device only at the tethers region. In (iii) the ProTEK is slightly detached but the device is fine. And in (iv) the ProTEK is not buckled ; it looks smooth and well attached to the device. Finally, in (v) the ProTEK is broken and detached from the device however, the device survives.

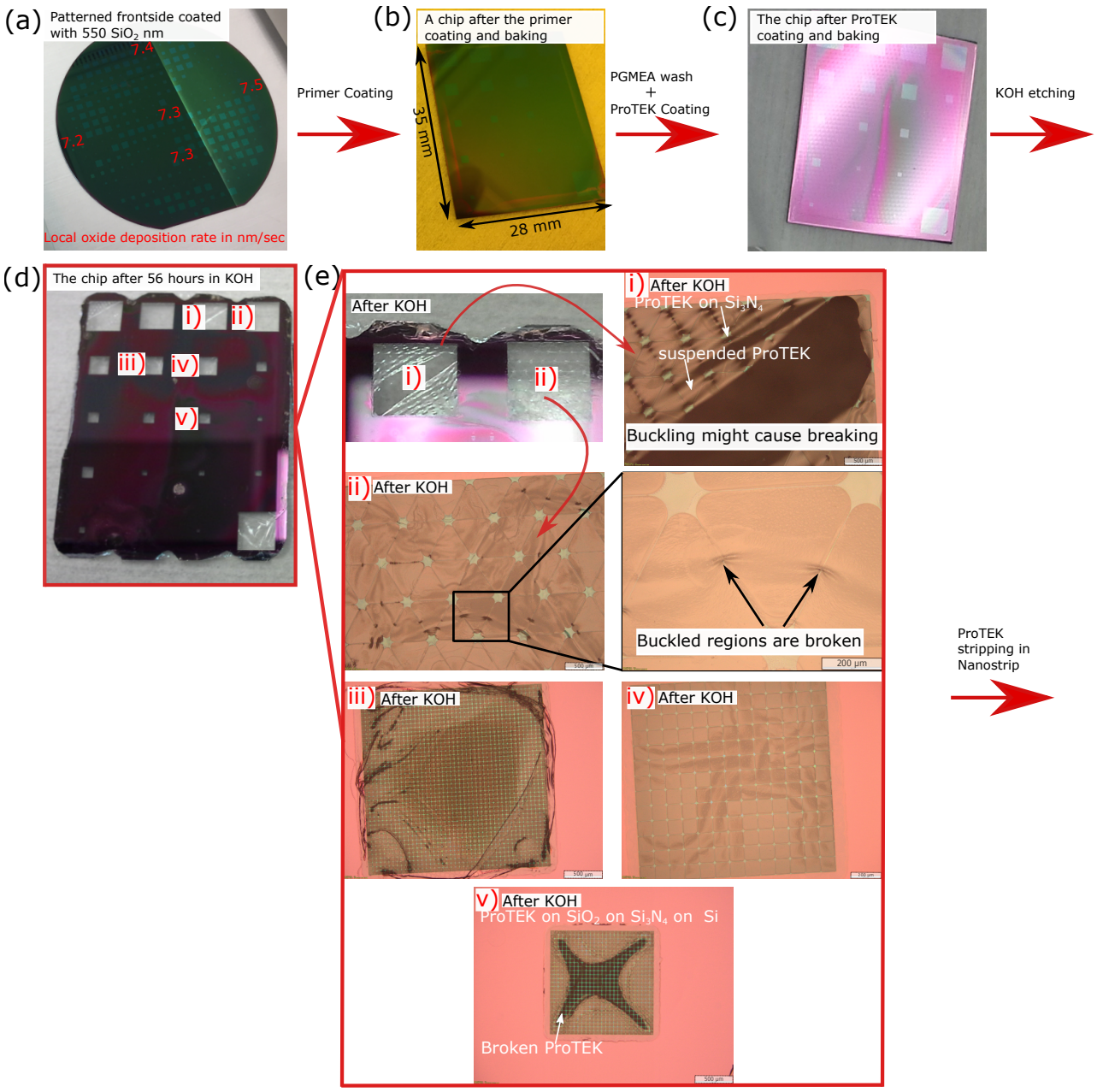

Figure 3.14: The progression of an example chip and its devices from step 12 to 16 of figure 3.13. (a) The wafer after the SiO_2 deposition, step 12, figure 3.13. (b) An example chip after the Primer coating and baking. (c) The chip after ProTEK coating and baking. (d) The chip after KOH etching. The devices are labeled with numbers; (e, i-v) a zoom in on some of the devices shows SiO_2/ ProTEK coating after KOH. The devices parameters are: (e : i) 128 µm pad diameter, 3 µm tether width, 350 µm tether length,4430 µm front window size, and 56 pads, (e : ii) 128 µm pad diameter, 2 µm tether width, 405 µm tether length, 4250 µm front window size, and 49 pads, (e : iii) 16 µm pad diameter, 3 µm tether width, 35 µm tether length, 2450 µm front window size, and 1849 pads, (e : iv) 16 µm pad diameter, 1.5 µm tether width, 70 µm tether length, 1320 µm front window size, and 144 pads, (e : v) 16 µm pad diameter, 5 µm tether width, 53 µm tether length, 1300 µm front window size, 625 and pads.

In figure 3.15, we continue showing the progression of some of the devices, after ProTEK and SiO_2 stripping. In (a) we show the chips inside the hot Nanostrip after 5 minutes; the ProTEK starts to peel off. Then after 30 minutes, (b), the ProTEK dissolves and the Nanostrip solution becomes clear. In (c, e, g) we show the same devices of (e), figure 3.14, after ProTEK stripping in Nanostrip, while in (d, f, h) we show them after the oxide stripping in BHF. By comparing the pictures, (c) vs. (d), (e) vs. (f), (g) vs. (h), we suspect that the SiO_2 layer that is covering the devices underneath the ProTEK has been etched away, while chips are inside KOH (note the color difference between the device borders and the rest of the chip). It is known that KOH etches PECVD oxide films rather quickly as compared to LPCVD ones [74], and once it is through, it can attack the oxide around the edges from underneath the ProTEK as it lifts away. After we strip the oxide layer in BHF, the color of the chip becomes the same as the device borders; we use this as a rough indication (by eye) that we removed the oxide. This is consistent with the fact that the etch rate of SiO_2 in BHF (measured value) is $\backsim$430 nm / minute, which means that 3 minutes in BHF should be enough to remove all the oxide.

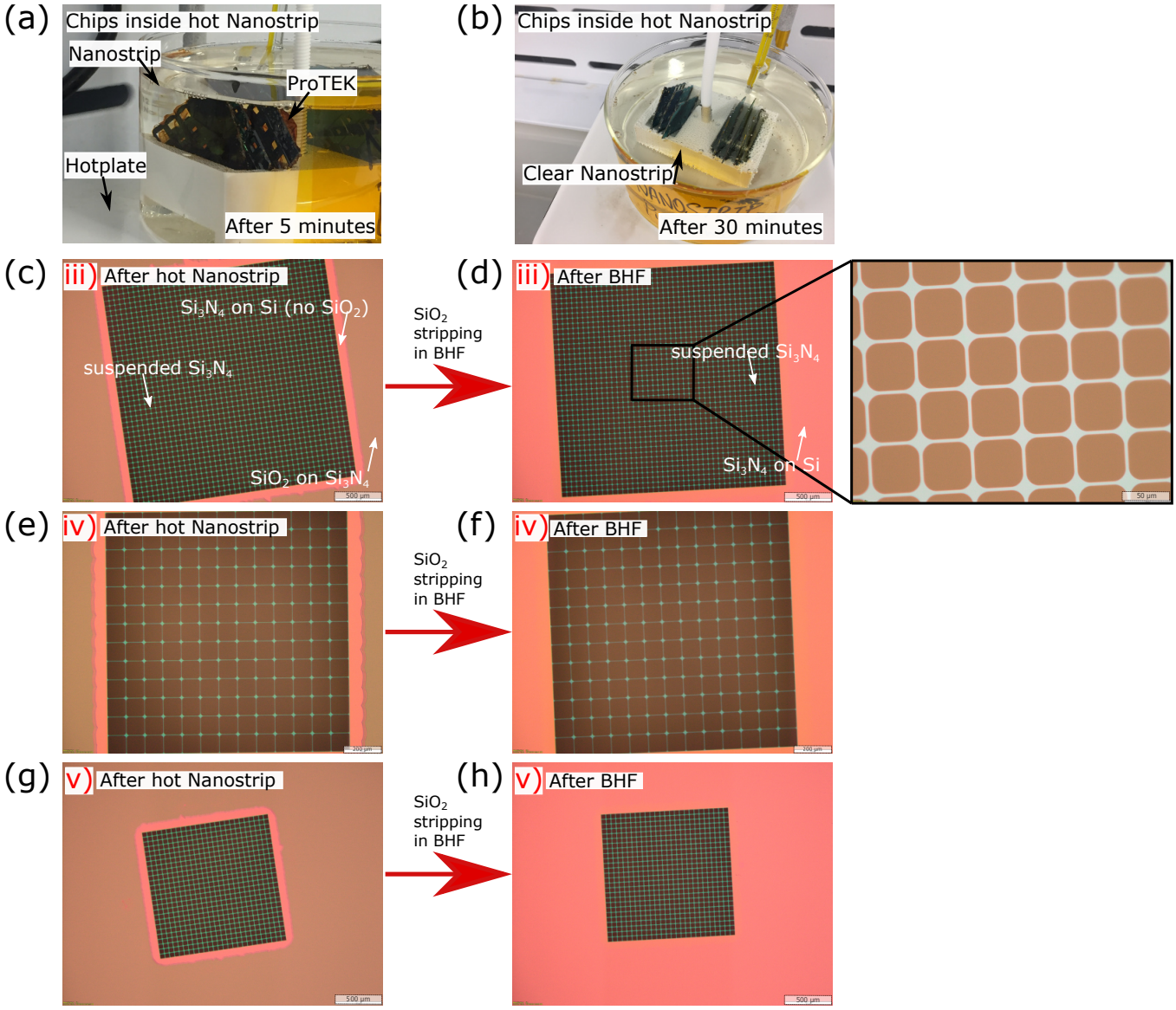

Figure 3.15: The progression of an example chip and its devices from step 17 to 19 of figure. (a), (b) Chips inside hot Nanostrip after 5 and 30 minutes respectively. (c - e) Same devices shown in (e, iii-v) of figure 3.14 after ProTEK and oxide stripping. The devices parameters are: (c : iii) 16 µm pad diameter, 3 µm tether width, 35 µm tether length, 2450 µm front window size, and 1849 pads, (d : iv) 16 µm pad diameter, 1.5 µm tether width, 70 µm tether length, 1320 µm front window size, and 144 pads, (e : v) 16 µm pad diameter, 5 µm tether width, 53 µm tether length, 1300 µm front window size, and 625 pads. Note: in the inset of (d), the reader should not confuse the "mice on a fence" optical illusion with contaminants on the pads [75].

3.4.2 Device yield and discussion

Other examples of surviving devices are shown in figure 3.16; hexagonal phononic crystals with relatively large pads as compared to the one (PD 16 μm) shown in figure 3.15. The overall yield of this process flow is 56 % (47 survived / 85 devices (hexagons+squares)) with 90% of the devices clean. The remaining 10% of the devices have some residues (5 devices / 47 survived devices), see (k-l) of figure 3.16 as an example of the residues we have seen. These residues can be introduced at any step in the process flow (we did not take pictures of each step as we did for the devices in figure 3.14 and figure 3.15), however since all the devices are clean until step 11 of figure 3.13, we assume that these might be KOH or ProTEK residues. Eventually, we plan to characterize the chemical make-up of these residues and develop additional cleaning techniques, but for now this process produces enough devices to pursue the physics of Chapter 2.

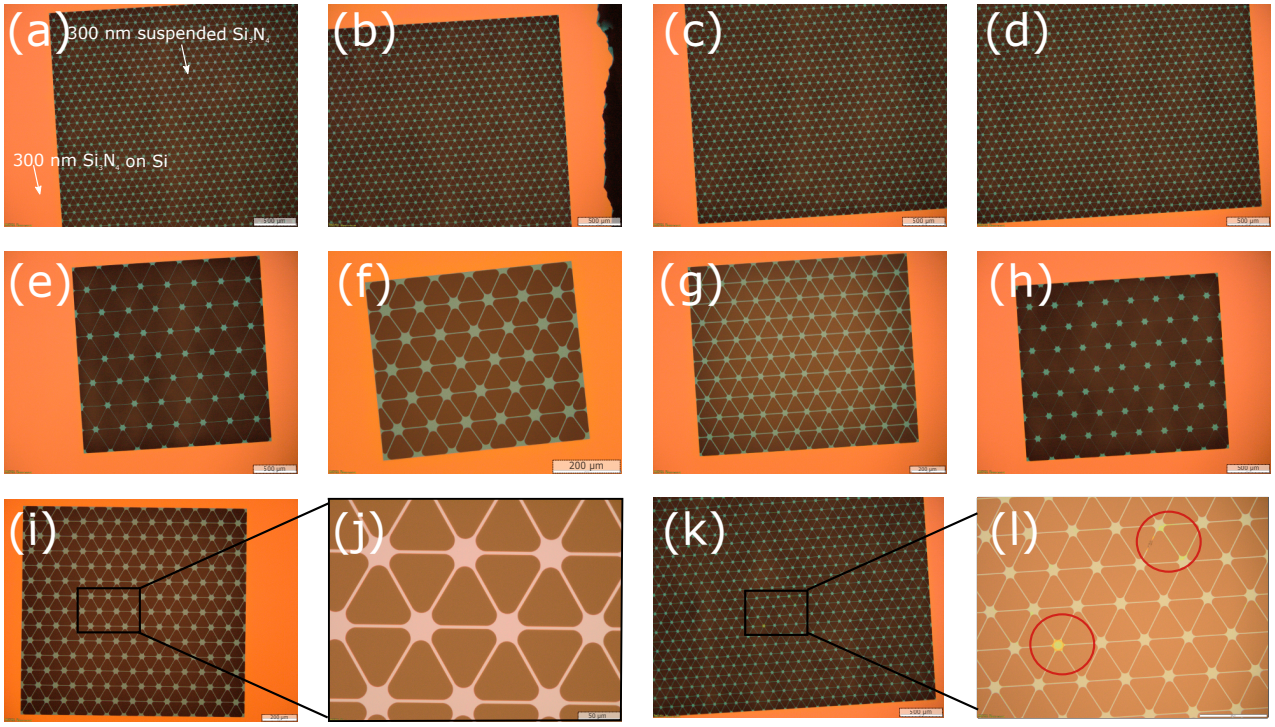

Figure 3.16: Hexagonal phononic crystals fabricated using the process flow in figure 3.13. (a-d) The four corners of a device with 32 µm pad diameter, 3 µm tether width, 55 µm tether length, 4500 µm front window size, and 2156 pads. (e) has the following parameters: 64 µm pad diameter, 3 µm tether width, 220 µm tether length, 2240 µm front window size, and 49 pads. (f) has the following parameters: 32 µm pad diameter, 3 µm tether width, 55 µm tether length, 620 µm front window size, and 30 pads. (g) has the following parameters: 32 µm pad diameter, tether 5 µm width, 85 µm tether length, 1300 µm front window size, and 90 pads. (h) has the following parameters: 64 µm pad diameter, 1 µm tether width, 200 µm tether length, 2400 µm front window size, and 56 pads. (i-j) has the following parameters: 32 µm pad diameter, 3 µm tether width, 55 µm tether length, 1326 µm front window size, and 169 pads. (k-l) has the following parameters: 32 µm pad diameter, 3 µm tether width, 85 µm tether length, 4400 µm front window size, and 1258 pads. Note that only 10 % of the devices fabricated using this method shows residues as the one shown in (k-l), otherwise 90% are clean.

Figure 3.17 shows a three dimensional space of survived and broken devices of both geometries (hexagons and squares) as a function of PD (pad diameter), TEL (tether length) and total number of pads. Note how this method allows us to achieve delicate devices with several hundred pads in a single device. In this map, we do not show the survival statistics dependency on TEW. Generally speaking, the survival rate of the devices with small pad diameters and relatively short tether lengths is higher than the case of relatively bigger pads diameters and long tether lengths. Interestingly, this is the opposite trend as that found for

the fabrication protocol of section 3.2, wherein the frontside is not protected. The ProTEK pictures after KOH etching we show in figure 3.14 ,(e i) (e-ii), and the low survival rate of the devices with relatively big PD and long TEL, make us suspect that the buckling induced by the compressive stress in the oxide layer might be one reason why these devices do not survive with this current scheme (550 nm SiO_2/ ProTEK). This result has motivated us to consider a fabrication scheme where we do not apply oxide and we only use ProTEK coating directly on the nitride.

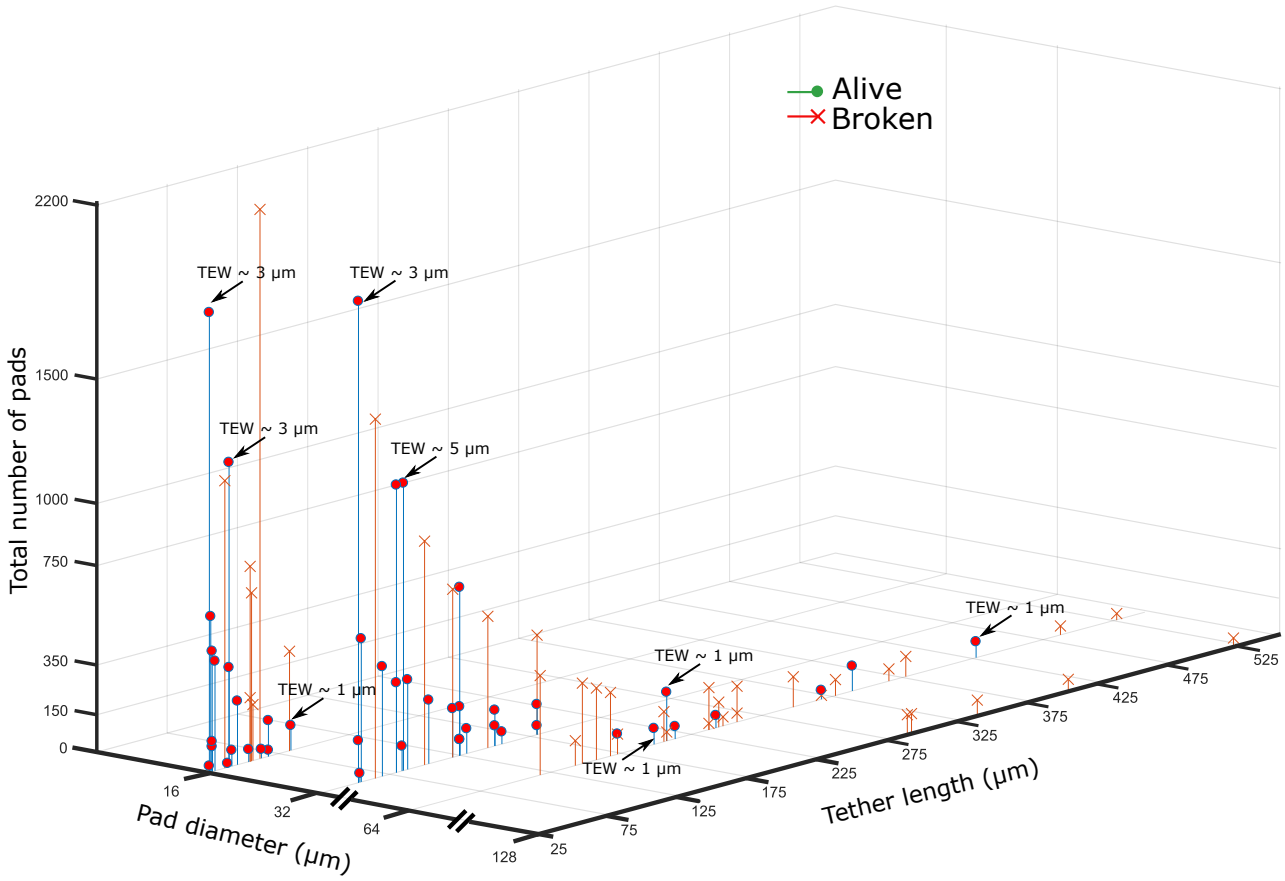

Figure 3.17: Summary of SiO_2 / ProTEK coating process flow. Three-dimensional space map that shows the survived (circles) and broken (crosses) devices as a function of the PD, TEL and the total number of pads; the map has considered hexagons and squares together. The arrows show the tether width (TEW) of the corresponding membrane. Note: TEW values here have been taken from the photomask design, no scanning electron microscope (SEM) measurements have been done yet.

3.5 ProTEK only mask

In this section, we illustrate the fabrication of the phononic crystals using ProTEK PSB alone. The process flow is the same as the one presented in the previous section without an oxide layer; we show it in figure 3.18. Then in section 3.5.1 we discuss the device yield.

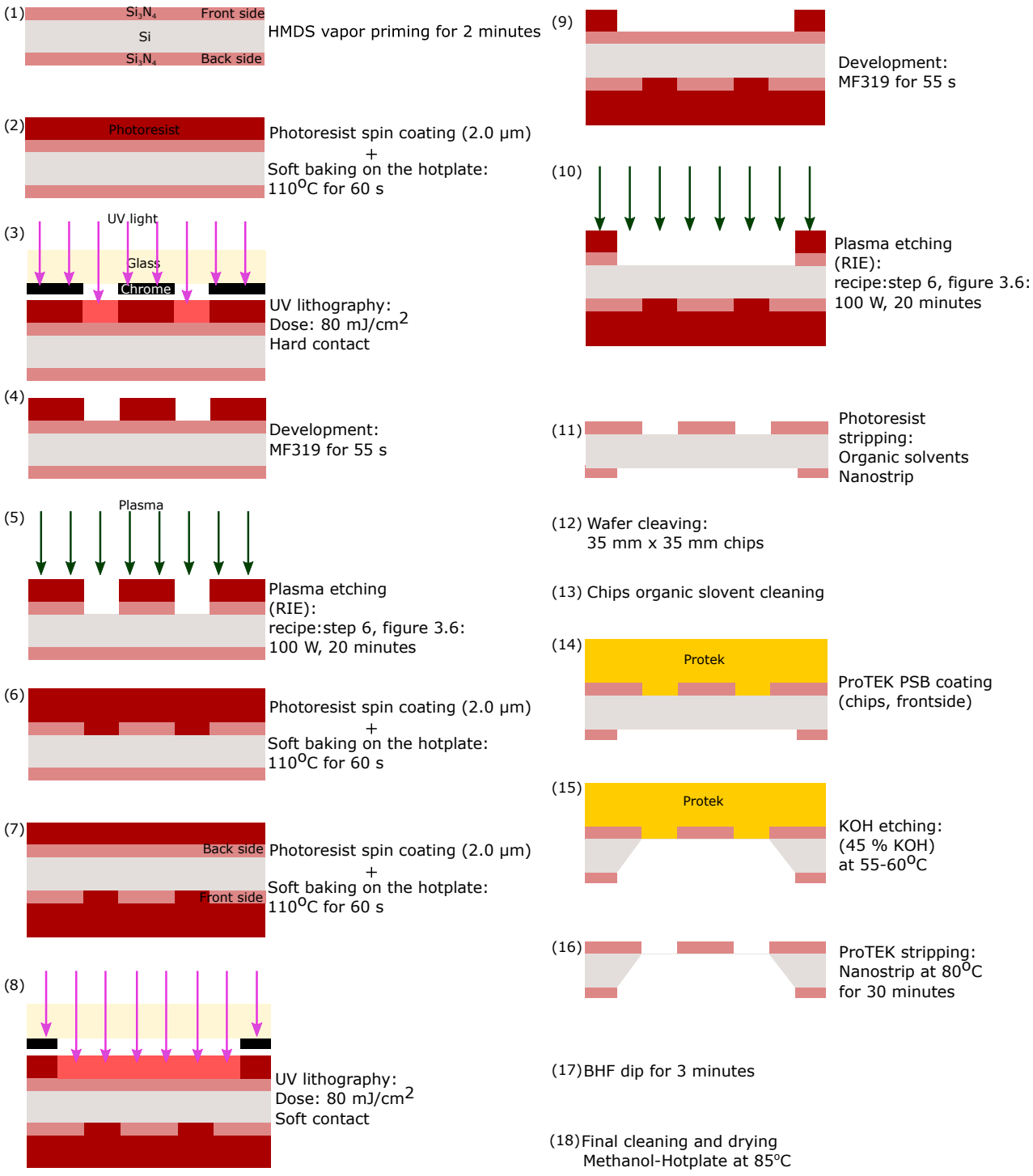

Figure 3.18: ProTEK coating process flow.

3.5.1 Device yield and discussion

Figure 3.19 shows a three dimensional space of survived and broken devices of both geometries (hexagons and squares) as a function of PD, TEL and total number of pads. In this map, we do not show the survival statistics dependency on TEW.

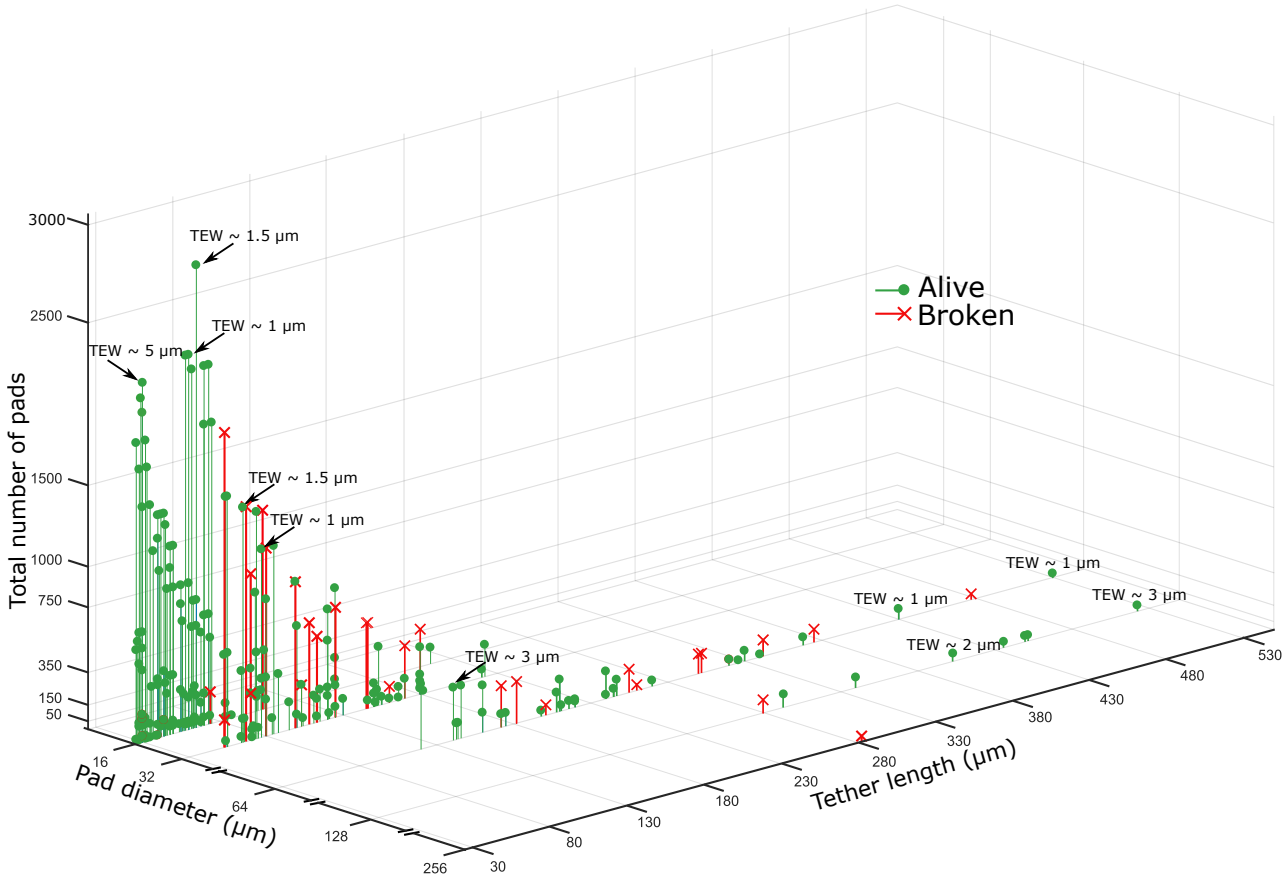

Figure 3.19: Summary of ProTEK coating process flow. Three-dimensional space map that shows the survived (circles) and broken (crosses) devices as a function of the PD, TEL and the total number of pads; the map has considered hexagons and squares together. The arrows show the tether width (TEW) of the corresponding membrane. Note: TEW values here have been taken from the photomask design, no scanning electron microscope (SEM) measurements have been done yet.

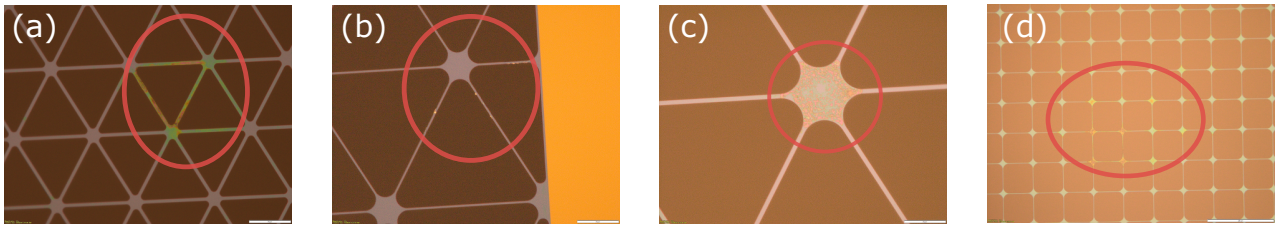

Figure 3.20: Examples of residues we see on the devices.

The total number of devices fabricated using this process flow is 252. Of those, 88% have survived (222 / 252 devices). Also, many devices that fail in the oxide / ProTEK process flow survived when fabricated using this scheme. This suggests that the absence of the oxide layer has positively contributed to this high yield, and that the elimination of the oxide buckling due to compressive stress might be the reason, particularly for the devices with big PD and long TEL. However, only 26% of them are clean under the optical microscope (57 / 222 devices); the majority of the devices have residues. However, the residues are confined to small areas (i.e. on the scale of a single unit cell, as in figure 3.20 above), and the vast majority of each device is clean. Figure 3.20 shows some examples of the residues we see in the final inspection after step 18, figure 3.18. We might have introduced these residues in one of the steps between step 13 and 18, figure 3.18. And since we have not taken microscopic pictures after these steps, or made a chemical analysis for the final device, we can not identify their nature.

At this stage with these available information, it might be beneficial to execute more cleaning steps to check the possibility of any improvement. For example, we could apply two steps ProTEK stripping protocol; we transfer the chips to a second fresh hot Nanostrip solution, for 30 minutes or even longer to remove the left-over residues, after the first ProTEK Nanostrip step. Or we could try the O_2 plasma, as recommended by ProTEK PSB specification sheet [73]. However, we can say that devices fabricated with an oxide/ProTEK bilayer were significantly cleaner than these (see section 3.4), hinting that the oxide does play a helpful role in removing residues. Perhaps using a thinner oxide layer would eliminate stress-induced buckling while still allowing us to realize a higher percentage of pristine devices.

Ultimately, this fabrication scheme has allowed us to realize many (thousands) pads quite

delicate devices with wide range of device parameters. For example, for small pad diameter (16 μm), we produce devices with up to 2750, 2304, 2025 pads (4.4 mm, 2.4 mm window sizes), figure 3.21 (a, b, c); these devices have pretty narrow tether width: 1.5, 1 and 5 μm, respectively. Other examples of a smaller windows are shown in (d, e, f). We also show in (g-j) examples for large pad diameter devices (64 and 128 μm) some with 4.4 mm window size and long tethers, similar to some devices produced in section 3.2; we circle residues with a white circle in (a) and (j).

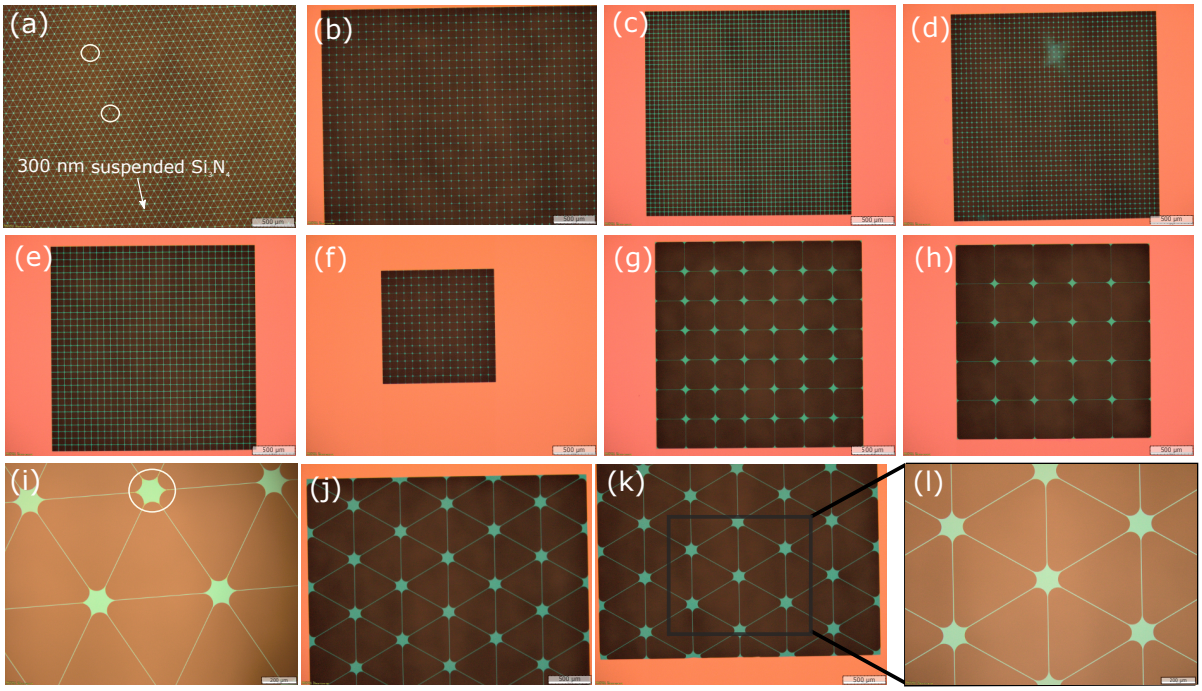

Figure 3.21: Examples of delicate devices produced using ProTEK process flow, figure 3.18. (a) Shows the center region of a device that has the following parameters: 16 μm pad diameter, 1.5 μm tether width, 65 μm tether length, 4420 μm front window size and 2750 pads. (b) Shows a corner of a device that has the following parameters: 16 μm pad diameter, 1 μm tether width, 58 μm tether length, 4440 μm front window size, and 2304 pads. (c) Shows a device with the following parameters: 16 μm pad diameter, 5 μm tether width, 30 μm tether length, 2450 μm front window size, and 2025 pads. (d) has the following parameters: 16 μm pad diameter, 2 μm tether width, 28 μm tether length, 1345 μm front window size, and 1681 pads. The little green spot under the device is a broken piece from other devices that was settling under the device on the clean room wipe. (e) has the following parameters: 16 μm pad diameter, 5 μm tether width, 60 μm tether length, 2450 μm front window size, and 900 pads. (f) has the following parameters: 16 μm pad diameter, 1 μm tether width, 60 μm tether length, 1350 μm front window size, and 196 pads. (g) has the following parameters: 64 μm pad diameter, 1.5 μm tether width, 220 μm tether length, 2480 μm front window size, and 36 pads. (h) has the following parameters: 64 μm pad diameter, 1.5 μm tether width, 340 μm tether length, 2300 μm front window size, and 16 pads. (i) Shows the center region of a device that has the following parameters: 128 μm pad diameter, 3 μm tether width, 523 μm tether length, 4350 μm front window size, and 36 pads. (j-l) Two corners and a zoom in of a device with 128 μm pad diameter, 5 μm tether width, 450 μm tether length, 3900 μm front window size, and 36 pads. (a) and (i) have residues circled with white.

We should also note that, while the devices may look clean under the microscope, they may still have residues, fabrication imperfections, thickness variations across the device, or tiny fractures that we cannot see. This disorder would undoubtedly produce defect mechanical

modes within the gap [61] that would interfere with the physics we hope to realize. In the following section, we measure the spectrum of normal modes in one of the "pristine" devices to verify that a complete bandgap (for out-of-plane motion) exists in these structures.

3.6 Preliminary mechanical characterization

In this section, we show preliminary measurements of the mechanical frequency spectrum for two example devices. As expected, the spectra demonstrate the presence of the band gap with a ratio of gap width to band edge frequency as high as 80 %. Using a relatively simple laser interferometric circuit, we achieve a noise floor of 100 fm/$\sqrt{\text{Hz}}$. This is sufficient to resolve the Brownian motion (i.e. each mechanical mode's response to thermal force noise [76, 77]) of the modes in ultrahigh vacuum.

Figure 3.22 shows the basic fiber and electric circuit we use to record the spectrum of the phononic crystal membranes [2]. We send an infrared laser beam (Thorlabs diode laser CLD1015, 1550 nm) through an optical fiber coupler (Thorlabs 90:10 fiber coupler). Nitride films are transparent in this wavelength which ensures minimal absorption and heating. The coupler splits the laser power into two signals 90% & 10%, and an isolator after the laser blocks back-reflected signals, reducing laser noise and preventing damage. The 10% signal goes to the fiber that interacts with the membrane inside the ultrahigh vacuum chamber (UHV, 10^{-9} torr), this power percentage is sufficient to give a good reflection signal without heating the membrane; in figure 3.22, we have labeled this signal red. This signal is reflected from the surface of the membrane carrying the vibrational information and interferes with the part that is reflected from the inner tip surface of the cleaved fiber; the combined signal is labelled with blue arrows in figure 3.22. This reflected signal goes back to the coupler and 90% of that is then directed to a photodetector (PD "1" in figure 3.22). The photodetector coverts the alternating optical signal ($E(x,t)$, the electromagnetic field) to a voltage signal $V(t)$ proportional to the power, $\left\langle |E(x,t)|^2 \right\rangle \propto V(t)$, (where the angle brackets indicate a time average / low-pass filter with a bandwidth of $\sim$ 150 MHz for our photodiodes (Thorlabs PDA10CF). This voltage signal is then sent to a spectrum analyzer (Zurich Instruments HF2 lock-in), and the final signal is converted into displacement units using the known functional

form of the interference fringe in the reflected signal; see the extensive discussion in Christoph Reinhardt's dissertation (McGill Physics, 2017).

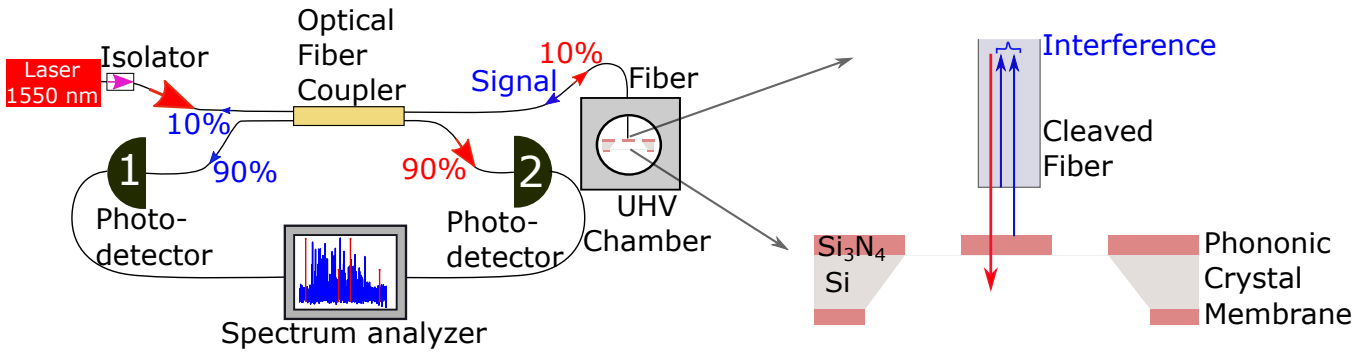

Figure 3.22: Laser interferometer circuit to measure the mechanical mode's Brownian motion. A 1550 nm laser beam (red) is split through an optical fiber coupler to 90% and 10% signals (the isolator after the laser blocks back reflection). The 10% signal goes to the fiber that interacts with the membrane inside the ultrahigh vacuum chamber. This signal is reflected from the surface of the membrane carrying the vibrational information and interferes with the part that is reflected from the inner tip surface of the cleaved fiber; the combined signal is labelled with blue arrows. Photodetector "1" then coverts 90% of this blue signal to a voltage. The voltage then is sent to a spectrum analyzer. The second coupler arm (red, 90%) is simultaneously measuring the laser classical noise, the shot noise and the photodetector noise; this is done using photodetector "2" and a spectrum analyzer.

Figure 3.23 shows a typical spectrum from a device having 64 μm pad diameter, 3 μm tether width, 344 μm tether length, 4200 μm front window size, and 90 pads. Notice the cluster of peaks spanning the range 188-340 kHz, and a cluster spanning the range 660-740 kHz . The gap in between these clusters roughly matches the gap predicted by COMSOL to within 6 %, as indicated. In this case the band gap is 70 % of the band edge frequency.

In addition to information about membrane motion, the resulting power spectral density (PSD) includes classical and shot noise from the laser as well as photodiode noise [78, 79]. The latter two simply add a broadband background to the spectrum, but the laser's classical noise has peaks. We identify the peaks within the band gap (highlighted in red) as coming from the laser by simultaneously measuring the spectrum of noise on the other arm of the coupler (photodiode "2" in figure 3.22). Currently, we are planning to either develop a differential circuit to subtract this classical noise from our signal, or find a lower-noise laser (ideally one that is quantum-limited over this frequency range). For now, however, we are reasonably

confident that there are no accidental defect modes within the gap (i.e. presuming they didn't happen to coincide with the laser noise peak!).

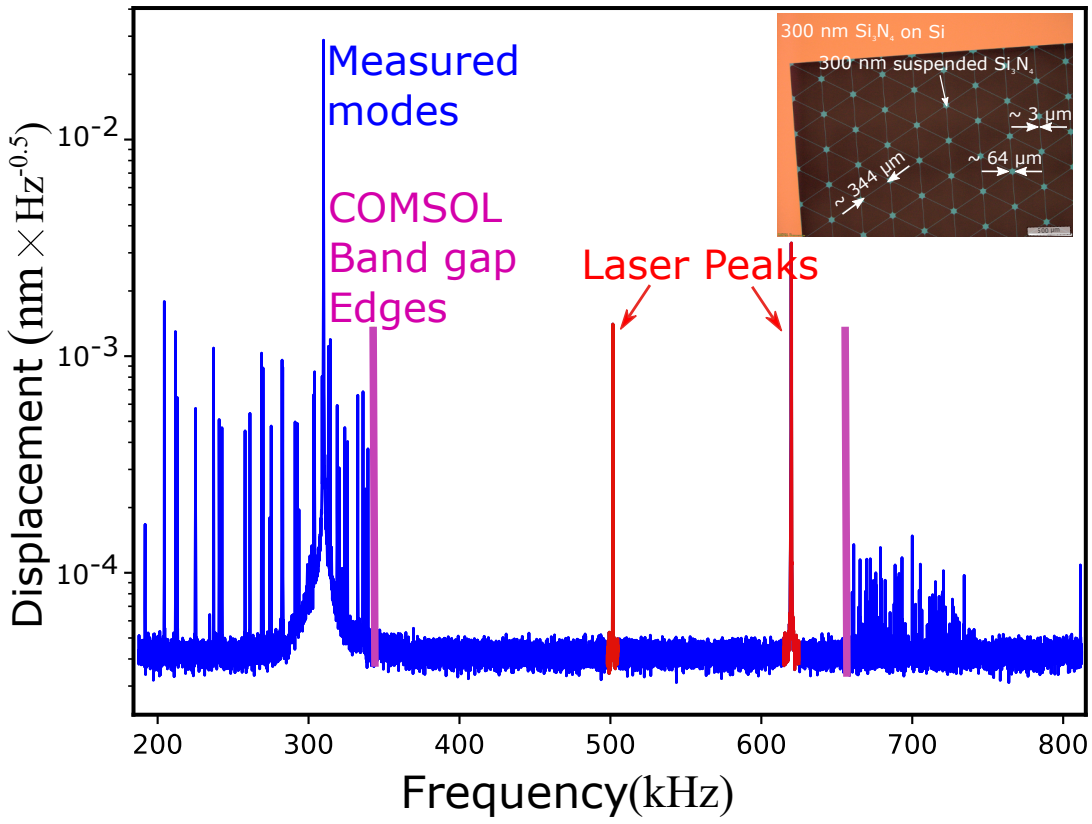

Figure 3.23: Thermal power spectral density of an example device shown in the optical microscope inset. The device has the following dimensions: 64 µm pad diameter, 3 µm tether width, 344 µm tether length, 4200 µm front window size and 90 pads. The blue peaks are the mechanical modes measured using the laser interferometer introduced in figure 3.22. The first blue peak bundles in the range (188 - 340 kHz) is separated by a gap from the second blue peak bundles in the range (660 - 740 kHz). The magenta lines highlight the gap predicted by COMSOL. The gap between the blue modes clusters roughly matches the gap predicted by COMSOL to within 6%. The two red peaks located inside the band gap are classical laser noise peaks.

Figure 3.24 shows results for another example device that has 128 µm pad diameter, 1 µm tether width, 350 µm tether length, 4500 µm front window size, and 81 pads. It similarly shows a bandgap, this time with a gap:edge ratio of 80%. In this case, however, we see peaks within the gap (gold) that we cannot attribute to laser noise. We suspect these are mechanical defect modes due to severe structural damage (cracks, fabrication defects) that are not visible when inspecting the device with an optical microscope.

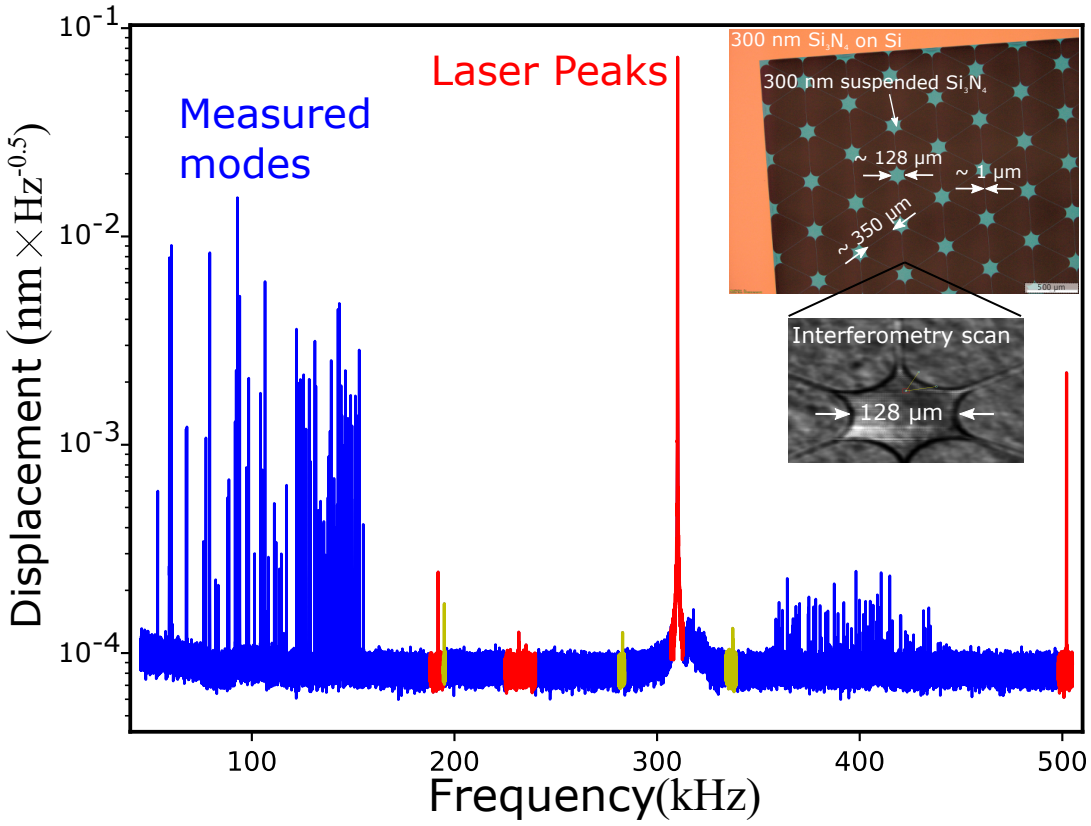

Figure 3.24: Thermal power spectral density of an example device shown in the insets, the first inset is an optical microscope image and the second one is an interferometric scan image. The device has 128 µm pad diameter, 1 µm tether width, 350 µm tether length, 4500 µm front window size, and 81 pads. The blue peaks are the mechanical modes measured using the laser interferometer introduced in figure 3.22. The band gap is between the first and second blue modes clusters (which span the ranges (53 - 155 kHz) and (360 - 435kHz), respectively). We attribute the red peaks to the classical laser noise and the gold ones to possible mechanical defects that might be due to severe structural damage (cracks, fabrication defects).

3.7 Summary

In this chapter, we demonstrated the fabrication of delicate 100-nm-thick and 300-nm-thick Si_3N_4 suspended phononic (hexagonal and square) crystal membranes with wide range of dimensions and an area as large as 20 mm^2, with thousands (up to 2750 pads) pads and as narrow as $\sim$ 1.5 µm tether width (with a ratio of gap width to band edge frequency as high as 80 %). We realized several fabrication techniques, based on standard photolithography,

each having it is own leverages and drawbacks. The existing (unprotected front side during release in KOH) process flow [2] allows us to produce clean, delicate devices with tens of large pads and long tethers but with a relatively low yield. However, by implementing some modifications, section 3.2, we found that it is possible to double the yield of this technique, to become 35 %. On the other hand, protecting the frontside with SiO_2/ ProTEK bilayer, section 3.4, (during release in KOH) has boosted the yield to 56% (90 % of them is clean). We produced more delicate membranes as compared to those produced by the unprotected front side technique, and, in particular, the yield has improved for membranes with hundreds of small pads and short tethers. The results we show suggest that the buckling induced by the compressive stress in SiO_2 might be the reason why large pads, long tethers membranes fail this scheme and that this process could be further optimized by fine tuning the oxide thickness. Interestingly, protecting the front side with ProTEK only, section 3.5, (by removing the oxide) does improve the yield of all membrane dimensions up to 90%. We produced suspended membranes with thousands (up to 2750 pads), hundreds and tens of small and large pads, long and short tethers, but 26 % of them are clean, which suggests that it might need cleaning optimization in the future. However, we should emphasize that the successful schemes we attempted here have produced enough pristine devices that should allow us to realize the physics we seek in chapter 2. Preliminary mechanical characterization of two example devices confirms that they can exhibit the phononic bandgap required for laser-induced localization experiments.

Chapter 4

Summary and Outlook

In this dissertation, we have proposed and demonstrated some initial steps toward exploiting radiation pressure to strongly tune the geometry and mass of a mechanical system. The basic idea is to fabricate an extended phononic crystal structure [27] and apply an optical trap to one lattice site, thereby creating a defect that exponentially localizes one or more mechanical modes.

In chapter 1, we reviewed the work done in this field. Noting that the geometry and mass have also been tuned via optically mediated normal-mode hybridization [19, 21, 22, 23, 24, 25, 26] but not so profoundly: only a few (essentially two) normal modes are involved, and the resulting hybridized modes therefore exhibit a mass and spatial extent comparable to that of the unperturbed modes. We also discussed some of the potential research directions enabled by this type of coupling. In particular, we suspect the ability to optically tune the spatial extent of a mechanical mode will provide a unique platform for fundamental dissipation studies, unconventional sensing applications, and quantum optomechanics experiments.

In chapter 2 we explored the physics of this optically mediated geometry and mass tuning in a semianalytical toy model in one dimension (1D), and then applied this intuition to guide the design of a realistic two-dimensional implementation, using finite element model (COMSOL). Importantly, we find that it is possible to vary the spatial extent and the amount of participating mass in the oscillation of these optically defined defect modes by many orders of magnitude. And that even a single photon can cause a macroscopic change in the amplitude that can be detected in a millimeter-scale membrane. We find surprisingly

good agreement between our 1D model and the 2D simulation, with the 1D model predicting band edge frequencies within $\sim$ 20 % of those simulated, and a semi-quantitatively similar response to an applied optical trap. We derived a few figures of merit for this style of optomechanical coupling to assess the localization efficiency, namely the localization length (and effective mass) and the ratio of the trapped pad's amplitude with the trap on and off for a fixed mechanical energy stored in the mode. We found that, despite the larger mass, large structures result in large response to a given trap as compared to small structures.

Then, in chapter 3, we demonstrated several fabrication schemes, each having their own leverages and drawbacks. We find that it is possible to fabricate delicate 100-nm-thick and 300-nm-thick Si_3N_4 suspended phononic (hexagonal and square) crystal membranes with wide range of dimensions and an area as large as 20 mm^2, with thousands (up to 2750) unit cells and as narrow as $\sim$ 1.5 μm tether width (with a ratio of gap width to band edge frequency as high as 80 %). We find that by protecting these delicate structures from the chemical etchant during release, we can boost the yield to more than 85%. Preliminary mechanical characterization of two example devices certifies that they indeed exhibit the phononic bandgap required for laser-induced localization experiments.

These large fabricated devices with defect free large band gap are expected to give promising mass and mode shape tuning results. For example, crystals that have 2750 unit cells (figure 3.21) will result in around three orders of magnitude reduction of the band gap edge mode effective mass as it becomes localized in the mid of the gap (where its spatial extent reduces from 2750 unit cells to $\sim$1).

Following in the historical footsteps of the modern field of optomechanics, our next goal is to demonstrate localization bolometrically. If these highly stressed silicon nitride phononic crystals have been subjected to localized heat, the thermal expansion of the tethers will lead to a reduction in the tensile stress. This will result in a localized reduction in mechanical frequency (i.e. an anti-spring), and should drag a mode from the upper continuum band into the band gap. A localization that is similar to the one shown in figure 2.9, chapter 2, will be realized. Our lab can demonstrate this immediately in the fiber interferometer setup shown in figure 3.22, chapter 3. However, the setup will need to be upgraded to become suitable for this study, for example by:

- Depositing a good heat absorber and conductor (like platinum) on the phononic crystal membrane so that our existing laser also acts as a heat source, and / or
- Adding a second, higher-power laser at a different (absorptive) wavelength to more effectively heat the structure.

As the upper band edge mode enters the band gap, we expect to see an increase in the Brownian motion amplitude because (a) the membrane's modes will be thermally driven at relatively higher temperature than room temperature, (b) the local material will not be as stiff, and, most importantly, (c) the localized mode's effective mass (and hence its effective spring constant) will be significantly reduced. The quality factor, Q, of the mode should also increase as the mode moves deeper in the band gap. This Q increase is expected to be due to isolation from the environment.

The subsequent step will be incorporating phononic crystal membranes inside high finesse optical cavities. For devices with pad sizes 256, 128 and 64 μm, our group (for instance) has access to a macroscopic (centimeter scale) 20000 finesse Fabry Perot cavity [2]. For smaller devices (with pad sizes 16, 32 μm), our group also has access to microscopic (micrometers scale) fiber cavities [80, 81] with more than 30000 finesse. Using microcavities is advantageous in optomechanics, because the small round-trip time of the photon inside the cavity provides stronger optomechanical force. The first step will be stabilizing the frequency of the laser to the frequency of the optical cavity using the locking techniques developed in our laboratory for macroscopic and microscopic cavities [82, 83]. Then the floor will be ready to apply linear or quadratic optical springs [39] to demonstrate the physics shown in figure 2.8, chapter 2.

In parallel with all these efforts our lab is starting soon the design and the assembly of a laser Doppler vibrometer (LDV) [84]. In this technique, we will synchronize pulses of light with the driven motion of the membrane, and image the whole motion at once with a camera. The signal will be either Doppler frequency shift or simple interferometry. The main purpose of this system is to directly image the evolution of the mechanical modes as they are tuned through the gap. This will result in unambiguous demonstration of strong control and provide valuable immediate information during future experiments involving more complex structures.

Bibliography

[1] A. Z. Barasheed, T. Müller, and J. C. Sankey, "Optically defined mechanical geometry," *Physical Review A*, vol. 93, no. 5, p. 053811, may 2016. [Online]. Available: https://link.aps.org/doi/10.1103/PhysRevA.93.053811 7, 8

[2] C. Reinhardt, T. Müller, A. Bourassa, and J. C. Sankey, "Ultralow-Noise SiN Trampoline Resonators for Sensing and Optomechanics," *Physical Review X*, vol. 6, no. 2, p. 021001, apr 2016. [Online]. Available: http://link.aps.org/doi/10.1103/PhysRevX.6.021001 8, 39, 46, 47, 50, 53, 57, 58, 59, 63, 97, 101, 104

[3] S. Hembacher, F. J. Giessibl, and J. Mannhart, "Force Microscopy with Light-Atom Probes," *Science*, vol. 305, no. 5682, 2004. [Online]. Available: http://science.sciencemag.org/content/305/5682/380 1

[4] J. Chaste, A. Eichler, J. Moser, G. Ceballos, R. Rurali, and A. Bachtold, "A nanomechanical mass sensor with yoctogram resolution." *Nature nanotechnology*, vol. 7, no. 5, pp. 301–4, may 2012. [Online]. Available: http://dx.doi.org/10.1038/nnano.2012.42 1

[5] D. Rugar, R. Budakian, H. J. Mamin, and B. W. Chui, "Single spin detection by magnetic resonance force microscopy." *Nature*, vol. 430, no. 6997, pp. 329–32, jul 2004. [Online]. Available: http://dx.doi.org/10.1038/nature02658 1

[6] M. A. Castellanos-Beltran, D. Q. Ngo, W. E. Shanks, A. B. Jayich, and J. G. E. Harris, "Measurement of the Full Distribution of Persistent Current in Normal-Metal Rings," *Physical Review Letters*, vol. 110, no. 15, p. 156801, apr 2013. [Online]. Available: https://link.aps.org/doi/10.1103/PhysRevLett.110.156801 1

[7] C. L. Degen, M. Poggio, H. J. Mamin, C. T. Rettner, and D. Rugar, "Nanoscale magnetic resonance imaging." *Proceedings of the National Academy of Sciences of the United States of America*, vol. 106, no. 5, pp. 1313–7, feb 2009. [Online]. Available: http://www.pnas.org/content/106/5/1313.abstract 1

[8] B. P. Abbott and Others, "Observation of Gravitational Waves from a Binary Black Hole Merger," *Physical Review Letters*, vol. 116, no. 6, p. 061102, feb 2016. [Online]. Available: https://link.aps.org/doi/10.1103/PhysRevLett.116.061102 1

[9] M. Aspelmeyer, T. J. Kippenberg, and F. Marquardt, "Cavity optomechanics," *Reviews of Modern Physics*, vol. 86, no. 4, pp. 1391–1452, dec 2014. [Online]. Available: https://link.aps.org/doi/10.1103/RevModPhys.86.1391 1, 2

[10] P. F. Cohadon, A. Heidmann, and M. Pinard, "Cooling of a Mirror by Radiation Pressure," *Physical Review Letters*, vol. 83, no. 16, pp. 3174–3177, oct 1999. [Online]. Available: https://link.aps.org/doi/10.1103/PhysRevLett.83.3174 1, 2

[11] M. Zalalutdinov, A. Zehnder, A. Olkhovets, S. Turner, L. Sekaric, B. Ilic, D. Czaplewski, J. M. Parpia, and H. G. Craighead, "Autoparametric optical drive for micromechanical oscillators," *Applied Physics Letters*, vol. 79, no. 5, pp. 695–697, jul 2001. [Online]. Available: http://aip.scitation.org/doi/10.1063/1.1388869 1

[12] M. Vogel, C. Mooser, K. Karrai, and R. J. Warburton, "Optically tunable mechanics of microlevers," *Applied Physics Letters*, vol. 83, no. 7, pp. 1337–1339, aug 2003. [Online]. Available: http://aip.scitation.org/doi/10.1063/1.1600513 1

[13] C. H. Metzger and K. Karrai, "Cavity cooling of a microlever," *Nature*, vol. 432, no. 7020, pp. 1002–1005, dec 2004. [Online]. Available: http://www.nature.com/doifinder/10.1038/nature03118 1, 2

[14] T. Carmon, H. Rokhsari, L. Yang, T. J. Kippenberg, and K. J. Vahala, "Temporal Behavior of Radiation-Pressure-Induced Vibrations of an Optical Microcavity Phonon Mode," *Physical Review Letters*, vol. 94, no. 22, p. 223902, jun 2005. [Online]. Available: https://link.aps.org/doi/10.1103/PhysRevLett.94.223902 2

[15] T. J. Kippenberg, H. Rokhsari, T. Carmon, A. Scherer, and K. J. Vahala, "Analysis of Radiation-Pressure Induced Mechanical Oscillation of an Optical Microcavity," *Physical Review Letters*, vol. 95, no. 3, p. 033901, jul 2005. [Online]. Available: https://link.aps.org/doi/10.1103/PhysRevLett.95.033901 2

[16] O. Arcizet, P.-F. Cohadon, T. Briant, M. Pinard, and A. Heidmann, "Radiation-pressure cooling and optomechanical instability of a micromirror," *Nature*, vol. 444, no. 7115, pp. 71–74, nov 2006. [Online]. Available: http://www.nature.com/doifinder/10.1038/nature05244 2

[17] S. Gigan, H. R. Böhm, M. Paternostro, F. Blaser, G. Langer, J. B. Hertzberg, K. C. Schwab, D. Bäuerle, M. Aspelmeyer, and A. Zeilinger, "Self-cooling of a micromirror by radiation pressure," *Nature*, vol. 444, no. 7115, pp. 67–70, nov 2006. [Online]. Available: http://dx.doi.org/10.1038/nature05273 2

[18] A. Schliesser, P. Del'Haye, N. Nooshi, K. J. Vahala, and T. J. Kippenberg, "Radiation Pressure Cooling of a Micromechanical Oscillator Using Dynamical Backaction," *Physical Review Letters*, vol. 97, no. 24, p. 243905, dec 2006. [Online]. Available: http://link.aps.org/doi/10.1103/PhysRevLett.97.243905 2

[19] K.-K. Ni, R. Norte, D. J. Wilson, J. D. Hood, D. E. Chang, O. Painter, and H. J. Kimble, "Enhancement of Mechanical Q Factors by Optical Trapping," *Physical Review Letters*, vol. 108, no. 21, p. 214302, may 2012. [Online]. Available: https://link.aps.org/doi/10.1103/PhysRevLett.108.214302 2, 5, 102

[20] T. Corbitt, Y. Chen, E. Innerhofer, H. Müller-Ebhardt, D. Ottaway, H. Rehbein, D. Sigg, S. Whitcomb, C. Wipf, and N. Mavalvala, "An All-Optical Trap for a Gram-Scale Mirror," *Physical Review Letters*, vol. 98, no. 15, p. 150802, apr 2007. [Online]. Available: https://link.aps.org/doi/10.1103/PhysRevLett.98.150802 2

[21] Q. Lin, J. Rosenberg, D. Chang, R. Camacho, M. Eichenfield, K. J. Vahala, and O. Painter, "Coherent mixing of mechanical excitations in nano-optomechanical structures," *Nature Photonics*, vol. 4, no. 4, p. 236, feb 2010. [Online]. Available: http://www.nature.com/doifinder/10.1038/nphoton.2010.5 2, 102

[22] A. H. Safavi-Naeini, T. P. M. Alegre, J. Chan, M. Eichenfield, M. Winger, Q. Lin, J. T. Hill, D. Chang, and O. Painter, "Electromagnetically Induced Transparency and Slow Light with Optomechanics," *Nature*, vol. 472, no. 7341, pp. 69–73, 2010. [Online]. Available: http://arxiv.org/abs/1012.1934{%}0Ahttp://dx.doi.org/10.1038/nature09933 2, 102

[23] M. Zhang, G. S. Wiederhecker, S. Manipatruni, A. Barnard, P. McEuen, and M. Lipson, "Synchronization of Micromechanical Oscillators Using Light," *Physical Review Letters*, vol. 109, no. 23, p. 233906, dec 2012. [Online]. Available: https://link.aps.org/doi/10.1103/PhysRevLett.109.233906 2, 3, 102

[24] F. Massel, S. U. Cho, J.-M. Pirkkalainen, P. J. Hakonen, T. T. Heikkilä, and M. A. Sillanpää, "Multimode circuit optomechanics near the quantum limit," *Nature Communications*, vol. 3, p. 987, aug 2012. [Online]. Available: http://www.nature.com/doifinder/10.1038/ncomms1993 2, 102

[25] A. Shkarin, N. Flowers-Jacobs, S. Hoch, A. Kashkanova, C. Deutsch, J. Reichel, and J. Harris, "Optically Mediated Hybridization between Two Mechanical Modes," *Physical Review Letters*, vol. 112, no. 1, p. 013602, jan 2014. [Online]. Available: http://link.aps.org/doi/10.1103/PhysRevLett.112.013602 2, 3, 102

[26] H. Fu, T.-h. Mao, Y. Li, J.-f. Ding, J.-d. Li, and G. Cao, "Optically mediated spatial localization of collective modes of two coupled cantilevers for high sensitivity optomechanical transducer," *Applied Physics Letters*, vol. 105, no. 1, p. 014108, jul 2014. [Online]. Available: http://scitation.aip.org/content/aip/journal/apl/105/1/10.1063/1.4889804 2, 3, 102

[27] Y. Pennec, J. O. Vasseur, B. Djafari-Rouhani, L. Dobrzyński, and P. A. Deymier, "Two-dimensional phononic crystals: Examples and applications," *Surface Science Reports*, vol. 65, no. 8, pp. 229–291, aug 2010. [Online]. Available: http://www.sciencedirect.com/science/article/pii/S0167572910000555 4, 102

[28] M. Torres, F. R. Montero de Espinosa, D. García-Pablos, and N. García, "Sonic Band Gaps in Finite Elastic Media: Surface States and Localization Phenomena in Linear

and Point Defects," *Physical Review Letters*, vol. 82, no. 15, pp. 3054–3057, apr 1999. [Online]. Available: https://link.aps.org/doi/10.1103/PhysRevLett.82.3054 4

[29] O. Painter, A. T. P. Mayer, S.-N. Amir, and W. Martin, "Quasi-two-dimensional optomechanical crystals with a complete phononic bandgap," *Optics Express*, vol. 19, no. 6, 2011. [Online]. Available: https://www.osapublishing.org/DirectPDFAccess/930D39ED-0432-E2DE-5FEACB3D398F881B{_}210757/oe-19-6-5658.pdf?da=1{&}id=210757{&}seq=0{&}mobile=no 4

[30] E. Gavartin, R. Braive, I. Sagnes, O. Arcizet, A. Beveratos, T. J. Kippenberg, and I. Robert-Philip, "Optomechanical Coupling in a Two-Dimensional Photonic Crystal Defect Cavity," *Physical Review Letters*, vol. 106, no. 20, p. 203902, may 2011. [Online]. Available: https://link.aps.org/doi/10.1103/PhysRevLett.106.203902 4

[31] J. Chan, T. P. M. Alegre, A. H. Safavi-Naeini, J. T. Hill, A. Krause, S. Gröblacher, M. Aspelmeyer, and O. Painter, "Laser cooling of a nanomechanical oscillator into its quantum ground state," *Nature*, vol. 478, no. 7367, pp. 89–92, oct 2011. [Online]. Available: http://dx.doi.org/10.1038/nature10461 4, 5

[32] A. H. Safavi-Naeini, J. Chan, J. T. Hill, T. P. M. Alegre, A. Krause, and O. Painter, "Observation of Quantum Motion of a Nanomechanical Resonator," *Physical Review Letters*, vol. 108, no. 3, p. 033602, jan 2012. [Online]. Available: http://link.aps.org/doi/10.1103/PhysRevLett.108.033602 4, 5

[33] J. T. Hill, A. H. Safavi-Naeini, J. Chan, O. Painter, and H. Wang, "Coherent optical wavelength conversion via cavity optomechanics," *Nature Communications*, vol. 3, p. 1196, nov 2012. [Online]. Available: http://www.nature.com/doifinder/10.1038/ncomms2201 4, 5

[34] A. H. Safavi-Naeini, S. Gröblacher, J. T. Hill, J. Chan, M. Aspelmeyer, and O. Painter, "Squeezed light from a silicon micromechanical resonator," *Nature*, vol. 500, no. 7461, pp. 185–189, 2013. [Online]. Available: http://www.nature.com/doifinder/10.1038/nature12307 4

[35] P.-L. Yu, K. Cicak, N. S. Kampel, Y. Tsaturyan, T. P. Purdy, R. W. Simmonds, and C. A. Regal, "A phononic bandgap shield for high-Q membrane microresonators," *Applied Physics Letters*, vol. 104, no. 2, p. 023510, jan 2014. [Online]. Available: http://scitation.aip.org/content/aip/journal/apl/104/2/10.1063/1.4862031 4

[36] J. D. Cohen, S. M. Meenehan, G. S. MacCabe, S. Gr oblacher, A. H. Safavi-Naeini, F. Marsili, M. D. Shaw, and O. Painter, "Phonon counting and intensity interferometry of a nanomechanical resonator," pp. 1–10, 2014. [Online]. Available: http://arxiv.org/abs/1410.1047{%}0Ahttp://dx.doi.org/10.1038/nature14349 4

[37] S. M. Meenehan, J. D. Cohen, G. S. MacCabe, F. Marsili, M. D. Shaw, and O. Painter, "Pulsed Excitation Dynamics of an Optomechanical Crystal Resonator near Its Quantum Ground State of Motion," *Physical Review X*, vol. 5, no. 4, p. 041002, oct 2015. [Online]. Available: https://link.aps.org/doi/10.1103/PhysRevX.5.041002 4

[38] D. E. Chang, K. K. Ni, O. Painter, and H. J. Kimble, "Ultrahigh-Q mechanical oscillators through optical trapping," *New Journal of Physics*, vol. 14, 2012. 5, 24, 25, 39, 40

[39] T. Müller, C. Reinhardt, and J. C. Sankey, "Enhanced optomechanical levitation of minimally supported dielectrics," *Physical Review A*, vol. 91, no. 5, p. 053849, may 2015. [Online]. Available: http://link.aps.org/doi/10.1103/PhysRevA.91.053849 5, 24, 25, 40, 42, 44, 104

[40] D. E. Chang, C. A. Regal, S. B. Papp, D. J. Wilson, J. Ye, O. Painter, H. J. Kimble, and P. Zoller, "Cavity opto-mechanics using an optically levitated nanosphere." *Proceedings of the National Academy of Sciences of the United States of America*, vol. 107, no. 3, pp. 1005–10, jan 2010. [Online]. Available: http://www.ncbi.nlm.nih.gov/pubmed/20080573http://www.pubmedcentral.nih.gov/articlerender.fcgi?artid=PMC2824320 5

[41] O. Romero-Isart, M. L. Juan, R. Quidant, and J. I. Cirac, "Toward quantum superposition of living organisms," *New Journal of Physics*, vol. 12, 2010. 5

[42] S. Singh, G. A. Phelps, D. S. Goldbaum, E. M. Wright, and P. Meystre, "All-Optical Optomechanics: An Optical Spring Mirror," *Physical Review Letters*, vol. 105, no. 21, p.

213602, nov 2010. [Online]. Available: https://link.aps.org/doi/10.1103/PhysRevLett.105.213602 5

[43] I. Wilson-Rae, R. A. Barton, S. S. Verbridge, D. R. Southworth, B. Ilic, H. G. Craighead, and J. M. Parpia, "High- Q Nanomechanics via Destructive Interference of Elastic Waves," *Physical Review Letters*, vol. 106, no. 4, p. 047205, jan 2011. [Online]. Available: http://link.aps.org/doi/10.1103/PhysRevLett.106.047205 5

[44] A. Jöckel, M. T. Rakher, M. Korppi, S. Camerer, D. Hunger, M. Mader, and P. Treutlein, "Spectroscopy of mechanical dissipation in micro-mechanical membranes," *Applied Physics Letters*, vol. 99, no. 14, p. 143109, oct 2011. [Online]. Available: http://scitation.aip.org/content/aip/journal/apl/99/14/10.1063/1.3646914 5

[45] S. Chakram, Y. Patil, L. Chang, and M. Vengalattore, "Dissipation in Ultrahigh Quality Factor SiN Membrane Resonators," *Physical Review Letters*, vol. 112, no. 12, p. 127201, mar 2014. [Online]. Available: https://link.aps.org/doi/10.1103/PhysRevLett.112.127201 5

[46] L. Villanueva and S. Schmid, "Evidence of Surface Loss as Ubiquitous Limiting Damping Mechanism in SiN Micro- and Nanomechanical Resonators," *Physical Review Letters*, vol. 113, no. 22, p. 227201, nov 2014. [Online]. Available: https://link.aps.org/doi/10.1103/PhysRevLett.113.227201 5

[47] Y. Tsaturyan, A. Barg, E. S. Polzik, and A. Schliesser, "Ultra-coherent nanomechanical resonators via soft clamping and dissipation dilution," *Nature nanotechnology*, vol. 12, no. June, pp. 1–10, 2016. [Online]. Available: http://arxiv.org/abs/1608.00937 5

[48] R. Norte, J. Moura, and S. Gröblacher, "Mechanical Resonators for Quantum Optomechanics Experiments at Room Temperature," *Physical Review Letters*, vol. 116, no. 14, p. 147202, apr 2016. [Online]. Available: https://link.aps.org/doi/10.1103/PhysRevLett.116.147202 5, 39

[49] A. D. O'Connell, M. Hofheinz, M. Ansmann, R. C. Bialczak, M. Lenander, E. Lucero, M. Neeley, D. Sank, H. Wang, M. Weides, J. Wenner, J. M. Martinis, and

A. N. Cleland, "Quantum ground state and single-phonon control of a mechanical resonator," *Nature*, vol. 464, no. 7289, pp. 697–703, apr 2010. [Online]. Available: http://www.nature.com/doifinder/10.1038/nature08967 5

[50] J. D. Teufel, T. Donner, D. Li, J. W. Harlow, M. S. Allman, K. Cicak, A. J. Sirois, J. D. Whittaker, K. W. Lehnert, and R. W. Simmonds, "Sideband cooling of micromechanical motion to the quantum ground state." *Nature*, vol. 475, no. 7356, pp. 359–63, jul 2011. [Online]. Available: http://dx.doi.org/10.1038/nature10261 5

[51] T. P. Purdy, P.-L. Yu, N. S. Kampel, R. W. Peterson, K. Cicak, R. W. Simmonds, and C. A. Regal, "Optomechanical Raman-ratio thermometry," *Physical Review A*, vol. 92, no. 3, p. 031802, sep 2015. [Online]. Available: https://link.aps.org/doi/10.1103/PhysRevA.92.031802 5

[52] M. Underwood, D. Mason, D. Lee, H. Xu, L. Jiang, A. B. Shkarin, K. Børkje, S. M. Girvin, and J. G. E. Harris, "Measurement of the motional sidebands of a nanogram-scale oscillator in the quantum regime," *Physical Review A*, vol. 92, no. 6, p. 061801, dec 2015. [Online]. Available: https://link.aps.org/doi/10.1103/PhysRevA.92.061801 5

[53] M. Tegmark, "Apparent wave function collapse caused by scattering," *Foundations of Physics Letters*, vol. 6, no. 6, pp. 571–590, dec 1993. [Online]. Available: http://link.springer.com/10.1007/BF00662807 5

[54] L. Tian and H. Wang, "Optical wavelength conversion of quantum states with optomechanics," *Physical Review A*, vol. 82, no. 5, p. 053806, nov 2010. [Online]. Available: https://link.aps.org/doi/10.1103/PhysRevA.82.053806 5

[55] K. Stannigel, P. Rabl, A. S. Sørensen, P. Zoller, and M. D. Lukin, "Optomechanical transducers for long-distance quantum communication." *Physical review letters*, vol. 105, no. 22, p. 220501, nov 2010. [Online]. Available: http://www.ncbi.nlm.nih.gov/pubmed/21231374 5

[56] C. A. Regal and K. W. Lehnert, "From Cavity Electromechanics to Cavity

Optomechanics," 2010. [Online]. Available: http://arxiv.org/abs/1010.4056{%}0Ahttp://dx.doi.org/10.1088/1742-6596/264/1/012025 5

[57] A. H. Safavi-Naeini, "Proposal for an optomechanical traveling wave phonon-photon translator," *N. J. Phys.*, vol. 13, 2011. 5

[58] Y.-D. Wang and A. A. Clerk, "Using Interference for High Fidelity Quantum State Transfer in Optomechanics," *Physical Review Letters*, vol. 108, no. 15, p. 153603, apr 2012. [Online]. Available: https://link.aps.org/doi/10.1103/PhysRevLett.108.153603 5

[59] Y. Liu, M. Davanço, V. Aksyuk, and K. Srinivasan, "Electromagnetically Induced Transparency and Wideband Wavelength Conversion in Silicon Nitride Microdisk Optomechanical Resonators," *Physical Review Letters*, vol. 110, no. 22, p. 223603, may 2013. [Online]. Available: https://link.aps.org/doi/10.1103/PhysRevLett.110.223603 5

[60] R. W. Andrews, R. W. Peterson, T. P. Purdy, K. Cicak, R. W. Simmonds, C. A. Regal, and K. W. Lehnert, "Bidirectional and efficient conversion between microwave and optical light," vol. 10, no. March, pp. 321–326, 2013. [Online]. Available: http://arxiv.org/abs/1310.5276{%}0Ahttp://dx.doi.org/10.1038/nphys2911 5

[61] P. W. Anderson, "Absence of Diffusion in Certain Random Lattices," *Physical Review*, vol. 109, no. 5, pp. 1492–1505, mar 1958. [Online]. Available: https://link.aps.org/doi/10.1103/PhysRev.109.1492 5, 97

[62] B. E. A. Saleh and M. C. Teich, *Fundamentals of photonics.* Wiley-Interscience, 2007. 10

[63] N. W. Ashcroft and N. D. Mermin, *Solid state physics.* Holt, Rinehart and Winston, 1976. 12

[64] J. D. Joannopoulos, S. G. Johnson, J. N. Winn, and R. D. Meade, *Photonic Crystals : Molding the Flow of Light (Second Edition).* Princeton University Press, 2008. 19

[65] J. D. Thompson, B. M. Zwickl, A. M. Jayich, F. Marquardt, S. M. Girvin, and J. G. E. Harris, "Strong dispersive coupling of a high-finesse cavity to a micromechanical

membrane," *Nature*, vol. 452, no. 7183, pp. 72–75, mar 2008. [Online]. Available: http://www.nature.com/doifinder/10.1038/nature06715 38

[66] N. E. Flowers-Jacobs, S. W. Hoch, J. C. Sankey, A. Kashkanova, A. M. Jayich, C. Deutsch, J. Reichel, and J. G. E. Harris, "Fiber-cavity-based optomechanical device," *Applied Physics Letters*, vol. 101, no. 22, 2012. 39, 44

[67] D. Lee, M. Underwood, D. Mason, A. B. Shkarin, S. W. Hoch, and J. G. E. Harris, "Multimode optomechanical dynamics in a cavity with avoided crossings," *Nature Communications*, vol. 6, pp. 1–7, 2014. [Online]. Available: http://arxiv.org/abs/1401.2968{%}0Ahttp://dx.doi.org/10.1038/ncomms7232 44

[68] M. Aspelmeyer, T. J. Kippenberg, and F. Marquardt, "Cavity Optomechanics," pp. 1–4, 2014. [Online]. Available: http://link.springer.com/10.1007/978-3-642-55312-7 44

[69] J. R. S. Bruce W. Smith, Kazuaki Suzuki, *Microlithography: Science and Technology*, 1998. [Online]. Available: https://www.crcpress.com/Microlithography-Science-and-Technology-Second-Edition/Smith-Suzuki/p/book/9780824790240 51, 79, 80

[70] S. Franssila, *Introduction to microfabrication*. John Wiley & Sons, 2010. [Online]. Available: http://ca.wiley.com/WileyCDA/WileyTitle/productCd-0470749830.html 51

[71] BYU, "Oxide Film Color Calculator and Chart | BYU Cleanroom." [Online]. Available: https://cleanroom.byu.edu/color{_}chart 66, 69

[72] M. F. Ceiler, P. A. Kohl, and S. A. Bidstrup, "Plasma-Enhanced Chemical Vapor Deposition of Silicon Dioxide Deposited at Low Temperatures." [Online]. Available: http://jes.ecsdl.org/content/142/6/2067.full.pdf 79, 80

[73] B. science, "Brewer Science® ProTEK ® PSB." [Online]. Available: http://www.brewerscience.com/wp-content/uploads/2016/06/protek{_}psb.ds{_}.pdf 81, 94

[74] K. R. Williams, K. Gupta, and M. Wasilik, "Etch Rates for Micromachining Processingâ-Part II," *JOURNAL OF MICROELECTROMECHANICAL SYSTEMS*, vol. 12, no. 6, p. 761, 2003. 86

[75] R. Becker, "Here's why you can't see all twelve black dots in this optical illusion - The Verge," 2016. [Online]. Available: https://www.theverge.com/2016/9/12/12885574/optical-illusion-12-black-dots 87

[76] A. Einstein, "Investigation on the theory of the Brownian movement," *Ann. d. Phys.*, p. 549, 1905. [Online]. Available: http://users.physik.fu-berlin.de/{~}kleinert/files/eins{_}brownian.pdf 97

[77] R.KUBO, "The fluctuation-Dissipation theorem," *Reports on progress in physics IOP science*, vol. 29, p. 255, 1966. [Online]. Available: http://iopscience.iop.org/article/10.1088/0034-4885/29/1/306/meta 97

[78] A. E. Siegman, *Lasers*, 1986. [Online]. Available: https://www.osapublishing.org/books/bookshelf/lasers.cfm 98

[79] L. A. L. A. Coldren, S. W. S. W. Corzine, and M. Mashanovitch, *Diode lasers and photonic integrated circuits*. Wiley, 2012. 98

[80] E. Janitz, M. Ruf, M. Dimock, A. Bourassa, J. Sankey, and L. Childress, "Fabry-Perot microcavity for diamond-based photonics," *Physical Review A*, vol. 92, no. 4, p. 043844, oct 2015. [Online]. Available: https://link.aps.org/doi/10.1103/PhysRevA.92.043844 104

[81] V. Dumont, "Flexural membrane-at-the-edge optomechanical system," Master Thesis, McGill, 2016. [Online]. Available: https://oatd.org/oatd/search?q=*{%}3A*{&}language.facet=zh{&}sort=date{&}language.facet=en{&}discipline.facet=DepartmentofPhysics{&}start=1 104

[82] C. Reinhardt, T. Müller, and J. C. Sankey, "Simple delay-limited sideband locking with heterodyne readout," *Optics Express*, vol. 25, no. 2, p. 1582, jan 2017. [Online]. Available: https://www.osapublishing.org/abstract.cfm?URI=oe-25-2-1582 104

[83] E. Janitz, M. Ruf, Y. Fontana, J. Sankey, and L. Childress, "High mechanical bandwidth fiber-coupled Fabry-Perot cavity," *Optics Express*, vol. 25, no. 17, p. 20932, aug 2017. [Online]. Available: https://www.osapublishing.org/abstract.cfm?URI=oe-25-17-20932 104

[84] S. Rothberg, M. Allen, P. Castellini, D. Di Maio, J. Dirckx, D. Ewins, B. Halkon, P. Muyshondt, N. Paone, T. Ryan, H. Steger, E. Tomasini, S. Vanlanduit, and J. Vignola, "An international review of laser Doppler vibrometry: Making light work of vibration measurement," *Optics and Lasers in Engineering*, vol. 99, pp. 11–22, dec 2017. [Online]. Available: http://www.sciencedirect.com/science/article/pii/S0143816616303724 104